Novel decay properties of positive-parity low-spin states of deformed gadolinium and dysprosium nuclei

Neuartige Zerfallseigenschaften von Niedrigspinzuständen positiver Parität in deformierten Gadolinium- und Dysprosiumisotopen

Zur Erlangung des Grades eines Doktors der Naturwissenschaften (Dr. rer. nat.)
Genehmigte Dissertation von Tobias Beck, M.Sc. M.Sc. aus Dieburg
Tag der Einreichung: 8. Juni 2021, Tag der Prüfung: 5. Juli 2021

1. Gutachten: Prof. Dr. Dr. h. c. mult. Norbert Pietralla
2. Gutachten: Prof. Dr. Joachim Enders
Darmstadt – D 17

TECHNISCHE UNIVERSITÄT DARMSTADT

Fachbereich Physik
Institut für Kernphysik
AG Pietralla

Novel decay properties of positive-parity low-spin states of deformed gadolinium and dysprosium nuclei
Neuartige Zerfallseigenschaften von Niedrigspinzuständen positiver Parität in deformierten Gadolinium- und Dysprosiumisotopen

Accepted doctoral thesis by Tobias Beck, M.Sc. M.Sc.

1. Review: Prof. Dr. Dr. h. c. mult. Norbert Pietralla
2. Review: Prof. Dr. Joachim Enders

Date of submission: June 8, 2021
Date of thesis defense: July 5, 2021

Darmstadt – D 17

Please cite this document as:
URN: urn:nbn:de:tuda-tuprints-192550
URL: https://tuprints.ulb.tu-darmstadt.de/19255

Erklärungen laut Promotionsordnung

§8 Abs. 1 lit. c PromO

Ich versichere hiermit, dass die elektronische Version meiner Dissertation mit der schriftlichen Version übereinstimmt.

§8 Abs. 1 lit. d PromO

Ich versichere hiermit, dass zu einem vorherigen Zeitpunkt noch keine Promotion versucht wurde. In diesem Fall sind nähere Angaben über Zeitpunkt, Hochschule, Dissertationsthema und Ergebnis dieses Versuchs mitzuteilen.

§9 Abs. 1 PromO

Ich versichere hiermit, dass die vorliegende Dissertation selbstständig und nur unter Verwendung der angegebenen Quellen verfasst wurde.

§9 Abs. 2 PromO

Die Arbeit hat bisher noch nicht zu Prüfungszwecken gedient.

Darmstadt, 8. Juni 2021

Tobias Beck, M.Sc. M.Sc.

Abstract

Atomic nuclei are complex many-body quantum systems. Still, selected properties can often be modeled by macroscopic equilibrium shapes. Their evolution with nucleon number exhibits all signs of phase-transitional behavior. A prominent example for a transition between spherical and axially-symmetric deformed phases is the region of the nuclear chart in the vicinity of $N = 90$. It is characterized by a rapid onset of deformation with neutron number which is discernible from a multitude of observables such as isomer shifts, excitation energies, and transition strengths.

Mixed-symmetry states – states with nontrivial symmetry properties regarding their proton and neutron subsystems – have proven their sensitivity to the underlying shell structure as well as shape evolution across quantum phase transitions. Especially the electromagnetic transitions between the 1^+ scissors mode and the 0^+_2 state are strongly affected by the amount of nuclear deformation. In this work, the elusive $E2$ properties of mixed-symmetry states are established as novel signatures for phase-transitional behavior. This includes their extraction for the transitional nucleus ^{154}Gd and the quadrupole deformed nuclei ^{162,164}Dy using the method of nuclear resonance fluorescence at the High-Intensity γ-ray Source in Durham, NC, USA in connection with calculations in the proton-neutron version of the algebraic Interacting Boson Model.

Precision values for the branching ratios between the scissors mode and the 2^+_1 state of ^{164}Dy uncover significant deviations from the Alaga predictions for $K = 1$ states. From a two-state mixing calculation, the K- mixing matrix element along with first information on $\Delta K = 0$ $M1$ excitation strength is obtained. The latter is about two orders of magnitude smaller than usual collective $\Delta K = 1$ $M1$ strengths. This mixing is caused by the Coriolis interaction. It represents a first-order perturbation of a Hamiltonian which is diagonal in K. The associated mixing matrix element is twice as large as the one obtained from the second-order effect which admixes ground and γ bands.

Zusammenfassung

Atomkerne sind komplexe Vielteilchen-Quantensysteme. Dennoch können ausgewählte Eigenschaften oft durch makroskopische Kerngestalten modelliert werden. Ihre Entwicklung mit der Nukleonenzahl zeigt alle Anzeichen eines Phasenübergangs. Ein prominentes Beispiel für einen Übergang zwischen sphärischen und axialsymmetrisch deformierten Phasen ist die Region der Nuklidkarte in der Nähe von $N = 90$. Sie ist gekennzeichnet durch ein schnelles Einsetzen von Kerndeformation mit der Neutronenzahl, was an einer Vielzahl von Observablen wie Isomerieverschiebungen, Anregungsenergien und Übergangsstärken erkennbar ist.

Gemischtsymmetrische Zustände – Zustände mit nichttrivialen Symmetrieeigenschaften bezüglich ihrer Protonen- und Neutronensysteme – sind sensitiv sowohl auf die zugrundeliegende Schalenstruktur als auch die Evolution der Kerngestalt über Quantenphasenübergänge hinweg. Insbesondere die elektromagnetischen Übergänge zwischen der 1^+-Scherenmode und dem 0_2^+-Zustand werden stark vom Grad der Kerndeformation beeinflusst. In dieser Arbeit werden die $E2$-Eigenschaften von gemischtsymmetrischen Zuständen als neuartige Signaturen für Phasenübergangsverhalten etabliert. Dies beinhaltet deren Bestimmung für den Übergangskern ^{154}Gd und die quadrupoldeformierten Kerne ^{162,164}Dy mittels der Methode der Kernresonanzfluoreszenz an der High-Intensity γ-ray Source in Durham, NC, USA in Verbindung mit Berechnungen in der Proton-Neutron-Version des algebraischen Interacting Boson Model.

Präzisionswerte für die Verzweigungsverhältnisse zwischen der Scherenmode und dem 2_1^+-Zustand von ^{164}Dy zeigen deutliche Abweichungen von den Alaga-Vorhersagen für $K = 1$-Zustände. Aus einer Zweizustands-Mischungsrechnung wird das K-Mischungsmatrixelement zusammen mit ersten Informationen über die $\Delta K = 0$ $M1$-Anregungsstärke bestimmt. Letztere ist etwa zwei Größenordnungen kleiner als die üblichen kollektiven $\Delta K = 1$ $M1$-Übergangsstärken. Die zugrundeliegende Mischung wird

durch die Coriolis-Wechselwirkung verursacht. Dabei handelt es sich um eine Störung erster Ordnung des in K diagonalen Hamiltonoperators. Das zugehörige Mischungsmatrixelement ist doppelt so groß wie dasjenige, das sich aus dem Effekt zweiter Ordnung ergibt, welcher die Grundzustands- und γ-Banden mischt.

Contents

In this universe, as long as you're patient
you can make any wish come true.
Even though the possibility is minuscule,
it still exists.

From *Taking care of god* by Cixin Liu,
Head of Zeus Ltd, London (2017)

1. Introduction

Atomic nuclei are peculiar and in many ways Janus-like entities. Due to their mesoscopic structure of up to 300 individual particles they exhibit a complex juxtaposition of single-particle and collective degrees of freedom. This ambiguity is also reflected in their theoretical description; the former aspect is, for instance, represented by the microscopic shell model [1, 2] while the latter can be connected to macroscopic excitations of the nucleus' assumed equilibrium shape [3]. The most fundamental questions of nuclear-structure physics are the reconciliation of these seemingly antithetical paradigms and their evolution with changing proton and neutron numbers [4] or asymmetry [5]. A contemporary example for the experimental exploration of the latter is the study of so-called islands of inversion [6] at rare-isotope beam facilities [7].

Starting from the spherical shell model, the emergence of collectivity and deformation can be traced back to configuration mixing due to the isoscalar part of the proton-neutron interaction [8]. For light and medium-mass nuclei, a strong overlap between proton and neutron orbitals is required [9]. In the case of heavy nuclei, on the contrary, the sheer number of potential proton-neutron interactions can facilitate a dominance over the pairing force which favors sphericity [10]. Hence, the occurrence of deformation and phase-transitional behavior are dictated by the proton-neutron degree of freedom. A possibility for the study of this aspect arises from excitation modes with an explicit proton-neutron (partial) asymmetry. While giant resonances of this type [11] are known for almost a century [12], their valence-space counterparts did not come into the spotlight until the advent of the algebraic Interacting Boson Model [13] in the 1980s. There, they emerge naturally and form an entire class [14] of excitations with nontrivial symmetry properties with respect to the two coupled subsystems. The most prominent representatives are the energetically lowest-lying states; namely the 2^+_{ms} states of spherical vibrators [15] and the 1^+_{sc} scissors mode of quadrupole-deformed nuclei [16, 17].

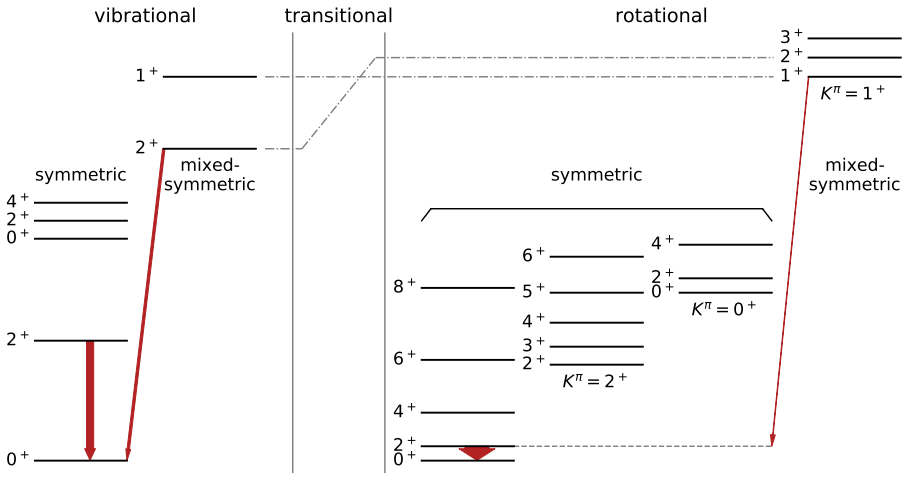

Figure 1.1.: Schematic evolution of nuclear structure across a phase transition connecting spherical (left panel) and deformed (right panel) phases. The suspected interchange of mixed-symmetric 1^+ and 2^+ states in the transitional region is indicated by dash-dotted lines. Experimentally available $E2$ transitions of these states and between the 2^+_1 and 0^+_1 states are highlighted by red arrows. Their widths approximately scale with the magnitude of the $E2$ transition strength. The opposite magnitude evolution of these transition strengths along with the ordering of the states themselves might constitute a novel signature for the quantum phase transition. This Figure is inspired by Fig. 1 of Ref. [20].

The evolution of the scissors mode's $M1$ properties across the quantum phase transition in the rare-earth region around neutron number $N = 90$ [18] has recently been described for ^{152,154,156}Gd in terms of a novel signature [19]. Concerning the 2^+_{ms} state and the associated $E2$ transition strengths, their trend with incipient nuclear deformation remains an enigma. The suspected behavior is schematically depicted in Fig. 1.1; the 2^+_{ms} state evolves from a one-phonon state of spherical vibrators to a member of the $K = 1$ scissors-mode rotational band. Given the distinct phonon

structure of mixed-symmetry states for vibrational nuclei, which was experimentally verified for ^{94}Mo [21, 22], this evolution necessarily requires a commutation of the mixed-symmetric 1^+ and 2^+ states. Since the exact location of this exchange might coincide with the critical point of the phase transition, the ordering of the lowest-lying mixed-symmetry states can provide valuable information. Beyond excitation energies also $E2$ transition strengths are sensitive indicators for the phase transition. The transition between the 2^+_{ms} state and the ground state is weakly collective for spherical nuclei whereas the ground-state excitation of the 2^+_{sc} state is minuscule [23, 24]. It is the aim of this work to elucidate whether $E2$ transitions between mixed-symmetry states and the ground-state band represent a new class of experimental signatures for the spherical-deformed quantum-phase transition at $N = 90$.

2. Theoretical background

This Chapter is dedicated to the introduction of concepts from nuclear physics which are pivotal for the present work. These encompass a brief overview of symmetries in nuclear systems and the mixing of quantum states, the symmetry-based algebraic Interacting Boson Model, and the transitions between idealized paradigms in the equilibrium shapes of atomic nuclei. The individual Sections are arranged in such a way, that there is a fairly smooth transition from basic concepts to applications from nuclear-structure physics.

2.1. Symmetries of quantum systems

Classical mechanics relies on three fundamental conservation laws: conservation of energy, linear momentum, and angular momentum. By virtue of Noether's theorem [25], these conservation laws are related to symmetries of action; namely time, translational, and rotational invariance. In quantum-mechanical systems, these quantities are conserved as well.[1] Atomic nuclei are popular examples for such systems. More precisely, they are strongly-interacting two-component quantum systems consisting of up to about 300 particles. On the basis of individual nucleons, these systems exhibit an excessive number of degrees of freedom. Thus, the description of nuclear states in terms of symmetry properties and conserved quantities plays a prominent role. In the following, symmetries in ordinary three-dimensional space are discussed.[2]

[1] In relativistic systems, they become intertwined and result in Lorentz invariants of the four-dimensional space-time.

[2] Additional examples for symmetries of strongly-interacting quantal systems are spin and isospin of atomic nuclei or color of quarks.

2.1.1. Axial and $\mathscr{P}$ symmetry

The success of the shell-model [1, 2, 26, 27], which features a spherical central potential, hints at an approximate spherical symmetry of many nuclei in the vicinity of closed shells. However, the occurrence of non-vanishing electric quadrupole moments [Sec. 3.3 of [28]] indicates that this symmetry is broken [3, 29].[3] Since the existence of deformation enables the specification of the whole system's orientation, rotational degrees of freedom emerge from this breaking of rotational symmetry [31]. If the deformation remains invariant with respect to a subgroup of rotations, the additional degrees of freedom are correspondingly restricted. The most prominent example with such a partial invariance is axially-symmetric deformation.[4] In that case, collective rotations about the intrinsic symmetry axis do not occur and $\boldsymbol{J_3}$, which is the projection of the body's total angular momentum $\boldsymbol{J}$ onto the intrinsic symmetry axis, is a constant of motion. The eigenvalues of $\boldsymbol{J_3}$ are denoted by K and take values $K \in [-J, J] \cap \mathbb{Z}$.[5] Consequently, K is a good quantum number and has a fixed value for all members of the rotational band.

The intrinsic nuclear states, which are eigenstates of the intrinsic part of the nuclear Hamiltonian,[6] can be classified by their symmetry properties. The most prominent example is the behavior under space inversion which is known as $\mathscr{P}$ symmetry with parity quantum numbers $\pi = \pm 1$ [Sec. 4-2d of [4]]. Since $\mathscr{P}$ acts solely on the intrinsic motion, π is common for all states of a rotational band. In combination with axial deformation, space-reflection invariance yields a spheroidal shape. Nuclei with these characteristics exhibit positive-parity rotational bands. Conversely, the identification of low-lying negative-parity states [32–34] might indicate the existence of shapes

[3] In fact, nuclear deformation has been inferred from nuclear quadrupole moments deduced on the basis of atomic hyperfine structure as early as 1936 [§ 25 of [30]]. A more detailed discussion is presented in Ref. [31].

[4] It has to be stressed, that in the present context axially-symmetric deformation describes a generic solid of revolution. It is by no means restricted to a spheroid, which is a special case requiring further reduction of the rotational degrees of freedom.

[5] In this sense, the definition of K is completely analogue to the magnetic quantum number M, which is the eigenvalue of $\boldsymbol{J_z}$. The latter is the projection of $\boldsymbol{J}$ onto the space-fixed (laboratory frame) z axis.

[6] In the collective model of Bohr and Mottelson the nuclear Hamiltonian can be separated into intrinsic and rotational parts, i.e. $\boldsymbol{H} = \boldsymbol{H}_{\text{int}} + \boldsymbol{H}_{\text{rot}}$ [Eq. (4-3) of [4]]. Its eigenstates are products of intrinsic and rotational components. Hence, each intrinsic state gives rise to a range of rotational levels built on it.

asymmetric under reflection [35], such as a pear shape[7] [36, 37]. The realization of such a deformation is corroborated by a variety of studies focusing on different observables [38–41].

2.1.2. $\mathscr{R}$ symmetry

A spheroidal shape is also obtained, if the nuclear body is axially symmetric and invariant with respect to a rotation of 180° around an arbitrarily chosen axis perpendicular to the symmetry axis.[8] This is known as $\mathscr{R}$ symmetry [Sec. 4-2c of [4]], whose interplay with parity is illustrated in Fig. 2.1. Without loss of generality, the rotation $\mathscr{R}$ is defined with respect to the 2 axis, i.e. $\mathscr{R} = \mathscr{R}_2(\pi)$. The $\mathscr{R}$ symmetry implies that the rotation $\mathscr{R}$ is no longer part of the rotational degrees of freedom but of the intrinsic. Technically, this constraint is realized by requiring that the operator $\mathscr{R}_e$, which performs the rotation on the external orientation angles, is identical to $\mathscr{R}_i$ acting on the intrinsic variables; i.e. $\mathscr{R}_e = \mathscr{R}_i$.[9] The operation $\mathscr{R}_e$, which can be expressed in the form of a conventional rotation operator

$$\mathscr{R}_e = \exp[-i\pi \boldsymbol{J}_2],$$

acts solely on the rotational part of the wave function. It inverts the direction of the symmetry axis by putting $\vartheta \to \pi - \vartheta$ and $\varphi \to \varphi + \pi$. For an arbitrary state with initial quantum numbers J, M, and K, the effect on the rotational wave function is given by [Eq. 4-18 of [4]]

$$\mathscr{R}_e \mathscr{D}^J_{MK}(\Omega) = \exp[-i\pi \boldsymbol{J}_2] \mathscr{D}^J_{MK}(\Omega) = (-1)^{J+K} \mathscr{D}^J_{M-K}(\Omega). \tag{2.1}$$

The inversion of the symmetry axis can be observed in the effect of $\mathscr{R}_e$ on the Wigner $\mathscr{D}$ matrices $\mathscr{D}^J_{MK}(\Omega)$, causing the expected inversion of the projection quantum number K whereas M remains untouched. The latter equality in Eq. (2.1) is derived employing Eq. (1A-47) of Ref. [28]. The rotation $\mathscr{R}_i$, on the other hand, affects solely the intrinsic

[7] A pear shape might be realized either in a dynamic way (octupole vibrations) or having a static shape (permanent octupole deformation).

[8] For an axially-symmetric but non-spherical system, $\mathscr{R}$ symmetry is the only additional rotational symmetry which does not induce sphericity.

[9] Graphically, $\mathscr{R}_e = \mathscr{R}_i$ means that a rotation by 180° does not only affect the orientation of the nucleus with respect to the laboratory frame. Instead, also the intrinsic states are rotated with respect to the body-fixed coordinate system.

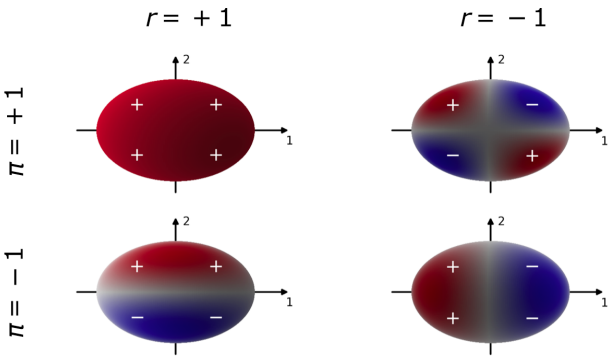

Figure 2.1.: Simplified visualization of intertwined $\mathscr{P}$ and $\mathscr{R}$ symmetry. The body-fixed symmetry axis of the axially-symmetric deformed nuclei is denoted by '1' and a generic perpendicular axis by '2'. The spatial distributions of the collective wave function over the nuclear body are color-coded and labelled by their signs. Since the nuclei on the left-hand side are invariant under a rotation of 180° about '2', they are characterized by the quantum number $r = +1$ in contrast to nuclei on the right-hand side with $r = -1$.

states $\Phi_K(\mathbf{r})$, which are described by the coordinates $\mathbf{r}$ with respect to the body-fixed frame. For a generic intrinsic state with projection K, the rotated state with negative eigenvalues of $\boldsymbol{J_3}$ is denoted $\overline{K}$ and given by

$$\Phi_{\overline{K}}(\mathbf{r}) = \mathscr{R}_i^{-1}\Phi_K(\mathbf{r}). \tag{2.2}$$

In the case of $K = 0$, the $\mathscr{D}$ matrices in Eq. (2.1) are reduced to spherical harmonics [Eq. (3.15) of [42]] and the initial and rotated intrinsic wave functions in Eq. (2.2) are identical. Consequently, Eqs. (2.1) and (2.2) can be simplified and reformulated in terms of the ordinary eigenvalue equations

$$\begin{aligned} &\mathscr{R}_e Y_{JM}(\vartheta,\varphi) = (-1)^J Y_{JM}(\vartheta,\varphi) \text{ and} \\ &\mathscr{R}_i \Phi_{K=0}(\mathbf{r}) \;\; = r\Phi_{K=0}(\mathbf{r}). \end{aligned} \tag{2.3}$$

Since application of $\mathscr{R}^2$ yields the initial state, the eigenvalues of $\mathscr{R}_i$ must be $r = \pm 1$. In combination with the constraint $\mathscr{R}_e = \mathscr{R}_i$, Eq. (2.3) implies $r = (-1)^J$. Hence,

a rotational band with $K = 0$ and $r = -1$ ($r = +1$) contains only states with odd (even) angular momentum quantum numbers. For these bands, $\mathscr{R}$ symmetry can be assigned unambiguously, whereas rotational bands comprising angular momenta $J = K, K+1, \ldots$ are obtained for intrinsic states with $K \neq 0$. The corresponding wave functions involve a sum over the twofold degenerate intrinsic states with positive and negative K [Eq. (4-19) of [4]], which represents an interweaving of intrinsic and rotational degrees of freedom. It is modulated by the factor $(-1)^{J+K}$, which is commonly referred to as the signature and naturally also affects the rotational energy spectrum [Sec. 4-3a ibid.].

The interplay of different symmetries governs the rotational degrees of freedom. Consequently, the low-energy rotational bands of even-even nuclei can be interpreted in terms of symmetries of nuclear deformation. Since each value of J occurs only once for a given rotational band, the nuclear body must be axially symmetric. Otherwise, the system is triaxial and rotational bands contain several states with the same angular momentum [Sec. 4-5 and especially Eq. (4-277) ibid.]. The occurrence of $\mathscr{R}$ and $\mathscr{P}$-symmetric deformation can be concluded from the absence of states with odd J values and parity doublets, respectively. Finally, time ($\mathscr{T}$) invariance is implied by the absence of degenerate states with the same quantum numbers J^π. These symmetry features, which are deduced solely from the analysis of rotational spectra, indicate a spheroidal deformation of the nuclear body.

All discussed symmetries are of 'geometric' nature in the sense that they are rooted in space-time. Beyond that, invariances in abstract spaces associated with intrinsic quantities such as spin, isospin or color are of interest. The general mathematical framework for the treatment of such symmetries is group theory. In Section 2.3 the algebraic Interacting Boson Model is presented, which is founded on the symmetries of a boson space and exploits group-theoretical techniques.

2.2. Mixing of quantum states

In Section 2.1, symmetries of a Hamiltonian $\boldsymbol{H}_0$ consisting of intrinsic and rotational parts were introduced. Its eigenstates can be expressed in terms of K and J, where K specifies the intrinsic state of the nucleus and J defines the rotational state's angular momentum. In its eigenbasis $\boldsymbol{H}_0$ is diagonal and, thus, actual computations are simple. However, pure configurations are seldomly encountered in nature. Instead, the Hamiltonian is subject to residual contributions $\boldsymbol{H}_1$, which are treated as perturbations to $\boldsymbol{H}_0$. The reasons for such perturbations are manifold; examples are deviations from axial symmetry or a coupling between rotational and intrinsic motion due to Coriolis and centrifugal forces [Sec. 4-4 of [4]]. Inclusion of these perturbations necessarily breaks the favorable structure of the Hamiltonian; while $\boldsymbol{H}_0$ is diagonal in the chosen basis, $\boldsymbol{H} = \boldsymbol{H}_0 + \boldsymbol{H}_1$ is not. Consequently, the eigenstates of $\boldsymbol{H}$ are linear combinations of the basis states. This effect is commonly referred to as band or K mixing.

In the present case, the perturbation might connect states belonging to different bands. Thus, the mixed states are no longer eigenstates of $\boldsymbol{H}_0$ and K is no longer a good quantum number.[10] In principle, a full diagonalization of the Hamiltonian matrix is necessary for a determination of the new eigenstates. A full calculation might be mathematically complex since the symmetries of $\boldsymbol{H}_0$ are no longer present in $\boldsymbol{H}$. However, a classification in terms of K still provides a simple language for describing these states. Irrespective of how complex the wave function of an, for instance, $J = 1$ state is, it can be fully decomposed into parts with K quantum numbers $K = 0$ and $K = 1$. Both components, $|K = 0, J = 1\rangle$ and $|K = 1, J = 1\rangle$, can then be treated separately as eigenstates of $\boldsymbol{H}_0$. As foreshadowed in the above example, a straightforward two-state mixing (TSM) calculation might satisfactorily well mimic the full diagonalization.

[10] The textbook example for such a symmetry breaking is isospin. Neglecting its charge-dependence, the strong nuclear force has an SU(2) isospin symmetry; i.e. the Hamiltonian $\boldsymbol{H}_0$ of the nucleus is invariant with respect to transformations between neutron and proton states. Inclusion of the Coulomb interaction, which acts solely between protons, breaks this symmetry [Sec. 1.1.6 of [43]].

In the following, two arbitrary dipole states 1_A and 1_B with excitation energies E_A and E_B[11] are considered. Then, their wave functions can be written as linear combinations of two basis states with good K quantum number, i.e.

$$\begin{pmatrix} |1_A\rangle \\ |1_B\rangle \end{pmatrix} = \begin{pmatrix} \alpha & \beta \\ -\beta & \alpha \end{pmatrix} \begin{pmatrix} |1_{K=0}\rangle \\ |1_{K=1}\rangle \end{pmatrix} \tag{2.4}$$

with amplitudes α and β normalized to $\alpha^2 + \beta^2 = 1$. The perturbed wave functions correspond to eigenfunctions of $\boldsymbol{H}$. The corresponding energies, E_A and E_B, are the eigenvalues of a 2×2 mixing matrix, which features nonvanishing off-diagonal entries V_{mix} due to $\boldsymbol{H}_1$. Consequently, E_A and E_B are obtained from the unperturbed energies E_I and E_{II} using the relation [Eq. (1.3) of [44]]

$$E_{A,B} = \frac{1}{2}\left[(E_I + E_{II}) \pm \sqrt{(E_I - E_{II})^2 + 4V_{\text{mix}}^2}\right].$$

Experimentally, the mixing parameters are accessible through transition rates. With the NRF method (cf. Section 3.1), especially the branching ratios [cf. Eq. (4.5)] to the 2_1^+ and 0_1^+ states of even-even nuclei

$$\begin{aligned} R_{1_A \to 2/0} &= \frac{B(\sigma 1; 1_A \to 2_1^+)}{B(\sigma 1; 1_A \to 0_1^+)} \text{ and} \\ R_{1_B \to 2/0} &= \frac{B(\sigma 1; 1_B \to 2_1^+)}{B(\sigma 1; 1_B \to 0_1^+)} \end{aligned} \tag{2.5}$$

can be determined precisely. Invoking Eq. (2.4) and the connection between the reduced transition probability and the associated matrix element [Eq. (1A-67) of [28]], the branching ratios can be rewritten in terms of matrix elements between states with good K quantum number. Subsequently, the dependence of the involved matrix elements on the angular momentum is removed, resulting in doubly reduced matrix elements [Eqs. (4-91) and (4-92) of [4]]. Their ratio $\langle K_f = 1 ||| \boldsymbol{T}(\sigma 1) ||| K_i = 0\rangle / \langle K_f = 0 ||| \boldsymbol{T}(\sigma 1) ||| K_i = 0\rangle$ is denoted Z and γ is the ratio β/α. This yields an alternative

[11] In the present discussion observed, i.e. perturbed or mixed, states are identified by letter subscripts whereas initial states are denoted by Roman numerals.

formulation of Eq. (2.5)[12] given by [45]

$$R_{1_A\to 2/0} = 5\left[\frac{\langle 2010|10\rangle + \sqrt{2}\gamma Z\langle 2011|11\rangle}{\langle 0010|10\rangle + \sqrt{2}\gamma Z\langle 0011|11\rangle}\right]^2 \text{ and}$$
$$R_{1_B\to 2/0} = 5\left[\frac{\sqrt{2}Z\langle 2011|11\rangle - \gamma\langle 2010|10\rangle}{\sqrt{2}Z\langle 0011|11\rangle - \gamma\langle 0010|10\rangle}\right]^2. \tag{2.6}$$

If no mixing occurs, i.e. $\gamma = 0$, the 1_A and 1_B states are of pure $K = 0$ and $K = 1$ nature, respectively. In that case, the branching ratios depend only on the ratio of squared Clebsch-Gordan coefficients[13] and $R_{1_A\to 2/0} = 2.0$ and $R_{1_B\to 2/0} = 0.5$ are obtained. This is known as the Alaga rule [46]. With increasing mixture ($\gamma \neq 0$) the branching ratios tend to deviate from the Alaga predictions. In fact, the implications of even little mixing can be drastic as $R_{1_A\to 2/0}$ is virtually nil for a certain value of γ. The evolution of the branching ratios with γ is visualized in panel (a) of Fig. 2.2. In order to determine the mixing parameters Z and γ, Eqs. (2.6) are reformulated to

$$(\gamma\cdot Z)_{\sigma_A} = \frac{\sqrt{2} + \sigma_A\left|\sqrt{R_{1_A\to 2/0}}\right|}{1 - \sqrt{2}\sigma_A\left|\sqrt{R_{1_A\to 2/0}}\right|} \text{ and}$$
$$(\gamma/Z)_{\sigma_B} = \frac{\sqrt{2}\sigma_B\left|\sqrt{R_{1_B\to 2/0}}\right| - 1}{\sqrt{2} + \sigma_B\left|\sqrt{R_{1_B\to 2/0}}\right|}. \tag{2.7}$$

Here, σ_A and σ_B explicitly denote the signs of the square roots of $R_{1_A\to 2/0}$ and $R_{1_B\to 2/0}$, respectively. Finally, the squared TSM parameters, γ^2 and Z^2, are given by

$$(\gamma^2)_{\sigma_A,\sigma_B} = (\gamma\cdot Z)_{\sigma_A}\cdot(\gamma/Z)_{\sigma_B} \text{ and}$$
$$(Z^2)_{\sigma_A,\sigma_B} = (\gamma\cdot Z)_{\sigma_A}/(\gamma/Z)_{\sigma_B}.$$

Thus, four distinct solutions (Z,γ) to the TSM scenario are obtained from the branching ratios. In the following, solely the solutions corresponding to positive values of Z and γ are considered.[14] In panel (b) of Fig. 2.2, these solutions correspond

[12] A detailed derivation of the connection between Eqs. (2.5) and (2.6) is given in Appendix A.1.

[13] This is a direct consequence of the assumed separability of intrinsic and rotational degrees of freedom mentioned in Section 2.1.2.

[14] For the remaining two solutions the discussion is completely analogous.

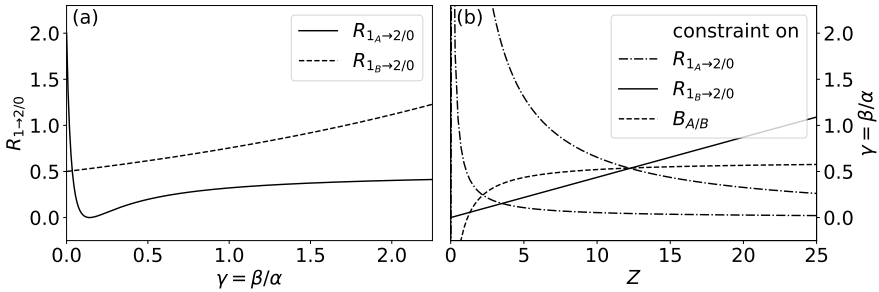

Figure 2.2.: Schematics of two-state mixing. The evolution of the branching ratios $R_{1_A\to 2/0}$ and $R_{1_B\to 2/0}$ [cf. Eqs. (2.5) and (2.6)] as a function of γ is shown in panel (a) for $Z = 10$. Already little mixing triggers a drastic decrease in $R_{1_A\to 2/0}$. Conversely, experimental information on the branching ratios constrains the potential solutions (Z, γ) to the TSM scenario [panel (b)]. The occurrence of two dash-dotted lines originates from an undefined phase in the initial problem [cf. Eq. (2.7)]. A unique solution is obtained through inclusion of an additional constraint on the ratio of excitation strengths $B_{A/B}$ (dashed line).

to intersections of the solid and dash-dotted lines. Apparently, these indicate either weak mixing and a comparable strength of $\Delta K = 0$ and $\Delta K = 1$ excitations or strong mixing and a dominating $\Delta K = 1$ matrix element. Introduction of an additional observable enables a consistency check and, thus, identification of the present scenario.[15] In the context of NRF experiments, the ratio of transition strengths $B_{A/B} := B(\sigma 1; 0_1^+ \to 1_A)/B(\sigma 1; 0_1^+ \to 1_B)$ is an obvious choice. Ultimately, the mixing amplitudes α and β are obtained from the mixing strength γ (cf. Appendix A.1). The mixing matrix element V_{mix} can be calculated from γ and the known final energies E_A and E_B (cf. Appendix A.2).

[15] In fact, an unambiguous disentanglement of the K-mixing scenario from branching ratios alone is not possible [47].

2.3. The Interacting Boson Model

Based on the seemingly simple constituents of atomic nuclei, a wide variety of theoretical models have been developed, which employ diverse assumptions and approaches. An essential parameter for characterization is their degree of microscopicity. The collective model of Bohr and Mottelson, whose properties were implicitly discussed in Section 2.1, is completely macroscopic. Examples for an entirely microscopic description are chiral effective field theory (EFT) [48, 49], which is rooted in the symmetries of quantum chromodynamics, and the nuclear shell model [1, 2, 26, 27].[16] While a description of rare-earth nuclei is not yet feasible in chiral EFT, shell-model type calculations of ^{154}Sm have been demonstrated recently [51] in the framework of the Monte-Carlo shell model [52, 53]. It enables the treatment of nuclei as mid-shell as ^{166}Er [51] and as heavy as the neutron-deficient mercury isotopes [54]. However, these calculations come at a great computational cost. This problem can be resolved by an additional truncation of the shell-model space.[17] An example for a rather drastic curtailing is the Interacting Boson Model (IBM), which is introduced in this Section.

The IBM belongs to the class of algebraic models which exploit group theoretical methods. It is based upon pioneering feats such as Elliot's SU(3) scheme [55], which represents the first sophisticated algebraic model, the truncated quadrupole-phonon model [56], and the work of Feshbach and Iachello [57, 58]. The introduction to the IBM formalism in Sections 2.3.1 and 2.3.2 is based on Refs. [13, 59–61]. Subsequently, potential extensions to the IBM and the connection to other nuclear models are briefly outlined.

2.3.1. Basic formalism and group structure

The IBM is founded on a heavily truncated shell-model space [Sec. 4 of [61]]. Its fundamental building blocks are different types of bosons which are understood as the pairing of like valence nucleons or holes. For a given nucleus with $N_p + N_n$ valence protons and neutrons (or holes due to the particle-hole conjugation in particle space) counted to the nearest closed shell $N = (N_p + N_n)/2$ bosons are considered in the IBM

[16] Naturally, both approaches are not necessarily completely separate. In Ref. [50] for instance, chiral EFT is used as a general operator basis to develop chiral interactions for the shell model.

[17] Already the shell model represents a truncation of the full A-body problem.

formalism. In the most basic form of the model, the IBM-1, the fermionic valence space is reduced to s ($J = 0$) and d ($J = 2$)[18] bosons,[19] which are oblivious to the isospin of their constituents. The basic operators of the IBM are twelve boson creation and annihilation operators

$$\boldsymbol{s}^\dagger, \boldsymbol{d}^\dagger_\mu \qquad \text{and} \qquad \boldsymbol{s}, \boldsymbol{d}_\mu \qquad \text{with} \qquad \mu \in \{0, \pm 1, \pm 2\}, \tag{2.8}$$

respectively. The operators introduced in Eq. (2.8) satisfy the standard Bose commutation relations. In order to equip also the annihilation operators with the symmetry properties of spherical tensors, they are redefined as

$$\widetilde{\boldsymbol{s}} = \boldsymbol{s} \qquad \text{and} \qquad \widetilde{\boldsymbol{d}}_\mu = (-1)^\mu \boldsymbol{d}_{-\mu}.$$

Using this redefinition, the resulting tensor operators obey the coupling rules of angular momenta [Eqs. (14.1) and (14.2) of [42]]. Since s and d bosons have a total of six magnetic substates, the s-d boson system can be described in terms of the six-dimensional unitary group, U(6). This Lie group is generated by the 36 boson number conserving tensor products[20] of the boson creation and annihilation operators [Eq. (2.7) of [13]].

For each Lie group of rank n there exist n operators $\boldsymbol{C}$, such that $[\boldsymbol{C}, \boldsymbol{G}] = 0$ holds for all generators $\boldsymbol{G}$ of the group. The operators $\boldsymbol{C}$ are called Casimir operators or Casimir invariants. For instance, the total boson number operator $\boldsymbol{N} = (\boldsymbol{s}^\dagger \cdot \widetilde{\boldsymbol{s}}) + (\boldsymbol{d}^\dagger \cdot \widetilde{\boldsymbol{d}})$[21] is a (linear) Casimir operator of U(6) in the IBM-1 since the generators of U(6) do not change the total boson number N. Smaller subsets of the generators that close on themselves under commutation form a subgroup of U(6). In this fashion, chains of subgroups of U(6) can be constructed. For physical significance, these must necessarily contain the angular momentum algebra O(3) and, thus, the three[22] operators

[18] Initially, a d-boson formulation was employed to the collective Hamiltonian [56, 62]. Subsequent introduction of s bosons yields the favorable U(6) symmetry [63]. Extensions to the model exist, which feature bosons beyond s and d. Such are briefly introduced in Section 2.3.3.

[19] The truncation in the IBM is rather extreme. In the case of rare-earth nuclei, for instance, the Hilbert space of the shell-model incorporates the $1g_{7/2}$ to $1h_{11/2}$ orbitals for protons and the $1h_{9/2}$ to $1i_{13/2}$ orbitals for neutrons. The infamous 3×10^{14} potential 2^+ shell-model states of ^{154}Sm [64] are reduced to merely 26 [44].

[20] A unitary group of dimension n, U(n), has n^2 generators $\boldsymbol{G_i}$ with $i \in \{1, \ldots, n^2\}$ [Sec. 3.4 of [65]].

[21] The scalar product, which is indicated by '$\cdot$', is a special case of the tensor product. It is defined as $(U^{(k)} \cdot V^{(k)}) = (-1)^k \sqrt{2k+1}\,[U^{(k)} \times V^{(k)}]^{(0)}_0 = \sum_\mu (-1)^\mu U^{(k)}_\mu V^{(k)}_\mu$ [42].

[22] An orthogonal group of dimension n, O(n), has $n(n-1)/2$ generators [Sec. 3.4 of [65]].

$\boldsymbol{L}_\mu \propto [\boldsymbol{d}^\dagger \times \widetilde{\boldsymbol{d}}]^{(1)}_\mu$ with $\mu \in \{0, \pm 1\}$. This constraint guarantees that eigenstates of the Hamiltonian are characterized by good angular momentum. Exactly three distinct chains with the required properties can be identified: via the U(5), SU(3), and O(6) groups [Sec. 2.3 of [13]]. The potential subalgebra SU(4), on the other hand, is not explicitly considered since it is isomorphic to O(6).

If the bosons are explicitly interpreted as proton or neutron pairs [66, 67], a richer group structure emerges. For distinction the individual creation and annihilation operators feature an additional label $\rho \in \{\pi, \nu\}$ specifying the microscopic interpretation of the bosons:

$$\boldsymbol{s}^\dagger_\rho, \boldsymbol{d}^\dagger_{\rho,\mu} \qquad \text{and} \qquad \widetilde{\boldsymbol{s}}_\rho, \widetilde{\boldsymbol{d}}_{\rho,\mu} \qquad \text{with} \qquad \mu \in \{0, \pm 1, \pm 2\}. \tag{2.9}$$

This version of the model is known as the IBM-2. The distinction between proton and neutron bosons introduces an additional symmetry called F-spin [66, 67]. It represents the bosonic analogue to isospin[23] and, thus, corresponds to an SU(2) algebra. To each boson in the IBM-2 an F-spin quantum number $F = 1/2$ is assigned and the proton (neutron) boson is defined as the $F_3 = 1/2$ ($F_3 = -1/2$) eigenstate of the F-spin operator. Due to its analogy to angular momentum,[24] the total F-spin of a system consisting of N_π proton bosons and N_ν neutron bosons takes values between $F_{\text{min}} = |N_\pi - N_\nu|/2$ and $F_{\text{max}} = (N_\pi + N_\nu)/2$. States with maximum F-spin are called fully-symmetric states. They are invariant under the pairwise exchange of protons and neutrons and, thus, represent eigenstates of the IBM-1 [68]. States with $F < F_{\text{max}}$ are not symmetric under this exchange and referred to as mixed-symmetry states. A prominent example for such a state is the scissors mode, which is discussed in Section 2.4.

In the IBM-2, the 72 bilinear operators constructed from the boson operators (2.9) generate the Lie algebra of the direct product $\text{U}_\pi(6) \otimes \text{U}_\nu(6)$.[25] Similar to the IBM-1, chains of subalgebras have to be identified, which reduce to the rotation algebra $\text{O}_{\pi+\nu}(3)$. Since protons and neutrons are rotated simultaneously, the three generators

[23] Regarding the isospin, it must still be taken into account that the bosons are composed of two nucleons. For instance, a proton boson is characterized through F-spin by $|F, F_3\rangle = |1/2, +1/2\rangle$ but through isospin by $|T, T_3\rangle = |1, +1\rangle$.

[24] The algebras SU(2) and O(3) are isomorphic [65].

[25] The Lie algebra U(12) is not appropriate because it contains operators which exchange proton and neutron bosons. However, not only the total boson number $N = N_\pi + N_\nu$ has to be conserved but also the two terms (N_π and N_ν) separately.

of $O_{\pi+\nu}(3)$ are given by the sums of the individual generators of $O_\pi(3)$ and $O_\nu(3)$ [Eq. (5.2) of [13]]. However, the first common algebra can be placed earlier in the reduction chain; either $U_{\pi+\nu}(6)$ [Eq. (5.6) ibid.] or $U_{\pi+\nu}(5)$, $SU_{\pi+\nu}(3)$ or $O_{\pi+\nu}(6)$ [Eq. (5.8) ibid.]. In the following, only the first case is considered. The presence of $U_{\pi+\nu}(6)$ guarantees that F-spin is a good quantum number for the Hamiltonians associated with the reduction $U_\pi(6)\otimes U_\nu(6) \supset U_{\pi+\nu}(6)$ [59]. The potential reductions to the angular momentum algebra are

$$
\begin{array}{ccccccccccccc}
 & & & & \curvearrowright & U_{\pi+\nu}(5) & \supset & O_{\pi+\nu}(5) & \curvearrowleft & & & & \\
 & & & & & | & & | & | & & & & \\
 & & & & & \{n_1,n_2\} & & (v_1,v_2) & \alpha & & & & \\
U_\pi(6)\otimes U_\nu(6) & \supset & U_{\pi+\nu}(6) & \supset & SU_{\pi+\nu}(3) & & & & \supset & O_{\pi+\nu}(3) & \supset & O_{\pi+\nu}(2) & \\
| & & | & & | & & & & | & | & & | & \\
[N_\pi]\otimes[N_\pi] & & [N-f,f] & & \beta & (\lambda,\mu) & & & \kappa & L & & M & \\
 & & & & \curvearrowleft & O_{\pi+\nu}(6) & \supset & O_{\pi+\nu}(5) & \curvearrowright & & & & \\
 & & & & & | & & | & | & & & & \\
 & & & & & \langle\sigma_1,\sigma_2\rangle & & (\tau_1,\tau_2) & \gamma & & & &
\end{array}
$$

For each group exists at least one quantum number which remains unaffected by any of the generators. The set of basis states characterized by a particular value of an unchanged quantum number is called an irreducible representation of the group. Since the generators of a group cannot connect different irreducible representations, the Casimir operators are by construction diagonal in this basis. Thus, they conserve all quantum numbers including those of all subgroups. In fact, the eigenvalues of Casimir operators depend only on the conserved quantum numbers of the respective subgroup. In the above reduction scheme the quantum numbers labeling the irreducible representations are given below each chain.[26] Since the reduction to $O_{\pi+\nu}(3)$ is unique in none of the chains, additional quantum numbers α, κ, and γ are introduced to resolve the ambiguity.[27] Similarly, β is needed to completely specify the reduction from $U_{\pi+\nu}(6)$ to $SU_{\pi+\nu}(3)$.

[26] The names of the individual variables are based upon Ref. [59].

[27] In the context of the present work, especially the additional quantum number κ is of importance since it distinguishes between the β ($\kappa = 0$) and γ ($\kappa = 2$) bands of rotational nuclei.

2.3.2. Physical operators and dynamical symmetries

The Hamiltonian of the Interacting Boson Model is formulated in terms of boson creation and annihilation operators [cf. Eq. (2.9)]. Based on a phenomenological analysis of collective nuclear states, it is limited to one- and two-body contributions [Sec. 4.5.1 of [13]][28] and conserves the boson numbers N_π and N_ν. As indicated in the preceding Section, the most general Hamiltonian can be reformulated in terms of Casimir operators as

$$\begin{aligned}\boldsymbol{H} = E_0 &+ a\boldsymbol{C}_1(\mathrm{U}_{\pi+\nu}(6)) + a'\boldsymbol{C}_2(\mathrm{U}_{\pi+\nu}(6)) \\ &+ \eta\boldsymbol{C}_2(\mathrm{O}_{\pi+\nu}(6)) + \epsilon\boldsymbol{C}_1(\mathrm{U}_{\pi+\nu}(5)) + \alpha\boldsymbol{C}_2(\mathrm{U}_{\pi+\nu}(5)) \\ &+ \beta\boldsymbol{C}_2(\mathrm{O}_{\pi+\nu}(5)) + \delta\boldsymbol{C}_2(\mathrm{SU}_{\pi+\nu}(3)) + \gamma\boldsymbol{C}_2(\mathrm{O}_{\pi+\nu}(3)).\end{aligned} \tag{2.10}$$

The subscripts of the operators denote their order in the generators of the respective group. The first three terms are functions of the boson numbers only. Since they only contribute to binding energies, these terms can be omitted if solely intrinsic excitations are of interest. Hamiltonian (2.10) contains Casimir operators from all subchains and, thus, does not belong to any of them. Instead, it creates wave functions which are admixtures of different basis states regardless of the algebraic subchain they are expressed in. If the factors η, ϵ, α, β, δ, and γ are chosen such that the Hamiltonian consists solely of Casimir operators of a specific chain, it is diagonal in a basis defined by the respective representation labels. In this case, which is known as a dynamical symmetry, the eigenvalue problem posed by the Hamiltonian can be solved analytically [73–75]. Explicit expressions for the energy eigenvalues are compiled in Ref. [59].

However, only relatively few nuclei are well-described within a dynamical symmetry. For instance, O(6) symmetry manifests itself in ^{196}Pt [76]. In the SU(3) limit, states with the same angular momentum belonging to the bands with quantum numbers $(\lambda, \mu) = (2N-4, 2)$[29] are required to be exactly degenerate. Furthermore, $E2$ transitions between these bands and the ground-state band are forbidden. These requirements are approximately met by the ytterbium and hafnium nuclei with neutron

[28] In the IBM-1, on the other hand, higher-order terms might be needed in special cases; potentially due to the reduced boson space [Sec. 4.5.1 of [13]]. For instance, rigid triaxiality can be introduced by means of a cubic term in the Hamiltonian [69–72].

[29] These bands are commonly referred to as the β and γ band.

number $N = 104$ [77].[30] Even the textbook examples for the U(5) limit, the cadmium isotopes [13, 44], exhibit an ambiguous structure. While a U(5)-like multiplet structure was reported [80], deviating behavior of low-energy states was attributed to intruder configurations [62, 81]. For these latter states, the U(5) interpretation does not hold.[31] Although some features of dynamical symmetries might be realized in selected nuclei, a practical calculation requires a more universal Hamiltonian. Concurrently, the number of free parameters in the Hamiltonian is reduced by selection of sensitive contributions. The three main components of the general IBM-2 Hamiltonian

$$\boldsymbol{H} = \epsilon_\pi \boldsymbol{n}_{d_\pi} + \epsilon_\nu \boldsymbol{n}_{d_\nu} + \kappa(\boldsymbol{Q}_\pi^{\chi_\pi} \cdot \boldsymbol{Q}_\nu^{\chi_\nu}) + \boldsymbol{M}_{\pi\nu}(\xi_1, \xi_2, \xi_3)$$

are microscopically motivated [86]. The first two terms are inspired by the pairing interaction [87] between identical nucleons. They feature the sum of the d-boson number operators [Eq. (4.35) of [13]]

$$\boldsymbol{n}_{d_\rho} = (\boldsymbol{d}_\rho^\dagger \cdot \widetilde{\boldsymbol{d}}_\rho)$$

for proton and neutron bosons $\rho \in \{\pi, \nu\}$, which is scaled by the d-boson energy ϵ_ρ. It spans a phonon-like multiplet structure as approximately found in collective vibrational nuclei. The U(5) basis states are strongly mixed by introduction of a quadrupole-quadrupole interaction using the quadrupole operator [Eq. (4.39) ibid.]

$$\boldsymbol{Q}_\rho^{\chi_\rho} = [\boldsymbol{d}_\rho^\dagger \times \widetilde{\boldsymbol{s}}_\rho + \boldsymbol{s}_\rho^\dagger \times \widetilde{\boldsymbol{d}}_\rho]^{(2)} + \chi_\rho [\boldsymbol{d}_\rho^\dagger \times \widetilde{\boldsymbol{d}}_\rho]^{(2)}. \tag{2.11}$$

It mimics the quadrupole force between non-identical nucleons, which is the major driver for nuclear deformation [8]. The quadrupole-quadrupole interaction alone creates a spectrum of rotational bands.[32] In the previous Section, the notion of mixed-symmetry states has been introduced. These represent a completely new class of nuclear valence-shell excitations with non-trivial symmetry properties characterized by $F < F_{\max}$ [14]. Apart from totally symmetric states with maximum F-spin, states

[30] The nucleus ^{156}Gd, which is often described as SU(3)-like [78], exhibits an appropriate energy spectrum [Fig. 2.6 of [13]], but features comparably strong $E2$ transitions between γ and ground-state bands; e.g. $B(E2; 2_\gamma^+ \to 2_1^+) = 7.24(25)$ W.u. [79].

[31] From a formal point of view, the description of ^{110}Cd within the U(5) limit has at least partially been recovered by an approach [82] based on the U(5) partial dynamical symmetry [83–85].

[32] Strictly speaking, it represents the special case of a deformed rotor since all rotational bands within a given irreducible representation are degenerate.

with $F_{\max}-1$ are lowest in excitation energy. In contrast to the operators introduced above the Majorana interaction [Eq. (4.111) of [61]]

$$\begin{aligned}\boldsymbol{M}_{\pi\nu}(\xi_1,\xi_2,\xi_3) = \frac{\xi_2}{2}[\boldsymbol{d}^\dagger_\pi \times \boldsymbol{s}^\dagger_\nu - \boldsymbol{d}^\dagger_\nu \times \boldsymbol{s}^\dagger_\pi]^{(2)} \cdot [\widetilde{\boldsymbol{d}}_\pi \times \widetilde{\boldsymbol{s}}_\nu - \widetilde{\boldsymbol{d}}_\nu \times \widetilde{\boldsymbol{s}}_\pi]^{(2)} \\ + \sum_{k=1,3} \xi_k [\boldsymbol{d}^\dagger_\pi \times \boldsymbol{d}^\dagger_\nu]^{(k)} \cdot [\widetilde{\boldsymbol{d}}_\nu \times \widetilde{\boldsymbol{d}}_\pi]^{(k)}\end{aligned} \tag{2.12}$$

mixes proton- and neutron-boson operators. Hence, it only affects configurations with nontrivial symmetry properties, i.e. states with $F \in [F_{\min}, F_{\max}) \cap \mathbb{N}$. In applications, the Majorana interaction is phenomenologically used to shift these mixed-symmetry states to higher excitation energies [88]. In this sense, it takes the role of a symmetry energy [89] in geometrical models [90, 91]. Its parameters ξ_i ($i \in \{1,2,3\}$) can be determined from precision information on transitions between mixed-symmetry states and other intrinsic excitations modes [92].

For the modeling of electromagnetic transitions dedicated transition operators are introduced. In the IBM-2, they are conventionally written as the sum of proton and neutron parts $\boldsymbol{T} = t_\pi \boldsymbol{T}_\pi + t_\nu \boldsymbol{T}_\nu$ [59], where t_π and t_ν are proton and neutron effective charges, respectively. For magnetic dipole transitions the $M1$ operator [Eq. (4.41) of [13]]

$$\boldsymbol{T}(M1) = \sqrt{\frac{3}{4\pi}}(g_\pi \boldsymbol{L}_\pi + g_\nu \boldsymbol{L}_\nu) \tag{2.13}$$

is used with the boson effective g-factors g_ρ and the angular momentum operator [Eq. (4.35) ibid.]

$$\boldsymbol{L}_\rho = \sqrt{10}[\boldsymbol{d}^\dagger_\rho \widetilde{\boldsymbol{d}}_\rho]^{(1)}. \tag{2.14}$$

Since $M1$ transitions are forbidden between states with maximum F-spin,[33] they serve as fingerprint signatures for the identification of mixed-symmetry states. Analoguous

[33] Rewriting Eq. (2.13) in terms of the total angular momentum $\boldsymbol{L}_{\text{tot}} = \boldsymbol{L}_\pi + \boldsymbol{L}_\nu$ yields the expression $\boldsymbol{T}(M1) = \sqrt{3/(4\pi)}[(g_\pi N_\pi + g_\nu N_\nu)/N \boldsymbol{L}_{\text{tot}} + (g_\pi - g_\nu) N_\pi N_\nu / N(\boldsymbol{L}_\pi/N_\pi - \boldsymbol{L}_\nu/N_\nu)]$ [15]. Since $\boldsymbol{L}_{\text{tot}}$ is diagonal in the IBM-2 it cannot induce transitions between different states. Also the second term vanishes for transitions between states with maximum F-spin [Eq. (2.8) of [59]].

to the $M1$ case, the $E2$ transition operator involves effective quadrupole boson charges e_ρ as scaling for the quadrupole operators (2.11). It is given by [Eq. (4.39) of [13]]

$$\boldsymbol{T}(E2) = e_\pi \boldsymbol{Q}_\pi^{\chi_\pi} + e_\nu \boldsymbol{Q}_\nu^{\chi_\nu}. \tag{2.15}$$

For practical calculations using the IBM two conventions are adopted. First, the same quadrupole operators (2.11) are used in the quadrupole-quadrupole interaction of the Hamiltonian as well as in the $E2$ transition operator (2.15). This is known as the extended consistent-Q formalism [93–95]. In addition, F-spin symmetry is requested by treating proton and neutron bosons on equal footing. As a consequence, the d-boson energies ϵ_ρ and parameters χ_ρ are chosen equal for proton and neutron bosons. Furthermore, a quadrupole-quadrupole interaction between identical bosons is introduced for symmetry reasons. In summary, this yields the adopted F-spin symmetric Hamiltonian

$$\boldsymbol{H} = \epsilon(\boldsymbol{n}_{d_\pi} + \boldsymbol{n}_{d_\nu}) + \kappa(\boldsymbol{Q}_\pi^\chi + \boldsymbol{Q}_\nu^\chi) \cdot (\boldsymbol{Q}_\pi^\chi + \boldsymbol{Q}_\nu^\chi) + \boldsymbol{M}_{\pi\nu}(\xi_1, \xi_2, \xi_3). \tag{2.16}$$

By construction, the above Hamiltonian commutes with the F-spin operators $\boldsymbol{F}_3$ and $\boldsymbol{F}_\pm$. In particular, it also commutes with $\boldsymbol{F}^2$, i.e. all eigenstates of this Hamiltonian have good F-spin quantum number. Thus, no $M1$ transitions occur between states with maximum F-spin.[34] Naturally, Hamiltonian (2.16) trivially contains the discussed dynamical symmetries for $\kappa = 0$ [U(5)], $\epsilon = 0$ and $\chi = -\sqrt{7}/2$ [SU(3)], and $\epsilon = 0$ and $\chi = 0$ [O(6)].

2.3.3. Extensions and connection to other models

Historically, the IBM was proposed from a purely phenomenological viewpoint in order to describe energy spectra of vibrational [58] and rotational nuclei [63, 74]. It enables the treatment of medium-mass and heavy collective nuclei for which the dimension of the shell-model space becomes intractable. The inherent truncation is both effective, since the Hilbert space is reduced to manageable dimensions, and reasonable, since

[34] In reality, such $M1$ transitions are observed. However, they are small, leaving F-spin an approximate quantum number. Further experimental evidence for the goodness of F-spin is the occurrence of F-spin multiplets [96, 97]. Other studies, however, suggest that there is already a considerable mixed-symmetric contribution to the ground state [98]. This might also hint at constant admixtures in an F-spin multiplet [Sec. 5.9 of [13]].

the physical significance is preserved. In this sense, the IBM is characterized by a degree of microscopicity between the shell model and the collective model of Bohr and Mottelson. Using the former a microscopic justification of the mentioned truncation can be derived [[67, 86, 99] and Sec. 4 of [61]].[35] It features states consisting of collective pairs of like valence nucleons, which are projected onto good seniority [42] and subsequently mapped onto boson states. Naturally, this approach only yields a foundation for the IBM-2.

The most basic versions of the Interacting Boson Model, i.e. the IBM-1 and -2, are restricted to s and d bosons. Besides these a rich tapestry of deduced models emerged which incorporate additional bosons.[36] Examples include g ($J = 4$) bosons [[100] and Sec. 6.2 of [61]] for a consideration of the hexadecapole degree of freedom[37] or p ($J = 1$) and f ($J = 3$) bosons [[100, 105] and Sec. 6.3 of [61]] for the description of negative parity states.[38] All of these approaches are characterized by the occurrence of dynamical symmetries. As mentioned in Section 2.3.2, dynamical symmetries impose strict conditions such as degenerate energies for bands belonging to the same SU(3) irreducible representation. Introducing a partial symmetry breaking, favorable properties can be retained for some eigenstates while other states are admixtures of different irreducible representations. This is known as a partial dynamical symmetry (PDS) [83–85].[39] If, on the other hand, excited states of odd-even, even-odd or odd-odd nuclei are of interest, a purely bosonic model is no longer suitable.[40] In analogy to

[35] A related reason for exploring the shell-model foundations of the IBM is the desire to provide a simple access to collective states without diagonalizing the shell-model Hamiltonian matrix. In this context it has to be noted that the IBM-1 cannot have a direct shell-model basis due to the Pauli principle and the derived symmetry properties [Sec. 37 of [64]].

[36] Neither the list of extensions mentioned nor the associated References claim to be complete. Rather, they represent an illustrative selection.

[37] Experimental examples are $K^\pi = 4^+$ bands of ^{156}Gd [69] and ^{168}Er [101, 102] or strong $M1$ transitions between 4^+ states of ^{94}Mo [103, 104].

[38] Possible applications are the description of octupole modes [106, 107], or even α clustering in rare-earth nuclei [108] and the giant-dipole resonance [11] of deformed nuclei [109].

[39] In fact, there are three different types of partial dynamical symmetries [85, 110]: (i) some states have all properties of a dynamical symmetry, (ii) all states have some properties, and (iii) some states have some properties. A specific example of type (i) is the SU(3) PDS of Refs. [84, 111–113]. The O(5) PDS of type (ii) is, for instance, employed to transitional nuclei in the Ru-Pd [114] and Xe-Ba regions [72]. Ultimately, an O(6) PDS of type (iii) might be found in the experimental spectrum of ^{162}Dy [110].

[40] In fact, odd-odd nuclei can be discussed in the framework of the IBM-3 [115] which features an additional boson formed by a proton-neutron pair. This inclusion of the isospin degree of freedom allows the treatment of light nuclei whose protons and neutrons might occupy the same single-particle orbits [Sec. 7 of [13]].

the particle-rotor model [App. 4A of [4]], the Interacting Boson-Fermion Model [116] couples a collective core, which is described by a standard IBM Hamiltonian, to a fermion by virtue of some interaction term.

Due to its valence-space origin, many aspects of the IBM reflect an influence of the boson number. This is a clear difference to geometric models in the sense of Bohr and Mottelson or Gneuss and Greiner. For instance, in the U(5) dynamical symmetry

$$\frac{B(E2;2_2^+ \to 2_1^+)}{B(E2;2_1^+ \to 0_1^+)} = 2\frac{N-1}{N} = R_{\text{phonon}}\frac{N-1}{N}$$

is obtained [Eq. (6.63) of [44]], where $R_{\text{phonon}} = 2$ refers to the quadrupole-phonon picture. For small boson numbers N the deviations from the geometric result can be significant. Likewise,

$$\frac{B(E2;2_\gamma^+ \to 2_1^+)}{B(E2;2_\gamma^+ \to 0_1^+)} = \frac{10}{7}\frac{2N+3}{2N} = R_{\text{Alaga}}\frac{2N+3}{2N}$$

is obtained for transitions between the γ-vibrational $(\lambda,\mu) = (2N-4,2)$ and ground-state $(2N,0)$ bands in the SU(3) dynamical symmetry. Here, R_{Alaga} is the result obtained in a geometrical picture of a rigid rotor and for separable matrix elements (cf. Section 6.1.2). In both examples the results in the geometric picture are restored for infinite boson number. Such finite-size effects are a characteristic of the IBM and can have further drastic effects such as a cutoff in possible angular momentum quantum numbers.[41]

In order to place the IBM in a more descriptive context, its dynamical symmetries are conveniently related to equilibrium shapes of geometrical models. The latter might be solutions to the Bohr Hamiltonian [117, 118] for different choices of the potential [119]; the harmonic oscillator [120] [U(5)], the displaced harmonic oscillator [118] [SU(3)], and the anharmonic oscillator [121] [O(6)]. In order to bridge the gap to the shape variables β and γ of the Bohr Hamiltonian, the classical limit of the IBM Hamiltonian has to be considered [122–125]. This procedure yields expressions for potential energy surfaces of β and γ depending on the parameters of the IBM Hamiltonian (cf. Section 2.5.2).

[41] A system of N bosons can have a maximum of $n_d = N$ d bosons and, thus, in the maximally aligned configuration states with an angular momentum quantum number $J = 2N$.

2.4. The $M1$ scissors mode

The IBM-2 contains, as indicated in Sections 2.3.1 and 2.3.2, a new class of collective excitation modes which are not completely symmetric in the proton and neutron degrees of freedom [14, 126]. The most prominent examples for such mixed-symmetry states are the one-quadrupole phonon 2^+_{ms} state of weakly deformed, vibrational, and transitional nuclei [15] and the 1^+_{sc} scissors mode of medium-heavy and heavy deformed nuclei [17]. Especially the latter stands out since no dipole states are allowed in the IBM-1. In the following, its basic features are introduced by virtue of simple considerations in the framework of the IBM-2 [Sec. 4.12. of [61]].

Starting from a system comprising one proton and neutron boson each, a general expression for the ground state is given by the linear combination

$$|0^+_1\rangle = \alpha|s_\pi s_\nu; 0^+\rangle + \beta|d_\pi d_\nu; 0^+\rangle$$

with normalized amplitudes α and β. It is symmetric under an exchange of protons and neutrons and, thus, characterized by maximum F-spin quantum number $F_{\mathrm{max}} = 1$. The simplest operator which changes the angular momentum quantum number by one unit is the one-body angular momentum operator [cf. Eq. (2.14)]. Since transition operators in the IBM-2 contain separate proton and neutron parts, the operator $\boldsymbol{T}_1 = \boldsymbol{L}_\pi + \boldsymbol{L}_\nu$ is considered. This is the total angular momentum operator, whose action on the ground state is given by

$$\boldsymbol{T}_1|0^+_1\rangle = \beta\boldsymbol{T}_1|d_\pi d_\nu; 0^+\rangle = 0.$$

An operator $\boldsymbol{T}_2 = \boldsymbol{L}_\pi - \boldsymbol{L}_\nu$, on the other hand, generates an opposite rotation of proton and neutron bosons. Applied to the ground state, it breaks its proton-neutron symmetry and creates a 1^+ state with $F = F_{\mathrm{max}} - 1$, i.e.

$$\boldsymbol{T}_2|0^+_1\rangle = \beta\boldsymbol{T}_2|d_\pi d_\nu; 0^+\rangle \propto \beta|d_\pi d_\nu; 1^+\rangle.$$

This magnetic dipole state is antisymmetric since its sign changes if proton and neutron bosons are exchanged.[42] It is commonly referred to as the scissors mode and characterized by an excitation strength of $2-3\,\mu_N^2$ [125, 126] due to its valence-shell

[42] The operator $\boldsymbol{T}_1$ cannot produce the mixed-symmetric 1^+ state from the fully-symmetric ground state. It is a generator of $\mathrm{U}_{\pi+\nu}(6)$ and, thus, does not connect different irreducible representations.

origin. The deduced nature[43] corroborates results obtained from geometrical models which are discussed in the following.[44]

Low-energy excitation modes of all nucleons are well described within the collective model of Bohr and Mottelson [4]. They are characterized by in-phase (isoscalar) variations of the proton and neutron densities. Such modes are energetically favored over antisymmetric (isovector) excitations due to the symmetry energy. Nevertheless, even nonsymmetric excitations of spherical nuclei were considered early on [135–137]. Using extensions to the Bohr-Mottelson ansatz such as distinct proton and neutron degrees of freedom, the existence of nonsymmetric modes was predicted also for deformed nuclei [138–140]. In the geometric two-rotor model [139, 140] the scissors mode manifests itself as collective orbital $M1$ strength generated in the out-of-phase rotational oscillation of the deformed proton and neutron density distributions. These approaches predicted excitation energies between 3 and 5 MeV and fairly large $M1$ excitation strengths between 9 and $18\,\mu_N^2$ [139, 141–143].

Since the nuclear scissors mode is rooted in the quadrupole deformation of the proton and neutron subsystems, first experimental endeavors focused on quadrupole deformed rare-earth nuclei [16, 144, 145]. Subsequently, it has been studied extensively in inelastic electron-scattering (e, e'), photon scattering (γ, γ'), and neutron-scattering $(n, n'\gamma)$ experiments[45] [17, 147–150, and Refs. therein]. In the process, scissors-like excitation modes were also established in vibrational [[15] and Sec. VI of [17]], transitional [151, 152], odd-mass [[153–155] and Sec. IV of [17]], and γ-soft [156, 157] nuclei. The wealth of data on the scissors mode enabled the systematical analysis of its properties as a function of other nuclear characteristics. Due to its quadrupole-collective nature, the mean excitation energy of the scissors mode shows a smooth dependence on the nuclear mass number A and the quadrupole-deformation parameter δ[46] [141, 148, 159]. The total $M1$ strength, on the other hand, is correlated with the low-lying collective $E2$ strength [148, 160, 161] and, thus, to δ^2 [152, 162–164].

[43] Orbital out-of-phase oscillations can occur in generic coupled two-component many-body quantum systems. Besides atomic nuclei, Bose-Einstein condensates [127, 128], Fermi gases [129], metallic clusters [130–132], deformed quantum dots [133], and dipolar quantum droplets [134] are examples.

[44] The theoretical prediction of the scissors mode as well as its experimental discovery led to countless further theoretical, phenomenological, and experimental studies. The list of References given in the present Section represents a personal selection and is by far not exhaustive.

[45] States of the scissors mode are not observed in (p, p') experiments [146]. This shows that the scissors mode is indeed excited by the orbital part of the $M1$ transition operator [Eq. (28) of [17]].

[46] In the present work, the nuclear deformation parameter is denoted δ [Eq. (4-73) of [4]]. The relations of δ to other parametrizations are collected in Sec. 6.4 of [158].

Despite the scissors mode's quadrupole-collective nature, its $E2$ properties were mostly unknown until recently [24]. In principle, the latter can be divided into two classes. In well-deformed nuclei the 1^+_{sc} state is the band head of the scissors mode's $K = 1$ rotational band. For the excitation strength of its 2^+_{sc} state predictions exist from various geometrical models. These amount to a few Weisskopf units in the rare-earth region [139, 142, 143]. In the IBM-2, the excitation of a 2^+ mixed-symmetry state from the ground state is a $\Delta F = 1$ transition and, thus, its strength is proportional to the difference of the quadrupole boson charges in the $E2$ transition operator (2.15). Likewise, these are also accessible through the $E2$ component of the transition connecting the 1^+_{sc} and 2^+_1 states.[47] Hitherto, local values for the quadrupole charges have only been determined for the transitional nucleus ^{152}Sm and the quadrupole-deformed nucleus ^{156}Gd [23, 24].

There exist further approaches that extend the concept of the nuclear scissors mode. For instance, the emergence of a soft scissors mode due to the influence of a neutron skin is described in the IBM-2 [165] and a geometrical approach [166]. In analogy to multivibrational states, so-called overtones of the scissors mode are predicted in the framework of the projected shell model [167] and the two-rotor model [168, 169]. The lowest of these additional levels have quantum numbers $J^\pi = 0^+$ and 2^+ and are expected to reside at roughly 6 MeV for rare-earth nuclei. In a more exotic approach, negative-parity states are obtained if the rotors of the TRM can have negative $\mathscr{R}$ symmetry quantum numbers [170].

[47] Precisely, in the F-spin limit of the SU(3) dynamical symmetry the quadrupole boson charges can be determined from the knowledge of at least one $E2$ transition between two fully-symmetric states and one $E2$ transition between a fully-symmetric and mixed-symmetry state [59].

2.5. Quantum phase transitions

The description of quantum phase transitions (QPTs) borrows many concepts from the theory of classical phase transitions. The latter are rooted in the thermodynamics of macroscopic systems and describe transitions between different phases of a medium which are triggered by a change of external conditions such as temperature or pressure. Since entropy vanishes at zero temperature,[48] no classical (thermal) phase transition is possible in this realm. Considering a non temperature-like parameter instead, a quantum-phase transition between different phases of the underlying many-body system can occur. Further examples of QPTs include transitions between ferro- and para- or antiferromagnetism of diverse atomic quantum systems [Sec. 1.3 of [171]]. In the context of nuclear physics, equilibrium shapes of atomic nuclei are suitable surrogates for the mentioned phases. The following discussion on phenomenology and modeling of QPTs in the framework of the IBM is based on Refs. [172–175].

2.5.1. Phenomenology

The equilibrium shapes of even-even nuclei, which serve as order parameters of the QPT, are not directly accessible. Instead, they reveal themselves through characteristic observables such as the $R_{4/2}$ ratio, which is defined as the ratio of the energy of the 4_1^+ state to the energy of the 2_1^+ state, or the transition strength between the latter state and the ground state $B(E2; 2_1^+ \to 0_1^+)$. Panel (a) of Fig. 2.3 shows the former as a function of the neutron number N for even-even nuclei of the cerium to dysprosium isotopic chains. At and close to the $N = 82$ closed neutron shell, the low-energy structure is determined by the underlying shell structure. With increasing neutron number the structure is dictated by one of three idealized paradigms of collectivity; the spherical vibrator [120], the axially-symmetric rotor [118], and the γ-soft rotor [121]. In the present case, a transition between the first two is observed between $N = 88$ and $N = 90$ in the $R_{4/2}$ systematics. Since the neutron number is an integer quantity, it is no suitable control parameter. Instead, it might be replaced by continuous proxies; either another observable such as $E(2_1^+)$ or a model parameter (cf. Section 2.5.2). A universal description for the collectivity of nuclei is the factor $P = N_p N_n/(N_p+N_n)$ [173, 176] where N_p and N_n are the numbers of valence nucleons counted to the nearest

[48] This is exactly the statement of the third law of thermodynamics.

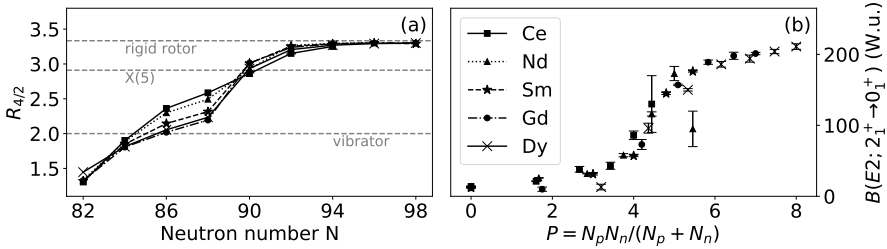

Figure 2.3.: Fingerprint observables illustrating the phase transition at $N = 90$. The evolution of the $R_{4/2}$ ratio with neutron number exhibits a sharp increase between $N = 88$ and $N = 90$ for the Sm, Gd, and Dy isotopic chains, whereas the transition is much smoother for the Ce and Nd isotopes [panel (a)]. Expectations for spherical vibrators, X(5) critical-point nuclei, and rigid rotors for comparison are indicated in gray. Likewise, transitional behavior is found at $P \approx 5$ from $B(E2; 2_1^+ \to 0_1^+)$ systematics [panel (b)]. Data are taken from the Nuclear Data Sheets [79, 177–188].

closed shells. Irrespective of mass region, transitional behavior is semi-empirically found at $P \approx 5$ [176]. This becomes evident, for example, from panel (b) of Fig. 2.3, which shows the evolution of $B(E2; 2_1^+ \to 0_1^+)$ with continuous P for the above isotopic chains.

2.5.2. Quantum-phase transitions in the Interacting Boson Model

In the framework of the Interacting Boson Model (cf. Section 2.3), the mentioned paradigms correspond to the dynamical symmetries U(5), SU(3), and O(6) (cf. Section 2.3.2). A simple IBM-1 Hamiltonian which traverses the triangle spanned by these symmetries is given by [172, 173]

$$\boldsymbol{H} = C\left[(1-\zeta)\boldsymbol{n}_d - \frac{\zeta}{4N}(\boldsymbol{Q}^\chi \cdot \boldsymbol{Q}^\chi)\right] \qquad \text{with} \qquad \zeta = \frac{4N}{4N + {}^{\epsilon}/_{\kappa}}. \tag{2.17}$$

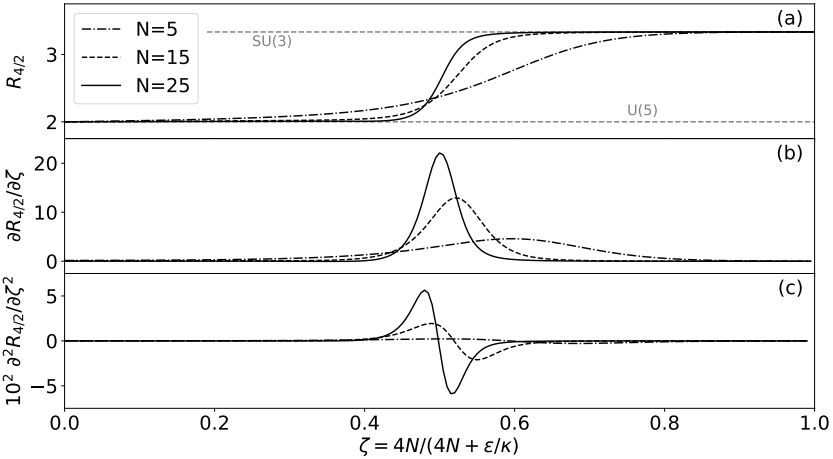

Figure 2.4.: Evolution of the $R_{4/2}$ ratio with ζ in the IBM for different boson numbers and $\chi = -\sqrt{7}/2$ alongside the first [panel (b)] and second [panel (c)] partial derivatives. The phase transition is smoothed out due to the finite size of the considered systems. First-order nature can be deduced from the occurrence of a discontinuity in the first partial derivative. Its location as well as the root of the second derivative yield information on the critical point [189].

It employs the extended consistent Q formalism [93–95] and, thus, has two free parameters.[49] Most importantly, $\zeta \in [0,1]$ mediates between spherical symmetry due to the d-boson number operator $\boldsymbol{n}_d$ ($\zeta = 0$) and deformed configurations driven by the quadrupole-quadrupole interaction ($\zeta = 1$). Furthermore, ζ is an appropriate continuous control parameter in the IBM description to QPTs. Panel (a) of Fig. 2.4 shows the evolution of the $R_{4/2}$ ratio as a function of ζ for different boson numbers using Hamiltonian (2.17) with $\chi = -\sqrt{7}/2$. The latter choice selects the U(5)-SU(3) leg of the symmetry triangle. The similarity to the experimental systematics from panel (a) of Fig. 2.3 is unmistakable.

[49]The scaling parameter C can be expressed in terms of ϵ and κ through $C = \epsilon - 4N\kappa$ [173].

Unlike macroscopic phase transitions, those in nuclei are damped by the finite number of valence particles. In detail, it becomes also clear that this finite-N effect is at least partially responsible[50] for the smoother transition in the cerium and neodymium isotopes compared to samarium, gadolinium, and dysprosium. In order to pinpoint type and critical point of the QPT, the concept of the Ehrenfest classification is adopted. Panels (b) and (c) of Fig. 2.4 show the first and second partial derivatives of the order parameter $R_{4/2}$ with the control parameter ζ, respectively. In the classical limit ($N \to \infty$) the first derivative exhibits a discontinuity indicating a first-order quantum phase transition. The extremum in the first partial derivative – or equivalently the root of the second partial derivative – indicates the location of the QPT's critical point [189].[51] Alternatively, it can be exploited that critical points correspond to minima in the potential energy. Using the coherent-state formalism [122–124] the scaled potential energy surface of Hamiltonian (2.17) in terms of the intrinsic shape variables β[52] and γ is given by [197, 198]

$$\begin{aligned}\frac{E(\beta,\gamma)}{CN} = \frac{\beta^2}{1+\beta^2}\left[(1-\zeta)-(\chi^2+1)\frac{\zeta}{4N}\right]-\frac{5\zeta}{4N(1+\beta^2)} \\ -\frac{\zeta(N-1)}{4N(1+\beta^2)}\left[4\beta^2-4\sqrt{\frac{2}{7}}\chi\beta^3\cos 3\gamma+\frac{2}{7}\chi^2\beta^4\right].\end{aligned} \tag{2.18}$$

Its evolution across the QPT is illustrated in Fig. 2.5 for $N = 10$ and $\chi = -\sqrt{7}/2$. For small (large) values of ζ a spherical (deformed) minimum exists at $\beta = 0$ ($\beta > 0$). In the transitional region both minima coexist in a small N-dependent range of ζ values. As a result, three approximate signatures for the critical point are conceivable: the advent of the deformed minimum, degeneracy of both minima, or the disappearance of the spherical minimum.[53] With incipient γ-softness ($\chi \in]-\sqrt{7}/2, 0[$) the coexistence

[50] The influence of γ-softness on the QPT has been discussed with respect to ^{148}Ce [190]. In the schematic illustration of Fig. 2.4 this contribution has been neglected by choosing $\chi = -\sqrt{7}/2$.

[51] This statement is fulfilled for a variety of additional observables [189] such as quadrupole shape invariants [191–193] and wave functions [194, 195].

[52] In the present context, β does not coincide with the quadrupole deformation parameter β_2 in the sense of Bohr and Mottelson [4, 117]. Instead, the latter is much smaller. The numerical values estimated from the relation $\beta_2 = 1.18(2N/A)\beta$ should be taken with a grain of salt since they involve gross assumptions [196].

[53] Strictly speaking, the point of degeneracy is the actual critical point. The others are also known as the spinodal and antispinodal points [198]. However, all three points are – irrespective of N – close in ζ and, thus, basically indistinguishable for real nuclei. As a consequence, the requirement of a saddle point at $\beta = 0$, i.e. $\partial^2 E(\beta,\gamma)/\partial\zeta^2|_{\beta=0} = 0$, is often used as a criterion [189].

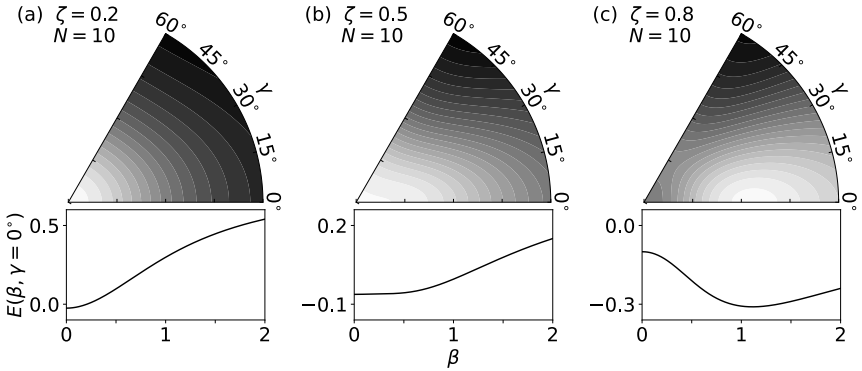

Figure 2.5.: Potential energy surfaces (2.18) obtained from Hamiltonian (2.17) using the coherent-state formalism. They depict the situation prior to [panel (a)], at [panel (b)], and after [panel (c)] the critical point. The color code ranges from white (small) to black (large) and is independent for each panel. The lower figures show the sectional graphs at $\gamma = 0°$, i.e. $\chi = -\sqrt{7}/2$, illustrating the structural evolution in terms of two competing minima in the potential energy.

region shrinks [197], culminating in the second-order QPT between U(5) and O(6) at $\zeta = N/(2N-2)$ [189, 199, 200]. In contrast, no phase transition is found between SU(3) and O(6) in the standard version of the symmetry triangle [123]. If, however, axially-symmetric, oblate deformation, which is represented by the group $\overline{\mathrm{SU(3)}}$ ($\chi = +\sqrt{7}/2$), is included, a first-order quantum-phase transition from prolate to oblate shapes is encountered [201]. This leaves O(6) ($\chi = 0$) a critical-point symmetry and the critical point of the U(5)-O(6) QPT a triple point of nuclear deformation [202, 203] in which sphericity as well as prolate and oblate deformation coexist.

2.5.3. Signatures of phase transitions from the scissors mode

While Fig. 2.3 of Section 2.5.1 shows the influence of a quantum phase transition on two of the most fundamental observables, a plethora of additional signatures has been studied. The majority of those features properties of low-lying, quadrupole-collective states such as excitation energies, transition strengths, and ratios thereof.[54] The Interacting Boson Model is capable of describing this evolution both qualitatively and quantitatively. For mixed-symmetry states, however, this comparison is complicated by the scarcity of precision data, which has both physical and technical reasons.

In the framework of the IBM-2, the scissors mode emerges as a single collective state whose excitation energy is controlled by the parameters of the Majorana operator (2.12) in the Hamiltonian. In the U(5) and SU(3) dynamical symmetries, its excitation strength from the ground state is given by the analytical expressions [59]

$$\begin{aligned} &\text{U(5):} && B(M1;0_1^+ \to 1_{\text{sc}}^+) = 0 \text{ and} \\ &\text{SU(3):} && B(M1;0_1^+ \to 1_{\text{sc}}^+) = \frac{3}{4\pi}(g_\nu - g_\pi)^2 \frac{8}{2N-1} N_\nu N_\pi, \end{aligned} \tag{2.19}$$

respectively. In the former case the $M1$ matrix element to the ground state vanishes due to the scissors mode's two-phonon nature.[55] From these estimates it is expected that scissors-mode states are only weakly excited in spherical vibrators and strongly in axially-symmetric, quadrupole-deformed nuclei. In real nuclei, however, the collective excitation strength is distributed over several isolated 1^+ states.[56] For a meaningful analysis a proxy state is constructed. It resides at the mean excitation energy [148, 150, 152, 212]

$$\overline{E}(1_{\text{sc}}^+) = \frac{\sum_i E_i B(M1;0_1^+ \to 1_i^+)}{\sum_i B(M1;0_1^+ \to 1_i^+)} \tag{2.20}$$

[54] Examples include $E(0_2^+)$, $B(E2;2_3^+ \to 0_2^+)/B(E2;2_1^+ \to 0_1^+)$ [197], and the $E0$ transition strength $\rho^2(E0)$ [204–206].

[55] To be precise, the scissors mode has in U(5) the explicit expression $|d_\pi d_\nu;1^+\rangle$ [59] and application of the $M1$ operator (2.13) to the U(5) ground state, which is an s-boson condensate, yields zero.

[56] This fragmentation has been studied in microscopic models such as QRPA [207], HFB+RPA [208] or the pseudo-SU(3) shell model [209, 210], among others. Starting from collective models such as the IBM the underlying mechanism has been described as a mixing of the collective 1^+ state with a background of two- and four-quasiparticle excitations mediated by a constant coupling matrix element [211].

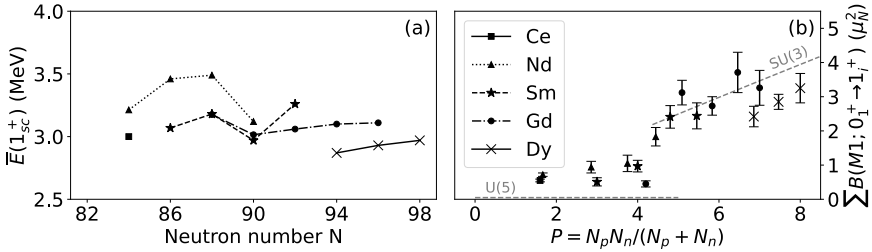

Figure 2.6.: Evolution of the scissors mode's mean excitation energy [panel (a)] and summed $M1$ excitation strength [panel (b)]. While no effect of the QPT at $N = 90$ is observed for the former, the experimental $M1$ strengths exhibit transitional behavior illustrating the scissors mode's origin in quadrupole collectivity. Data are taken from Refs. [19, 150].

and carries the summed $M1$ excitation strength of all individual states i. For the cerium to dysprosium isotopic chains these surrogate quantities are depicted in panels (a) and (b) of Fig. 2.6, respectively. Contrary to the excitation energy of the 2^+_1 state or the $R_{4/2}$ ratio [cf. panel (a) of Fig. 2.3], the mean energy of the scissors mode exhibits no discernible transitional behavior. Besides an inverse mass dependence of $A^{-1/3}$ [141, 148, 150, 159], similar to the giant dipole resonance [11, 213], a linear dependence on the nuclear deformation parameter δ was initially conceived [141, 159]. With the availability of more data over a larger range of deformation parameters this assumption was weakened considerably [148] until it was eventually discarded [150]. In contrast, the summed $M1$ strength shows a clear signature of transitional behavior[57] due to its quadratic dependence on δ [162, 164]. Thus, the mean excitation energy of the scissors mode is not a suitable indicator for a QPT, but the summed excitation

[57] Compared to the $B(E2; 2^+_1 \to 0^+_1)$ evolution [cf. panel (b) of Fig. 2.3], the data on the $M1$ excitation strength shows considerable fluctuations. The majority of the experiments were performed at bremsstrahlung facilities and lack parity assignments. Instead, scissors-mode nature was concluded from rather broad criteria [161]. Due to the high fragmentation and the common energy range selected a priori, a fair amount of the total $M1$ strength might have remained undetected or excluded, respectively. In turn, two-quasiparticle and low-lying spin-flip $M1$ strength may have been incorrectly taken into account. In principle, the parity quantum number as well as the amount of orbital $M1$ strength needs to be extracted for each fragment; e.g. from comparison to proton-scattering experiments [214].

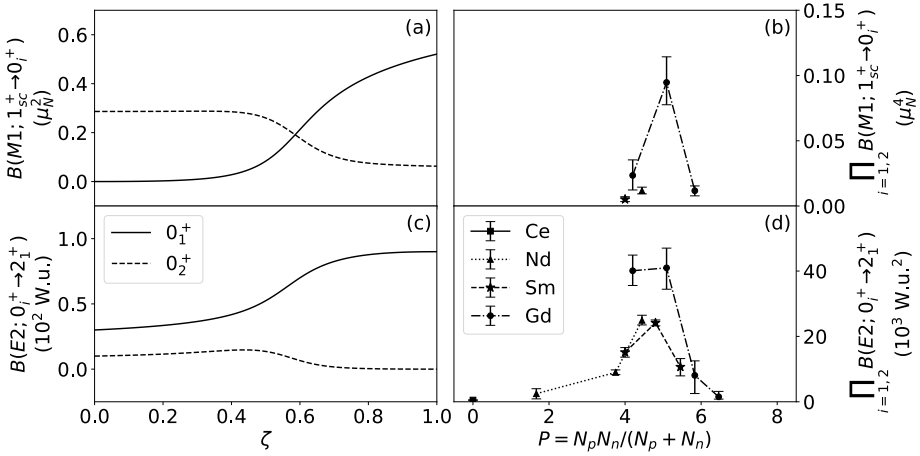

Figure 2.7.: Evolution of $M1$ transition strengths between the scissors mode and the $0^+_{1,2}$ states [panel (a)] and $E2$ transitions strengths connecting the $0^+_{1,2}$ and 2^+_1 states [panel (c)] in the IBM-2 and their products from experiment [panels (b) and (d)]. By virtue of Eq. (2.21) their individual products are related to each other. Indeed, the experimental results, which are illustrated in panels (b) and (d), both peak at the transitional region. Data taken from Refs. [19, 79, 92, 177, 179, 181–185, 206].

strength is. In this context, the different nature of the considered observables has to be emphasized. While the excitation energy of the proxy state is a mean value and, thus, susceptible to outliers, the summed $M1$ strength is a rather robust observable.

At the latest with the advent of monochromatic photon beams or in combination with coincidence measurements, decay properties of single excited states came into focus. For instance, the transition of the scissors mode to the 0^+_2 state was introduced as a measure for shape coexistence [215] and further developed into a sensitive indicator for a QPT [19, 216]. Panel (a) of Fig. 2.7 sketches the evolution of the $M1$ transition strengths between the scissors mode and the $0^+_{1,2}$ states in the IBM-2. The calculations

employ the Hamiltonian [217]

$$\boldsymbol{H} = (1-\zeta)(\boldsymbol{n}_{d_\pi} + \boldsymbol{n}_{d_\nu}) - \frac{\zeta}{4N}(\boldsymbol{Q}^\chi_\pi + \boldsymbol{Q}^\chi_\nu)\cdot(\boldsymbol{Q}^\chi_\pi + \boldsymbol{Q}^\chi_\nu) + \boldsymbol{M}(\xi_1, \xi_2, \xi_3)$$

with $N_\pi = N_\nu = 3$, $\chi = -\sqrt{7}/2$, $\xi_1 = \xi_2 = \xi_3 = 1\,\text{MeV}$, $(g_\pi - g_\nu) = 1\,\mu_N$, and $e_\pi = e_\nu = 1\,\text{W.u.}$ The transition strengths $B(M1; 1^+_{\text{sc}} \to 0^+_1)$ and $B(M1; 1^+_{\text{sc}} \to 0^+_2)$ exhibit an opposite behavior with ζ.[58] While the former qualitatively mirrors the evolution of the experimental data [cf. panel (b) of Fig. 2.6], the latter dominates at small deformation [cf. Eq. (2.19)]. A similar trend is found for the $E2$ transitions connecting the $0^+_{1,2}$ and 2^+_1 states, which are depicted in panel (c) of Fig. 2.7. In an approach, which combines a linear energy weighted $M1$ sum rule [218, 219] with the mixed-symmetry version of the Q-phonon scheme [220–222], the product of the above $M1$ transition strengths is linked to the product of the $E2$ transition probabilities[59] through the relation [19]

$$\frac{B(M1; 0^+_1 \to 1^+_{\text{sc}})B(M1; 0^+_2 \to 1^+_{\text{sc}})}{B(E2; 0^+_1 \to 2^+_1)B(E2; 0^+_2 \to 2^+_1)} = \left(\frac{10.6}{Z^2}\right)^2 \left[1 - \frac{E(0^+_2)}{2E(1^+_{\text{sc}})}\right]^{-2} \tag{2.21}$$

assuming that all transition strengths are given in single-particle units. The left-hand side's enumerator and denominator are shown in panels (b) and (d) of Fig. 2.7, respectively. Both exhibit pronounced maxima around $P \approx 5$ (cf. Section 2.5.1) and, thus, qualify as additional signatures of a QPT between spherical and axially-symmetric deformed phases. While the evolution of the $E2$ part is pinpointed by experimental data, information on only one isotopic chain is available for the $M1$ component. Further precision experiments on weak decay channels of the scissors mode are needed for the neodymium and samarium nuclei around $N = 90$.

An even more elusive signature arises from the $E2$ properties of mixed-symmetry states. The primary origin of low-lying $\Delta F = 1$ quadrupole strength is the one-phonon 2^+_{ms} state of vibrational nuclei [15]. Across the U(5)-SU(3) QPT it is expected to evolve into the 2^+_{sc} member of the $K = 1$ scissors-mode band of deformed nuclei (cf. Fig. 1.1). This is accompanied by an enhancement of the state's excitation energy and a reduction

[58] Naturally, the relative magnitudes of the parameters ξ_i, $i \in \{1, 2, 3\}$, significantly influence the decay behavior of mixed-symmetry states. For reasonable choices, however, a behavior similar to the one depicted in panel (a) of Fig. 2.7 is encountered.

[59] A detailed derivation is given in App. A.1. of Ref. [223]. It must be taken into account that a square is missing in Eq. (A.7) ibidem.

of its $E2$ excitation probability from the ground state. Likewise, the $E2$ transition strength between the scissors mode and the 2_1^+ state decreases.[60] This evolution either originates from or is enhanced by the predicted [224] assimilation of the proton and neutron quadrupole boson charges with incipient deformation, which in turn is traced back to the increasing significance of g-boson renormalization effects in deformed nuclei [225, 226]. However, in the assumed scenario, the necessary experimental ingredients, i.e. at least one F-vector $E2$ transition strength, are available to determine local values of the boson charges e_π and e_ν.[61] This procedure explicitly does not require any a priori assumptions about the evolution of the charges. Hitherto, local values have only been determined for ^{156}Gd [24] in the SU(3) dynamical symmetry and for ^{152}Sm [230] using an F-spin invariant Hamiltonian in the IBM-2. Panel (a) of Fig. 2.8 compares these results to predictions for the neodymium and samarium isotopic chains obtained from g-boson renormalization [226] and introduction of a phenomenological mass dependence [224], respectively. Since the $B(E2; 2_1^+ \to 0_1^+)$ systematics show a contrary behavior [cf. panel (b) of Fig 2.3] to the experimentally available $\Delta F = 1$ $E2$ transition strengths, i.e. $B(E2; 2_{\mathrm{ms}}^+ \to 2_1^+)$ and $B(E2; 1_{\mathrm{sc}}^+ \to 2_1^+)$, their products might constitute novel signatures for the QPT in the fashion of the $M1$ characteristic depicted in Fig. 2.7, panels (a) and (b).

[60] In the Q-phonon scheme the $2_{\mathrm{ms}}^+ \to 0_1^+$ and $1_{\mathrm{sc}}^+ \to 2_1^+$ transitions are equivalent since they both involve the destruction of a mixed-symmetric quadrupole phonon. In the U(5) dynamical symmetry, both share the same analytic expression for the $E2$ strength [59].

[61] For the sake of simplicity, quadrupole boson charges were commonly chosen equal, which is sufficient for the description of $E2$ transitions between states with maximum F-spin. Selecting nuclei for which a common dynamical symmetry is realized, e_π and e_ν were also determined from experimental values for the $B(E2; 2_1^+ \to 0_1^+)$ transition strength [59, 227, 228]. This approach presupposes constancy of the charges for the considered isotopes. Application to the $N = 84$ nuclei ^{140}Ba, ^{142}Ce, and ^{144}Nd [227] or ^{142,150}Nd [226] yielded $e_\nu > e_\pi$ in contrast to expectations from microscopic models [26, 229]. This motivated the introduction of mass-dependent charges [226].

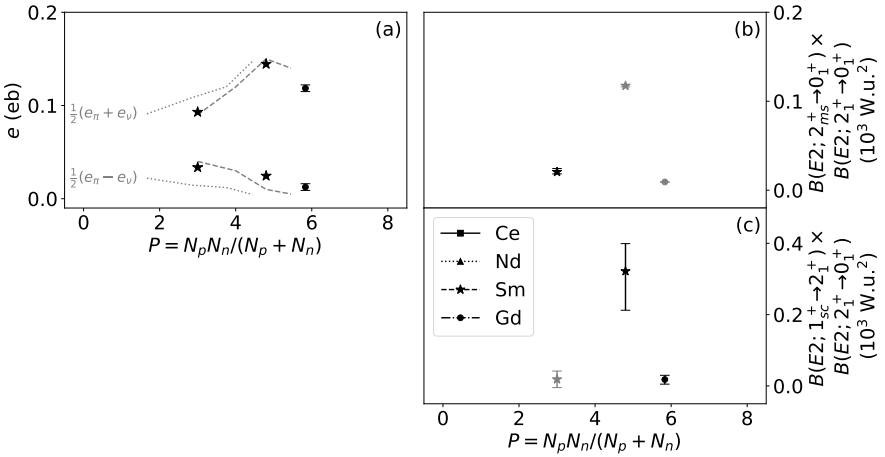

Figure 2.8.: Evolution of $E2$ quantities across the $N = 90$ QPT. Panel (a) depicts scalar and vector quadrupole boson charges for ^{148}Sm [20], ^{152}Sm [230] and ^{156}Gd [24][62]along with predictions for the neodymium [226] and samarium [224] isotopic chains. Panels (b) and (c) show (semi-) experimental values for products of $\Delta F = 0$ and $\Delta F = 1$ $E2$ transition strengths. Predictions for the latter from the IBM-2 calculations, which employ the charges from panel (a), are identified by gray markers. Similar to the $M1$ signatures from panel (b) of Fig. 2.7, a maximum appears to mark the QPT.

[62]Additional data on the $N = 84$ isotones ^{140}Ba [227], ^{142}Ce [231], and ^{144}Nd [232] is not considered for two main reasons. First, these nuclei are characterized by $R_{4/2} < 2.0$ and, thus, are not within reach of the standard IBM. Furthermore, the 2^+_{ms} state of the latter two nuclei is fragmented into two components with comparable $M1$ and $E2$ transition strengths. This is rooted in mixing with a fully-symmetric 2^+ state due to lacking shell stabilization at the proton $g_{7/2}$ subshell closure ($Z = 58$) [233]. While it is restored for the $N = 80$ isotone ^{140}Nd [234], a strong influence still appears to be present for ^{144}Nd. This assumption might be further supported by the observation of anomalous $E2$ transition strengths in the ground-state band of ^{144}Nd [235, 236].

3. Experiments

All experiments discussed in this work were performed at the High-Intensity γ-ray Source (HIγS) of the Triangle Universities Nuclear Laboratory at Duke University, NC, USA using the nuclear resonance fluorescence (NRF) method. In this Chapter, the NRF technique is introduced alongside a discussion of accessible observables. Furthermore, the HIγS facility is presented and the experimental setups for the individual experiments are described. The Chapter closes with an overview of specific experimental details.

3.1. Nuclear resonance fluorescence

The toolbox of nuclear structure physics provides a selection of experimental techniques covering a wide range of excitation energies and transferred angular momenta. For the investigation of scissors-mode states the method must meet certain conditions; mainly it must use a probe which enables a selective excitation of magnetic dipole strength well below the particle-separation threshold and the experimental setup must be sensitive to γ radiation emitted in the decay of excited nuclear states. The technique of nuclear resonance fluorescence in combination with an array of γ-ray detectors fulfills both requirements in an ideal way. The present Section is intended to give a compressed introduction, which is primarily based upon the review articles [147, 237]. Additional details on the the technique itself are given in Ref. [238].

Nuclear resonance fluorescence represents the interaction of incident photons with bound nuclear states. It comprises the excitation of a nuclear level by resonant absorption of a real photon and the subsequent emission of at least one photon [147]. The resonance cross section for this process is of Breit-Wigner shape [239] and experiences

a Doppler broadening due to the thermal motion of nuclei. The latter effect broadens the primal Breit-Wigner cross section but does not change its integral value. For the absorption from an initial state $i \equiv 0$ into an excited state x and the subsequent decay to a state f by emission of a photon, the energy-integrated cross section of this process is given by

$$I_{0\to x\to f} = \underbrace{\pi^2 \left(\frac{\hbar c}{E_x}\right)^2 \frac{2J_x+1}{2J_0+1} \Gamma_{0\to x}}_{I_{0\to x}} \frac{\Gamma_{x\to f}}{\Gamma_x}. \tag{3.1}$$

Here, J_0 and J_x denote the angular momentum quantum numbers of states 0 and x, respectively. The latter's excitation energy is given by E_x. Finally, Γ_x denotes the total transition width of state x, which is defined as as the sum of partial transition widths for all energetically allowed decay channels $x \to f$ and all possible combinations $\sigma\lambda$, i.e.[63]

$$\Gamma_x = \sum_f \Gamma_{x\to f} = \sum_f \sum_{\sigma\lambda} \Gamma_{x\to f,\sigma\lambda}.$$

The potential multipole orders λ and radiation characters $\sigma \in \{E, M\}$ are obtained from the selection rules [Eqs. (2.12) and (2.15) in Chapter XIII.2.B of [240]]

$$\begin{aligned} &|J_x - J_f| \le \lambda \le J_f + J_x \quad \text{and} \\ &\pi_x \pi_f = \begin{cases} (-1)^\lambda & \Leftrightarrow \quad \sigma = E \\ (-1)^{\lambda+1} & \Leftrightarrow \quad \sigma = M. \end{cases} \end{aligned} \tag{3.2}$$

The first selection rule, which is a consequence of the coupling rules for angular momenta, states that a transition between two arbitrary states x and f with $J_x \neq 0$ and $J_f \neq 0$ might be characterized by a combination of various multipolarities. The relative size of the multipole orders $\sigma'(\lambda+1)$ and $\sigma\lambda$ with $\sigma' \neq \sigma$ is quantified by the multipole-mixing ratio $\delta_{x\to f}$. Using the phase convention of Krane, Steffen, and Wheeler [241], it is related to the respective transition matrix elements in the style of

[63] In the context of the present work, the total transition width Γ_x contains only contributions from electromagnetic decay channels. This is inconsequential since the chosen beam energies (cf. Sections 3.3.1 and 3.3.2) are well below the particle separation thresholds of the studied nuclei [184, 187, 188] and internal conversion is negligible even for the lowest energy transitions [Chapter XIII.5.A of [240]].

Bohr and Mottelson [Eqs. (3C-8) of [28]] by the relation[64]

$$\delta_{x\to f} = \frac{\sqrt{\lambda(\lambda+2)}}{(\lambda+1)(2\lambda+3)} \left(\frac{E_x - E_f}{\hbar c}\right) \frac{\langle J_f \| \boldsymbol{T}(\sigma'(\lambda+1)) \| J_x \rangle}{\langle J_f \| \boldsymbol{T}(\sigma\lambda) \| J_x \rangle}. \tag{3.3}$$

From the reduced matrix elements[65] of Eq. (3.3) the reduced transition probability $B(\sigma\lambda; J_x \to J_f)$ and the partial transition width $\Gamma_{x\to f,\sigma\lambda}$ can be obtained via

$$\begin{aligned} B(\sigma\lambda; J_x \to J_f) &= \frac{1}{2J_x+1} |\langle J_f \| \boldsymbol{T}(\sigma\lambda) \| J_x \rangle|^2 \\ &= \Gamma_{x\to f,\sigma\lambda} \frac{1}{8\pi} \frac{\lambda[(2\lambda+1)!!]^2}{\lambda+1} \left(\frac{E_x - E_f}{\hbar c}\right)^{-(2\lambda+1)}. \end{aligned} \tag{3.4}$$

A combination of Eqs. (3.3) and (3.4) connects the squared multipole-mixing ratio $\delta^2_{x\to f} = \Gamma_{x\to f,\sigma\lambda} / \Gamma_{x\to f,\sigma'(\lambda+1)}$ with the ratio of partial transition widths. The magnitude of the multipole-mixing ratio affects the angular distribution of the photons emitted in the transition between states x and f. In general terms, the angular distribution function $W_{0\to x\to f}(\vartheta, \varphi, \delta_{x\to f})$ comprises contributions from the excitation of state x by an unpolarized and a linearly polarized beam, i.e. [147]

$$\begin{aligned} &W_{0\to x\to f}(\vartheta, \varphi, \delta_{x\to f}) \\ &\quad = W^{\text{unpolarized}}_{0\to x\to f}(\vartheta, \delta_{x\to f}) \\ &\qquad + (\pm)_{\lambda'_{0\to x}} W^{\text{polarized}}_{0\to x\to f}(\vartheta, \varphi, \delta_{x\to f}) \\ &\quad = \sum_{\nu\in\{0,2,4\}} A_\nu(X_{0\to x}) A_\nu(X_{x\to f}) P_\nu(\cos\vartheta) \\ &\qquad + (\pm)_{\lambda'_{0\to x}} \sum_{\nu\in\{2,4\}} A'_\nu(X_{0\to x}) A'_\nu(X_{x\to f}) P^{(2)}_\nu(\cos\vartheta)\cos(2\varphi). \end{aligned} \tag{3.5}$$

Here, P_ν denotes the Legendre polynomial of degree ν and $P^{(2)}_\nu$ is the unnormalized associated Legendre polynomial of second order and degree ν. The expansion coefficients A_ν and A'_ν are functions of the multipolarities of the considered transition

[64] For the $E2/M1$ ($\lambda = 1$) matrix element, the first factor evaluates to $\sqrt{3}/10$.

[65] The reduced matrix element contains the complete physical significance of the full matrix element $\langle J_f M_f | \boldsymbol{T}(\sigma\lambda) | J_i M_i \rangle$. This means that the dependence on the magnetic quantum numbers M_i and M_f is purely geometrical and can be given by a Clebsch-Gordan coefficient. It is a consequence of the Wigner-Eckhart theorem [Eq. (14.15) of [42]], which is fundamental for algebras of general irreducible tensor operators.

and the angular momenta of the states connected by it; these dependencies are summarized in $X_{0\to x}$ and $X_{x\to f}$ for exciting and deexciting transitions, respectively. The explicit definitions of A_ν and A'_ν are given in Ref. [241]. In principle, the sums in Eq. (3.5) extend to all even values ν for which P_ν and $P_\nu^{(2)}$ do not vanish. However, since dipole and quadrupole excitations dominate the NRF process [147], the considered multipolarities ν are restricted to these cases.

The term $W_{0\to x\to f}^{\text{unpolarized}}(\vartheta, \delta_{x\to f})$ in Eq. (3.5) denotes the angular distribution for the excitation by unpolarized photons such as on-axis bremsstrahlung. It is only dependent on the polar angle ϑ with respect to the incident photon beam. Since the scissors mode manifests itself as magnetic dipole strength (cf. Section 2.4), parity information is needed for its identification. It can be inferred from the polarization of the emitted photons by Compton polarimetry [242]. Since the polarization sensitivity is typically limited to about 10% at 3 MeV [237, 243] the usage of linearly polarized photons in the entrance channel is desirable. This process, which is represented by $W_{0\to x\to f}^{\text{polarized}}(\vartheta, \varphi, \delta_{x\to f})$ in Eq. (3.5), causes an anisotropic azimuthal distribution of the emitted photons. The relative sign of the polarized contribution is indicated by $(\pm)_{\lambda'_{0\to x}}$ which is positive (negative) for electric (magnetic) character of the higher multipolarity of the transition $x \to f$. While the energy-dependent polarization $P_\gamma(E_\gamma)$ is small for off-axis bremsstrahlung, it is close to unity for linearly polarized γ-ray beams provided by HIγS [244].

3.2. The High-Intensity γ-ray Source

The key features of HIγS are outlined in Ref. [245], which serves as a guideline for this Section. The facility is centered around an electron storage ring, which is supplied with ultra-relativistic[66] bunched electrons by a normal-conducting linear accelerator coupled to a booster synchrotron. Through Compton backscattering of free-electron laser-generated photons, quasi-monochromatic and almost 100% linearly polarized [244] photon beams are provided. In this process, the energy of the laser photons, which is typically in the range of a few eV, is increased to the MeV regime; this corresponds to a Lorentz boost factor of at least 10^6. This enables the γ-ray beam to leave the free-electron laser cavity and propagate towards the experimental areas.

[66] The storage ring is designed for electron energies ranging from 0.24 to 1.2 GeV [245].

In a distance of roughly 57 m from the collision point a collimation system is located. It allows a reduction of the beam's cross section and, thus, its energy spread.[67] The selection of collimators with a diameter of 0.75 in[68] results in photon beams with approximately 3% energy resolution and a photon rate between 10^7 and $10^8\,\mathrm{s}^{-1}$. After collimation, the beam traverses the experimental area, which is located in the so-called upstream target room, in an evacuated pipe. The individual targets are mounted inside the pipe in the center of the γ^3 detector setup [247]. The different configurations of the detectors are described in Sections 3.3.1 and 3.3.2. For beam diagnostics, a high-purity germanium (HPGe) detector can be swiveled into the beam axis. This allows the profile of the attenuated incident γ-ray beam to be recorded. In addition, a charge-coupled device (CCD) based imaging system is available for alignment of the collimator and the experimental apparatus [Sec. 5 of [248]].

3.3. Experimental details

The experiments discussed in this work utilized the γ^3 detector array [247], which has been installed at HIγS for the first time prior to the 2012 experimental campaign. It picks up the idea of a parity-sensitive arrangement of HPGe detectors in conjunction with an array of cerium-doped lanthanum bromide ($LaBr_3$:Ce) scintillators for $\gamma\gamma$-coincidence measurements. In standard configuration, it features four HPGe detectors and four 3 in × 3 in scintillators, whose positions are fully interchangeable. In the following, the position of each detector is characterized by a tuple (ϑ, φ) composed of the polar angle ϑ and the azimuthal angle φ with respect to the direction of the incident γ-ray beam and the beam's horizontal polarization plane, respectively. In contrast to the previous NRF setup at HIγS, which represented a simple polarimetry geometry for maximum sensitivity to the parity of dipole-excited states [249, 250], the inclusion of detectors at backward polar angles, i.e. $\vartheta > 90°$, enables a distinction between dipole- and quadrupole-excited states (cf. Sections 3.1 and 4.3.1).

The data acquisition (DAQ) system of the γ^3 setup is implemented twofold: analog singles spectra were recorded with the Canberra GENIE 2000 system, while simultaneously the Multi Branch System (MBS) [251] provided an event-based recording of

[67] The connection between the beam diameter and the energy spread is illustrated by Eq. (1) of Ref. [246].
[68] In metric units, this corresponds to 19.05 mm.

data. The latter enables the analysis of $\gamma\gamma$-coincidences. A comprehensive discussion of the used electronics and software is given in Refs. [247, 252].

3.3.1. Experiment on ^{154}Gd

Historically, ^{154}Gd has been the first transitional nucleus with experimental information on scissors-mode states following the identification [253] of strong $M1$ excitations in inelastic electron scattering. These states have also been investigated with bremsstrahlung-induced photon-scattering experiments augmented by the analysis of $\gamma\gamma$-coincidences after electron capture [19, 216]. This approach yielded absolute transition strengths and experimental decay intensity ratios. The present experiment is focused on the strongly excited 1^+ scissors-mode state at 2934.2(6) keV. It aims for an extraction of the $M1/E2$ multipole-mixing ratio [cf. Eq. (3.3)] of the γ-ray transition between the scissors mode and the 2^+ state of the ground-state rotational band. Consequently, the incident beam's energy was tuned to 2948(95) keV for the entirety of the experiment. The composite target was mounted in the center of the γ^3 setup consisting of four HPGe detectors at positions (ϑ, φ) of $(135°, 315°)$, $(90°, 90°)$, $(135°, 45°)$, and $(90°, 180°)$ alongside four large-volume $LaBr_3$:Ce scintillators positioned at $(90°, 0°)$, $(90°, 270°)$, $(135°, 225°)$, and $(135°, 135°)$.

Analysis of the CCD-based beam-imaging system [Sec. 5 of [248]] reveals a relative displacement of beam and target axes. In Fig. 3.1, which shows the spatial intensity distribution of the beam, they are marked by a cross and a plus sign, respectively. In addition, it also depicts the proportions of the individual target components. The actual target consisted of 4.978(25) g of gadolinium[69] in the chemical form of a Gd_2O_3 compound. It was enriched to 66.78(20)% in the isotope ^{154}Gd, corresponding to 3.325(20) g. The powdery target material was enclosed in a high-density polyethylene (HDPE, C_2H_4) container[70] with 0.75 in inner diameter. For photon-flux calibration two

[69] An inquiry to Oak Ridge National Lab (ORNL) revealed that 5.0000 g of gadolinium were prepared in form of a pellet with a diameter of 0.75 in. This material has been pressed into a container with an inner diameter of 0.75 in. During this procedure losses might have been occurred. After return to ORNL, the material weighed 4.9550 g after removal from the container. However, material may have remained in the container. In order to account for these imponderables, the mean value of both weights has been adopted along with an appropriate uncertainty.

[70] In the excitation region of the γ-ray beam no contaminant NRF transitions of ^{12}C [254] or ^{13}C [255] are known.

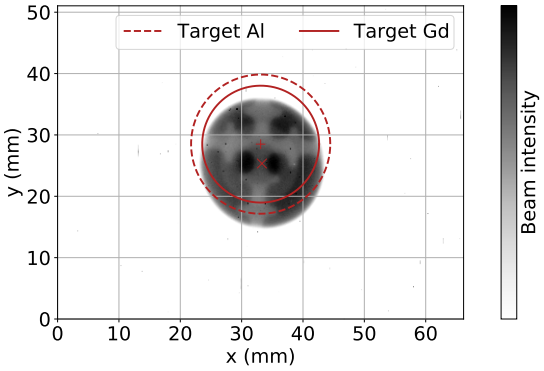

Figure 3.1.: Intensity profile of the incident photon beam during the ^{154}Gd experiment. The image comprises 752 × 580 pixels and has a resolution of 0.088 mm. It shows the superposition of the images of two alignment targets; a crosshair for the γ^3 setup and a circular item for the downstream setup. The former defines the target position which is marked by a red plus sign. Since it does not coincide with the center of the beam distribution, which is indicated by a red cross, the beam does not fully cover the aluminum (dashed red line) and gadolinium (solid red line) targets. Due to the divergence of the beam and scattering effects, the beam image is enlarged by roughly 5%.

0.5 mm thick aluminum sheets were added up- and downstream of the gadolinium. Since they have a larger diameter than the gadolinium pellet,[71] two different target compositions have to be considered during calibration. In the narrow crescent at the lower edge of the target composite (cf. Fig. 3.1), which corresponds to 11.6% of the aluminum target area, the beam traverses solely the two aluminum sheets but not the gadolinium. In contrast, 58.2% feature a gadolinium interlayer with a particle areal density of 0.00680(4) b^{-1}. In total, approximately 69.8% of the aluminum and 82.5% of the gadolinium targets are covered by the beam. Still, the photon-flux calibration

[71] The shape of the aluminum sheets deviates from a perfect circle. Mean radii of 11.1(6) and 11.3(6) mm are estimated from their weights [0.53105(1) and 0.55151(1) g] for the up- and downstream targets, respectively.

using aluminum can only be performed if also the spatial intensity distribution of the beam is known. From simulations, a non-homogeneous distribution is expected, which is characteristically quenched in the present case of linear polarization [Fig. 5 of [256]]. In practice, however, it cannot be inferred from the beam image shown in Fig. 3.1 because the relation between the beam intensity and the pixel value is unknown and saturation effects in the CCD might play a role. Thus, excitation cross sections of previously unknown states are determined relative to the 1^+ state at 2934.2(6) keV whose integrated cross section is known from a previous bremsstrahlung experiment [19].

Additional information on experimental properties, such as the target composition, is collected in Appendix C.1.

3.3.2. Experiments on ^{162,164}Dy

Similar to the case of ^{154}Gd, the objective of the experiments on the well-deformed nuclei ^{162,164}Dy is the investigation of the main scissors-mode fragments. For both isotopes, data on these states already exists from three bremsstrahlung experiments [154, 257, 258] and from spectroscopy after inelastic neutron scattering [259]. In the case of ^{164}Dy, additional experiments have been performed with inelastic electron scattering [144, 260] and polarized photon beams at HIγS [261]. The experiments presented in this work are mainly focused on the extraction of multipole-mixing ratios between strongly excited scissors-mode states and the 2_1^+ state. They exploited the γ^3 setup, which comprised four HPGe detectors at positions (ϑ, φ) of $(90°, 0°)$, $(90°, 90°)$, $(135°, 315°)$, and $(135°, 225°)$. In addition, four $LaBr_3$:Ce scintillators for $\gamma\gamma$-coincidence measurements were mounted at $(90°, 180°)$, $(90°, 270°)$, $(135°, 45°)$, and $(135°, 135°)$.

Since the considered 1^+ states of ^{162}Dy are located at 2900.0(3) and 3061.2(3) keV, the mean energies of the incident γ-ray beam were tuned to 2905(102) and 3069(119) keV. The ^{162}Dy target contained 4.6921(1) g of the compound Dy_2O_3 with an enrichment of 96.17(1)% in ^{162}Dy.[72] The material was encased in a plastic container,[73] which gave rise to NRF transitions from ^{13}C in the spectra.

Concerning the isotope ^{164}Dy, prominent 1^+_i states ($i = 1-3$) associated with the scissors mode are located at 3111.2(3), 3159.1(3), and 3173.6(3) keV. In order to excite them simultaneously, the 0.75 in collimator, which was used in the preceding experiment on ^{162}Dy, was retained and the beam energy was set to 3185(102) keV. Exploiting the coincidence capabilities of the γ^3 setup, additional aspects of the intriguing structure of ^{164}Dy can be probed. This includes a conjectured sizeable coupling of the scissors mode to the γ-vibrational band along with the existence of additional nuclear states at 3100 keV [259, 261]. Since the ground-state decays of potential states at 3100 keV are masked by the $1^+_3 \rightarrow 2^+_1$ transition at virtually the same energy, an additional beam setting was introduced. In order to prevent an excitation of the 1^+_3 state, it features a beam energy of 3076(98) keV.[74] In both measurements, the γ-ray beams were scattered from a target composed of 0.770(1) g Dy_2O_3 and 1.1(1) g metallic dysprosium with enrichments in ^{164}Dy of approximately 98(1) and 95.6(1)%, respectively.[75] Since the exact material composition of the target container was unknown, measurements with an identical, empty container were performed to ensure that transitions of ^{164}Dy do not coincide with contaminants.

Additional information on experimental properties, such as the target composition, is collected in Appendices C.2 and C.3.

[72] Uncertainties estimated from the last digit given in Ref. [262].

[73] The material and exact dimensions of the cylindrical container are unknown. Solely the rough dimensions, a diameter of 20 mm and a height of 8 mm, are reported [262]. It is assumed that these values correspond to outer dimensions and, thus, the inner diameter might be 0.75 in similar to the container of the ^{154}Gd target (cf. Section 3.3.1).

[74] In Ref. [262] it is noted that the 0.75 in collimator was replaced by one with a diameter of 0.50 in. Since the beam's energy spread does not change between both measurements, the assumption is that both featured the same collimator size. The beam's energy spread for the ^{162}Dy experiment, on the other hand, is systematically larger. Moreover, it is comparable to the ^{154}Gd experiment (cf. Section 3.3.1), which featured a collimator with a diameter of 0.75 in.

[75] See footnote [72].

4. Analysis

The data, collected in the experiments described in Sections 3.3.1 and 3.3.2, are subject to the processing and analysis steps presented in the following. This includes a series of calibrations and the extraction of physically significant quantities. In the case of the ^{154}Gd experiment, the analysis is based upon data recorded by the analogue acquisition system (cf. Section 3.3). The event-based DAQ was used for the evaluation of the measurements on ^{162,164}Dy due to its $\gamma\gamma$-coincidence capabilities.

4.1. General remarks

The general methodology of the analysis follows the principles outlined in Ref. [263]. Instead of the standard first-order Taylor series expansion, it employs a Monte-Carlo method for the propagation of uncertainties. In this sense, a functional relationship f between vectorial input quantities $\boldsymbol{X}$ and output quantities $\boldsymbol{Y}$, i.e. $\boldsymbol{Y} = f(\boldsymbol{X})$, is considered. Each component X_i of $\boldsymbol{X}$, $i \in \{1, \ldots, |\boldsymbol{X}|\}$, can be distributed according to an individual probability density function (PDF) $g_{X_i}(\xi_i)$. Here, the ξ_i are variables describing the possible values of the quantities X_i. The PDFs $g_{X_i}(\xi_i)$ have to be selected with the available knowledge.[76] The PDF of $\boldsymbol{Y}$ is obtained by propagation of the PDFs of the X_i through the model f, which is implemented in form of the Monte-Carlo method [264]. It approximates the PDF $g_{\boldsymbol{Y}}$ by repeated evaluation of the model f using input vectors randomly sampled from $g_{\boldsymbol{X}}$. The obtained empirical PDF converges to $g_{\boldsymbol{Y}}$ as the sample number approaches infinity.

[76] It has to be noted that the PDFs can only be selected individually if the X_i are independent. Otherwise, the joint PDF $g_{\boldsymbol{X}}(\boldsymbol{\xi})$ has to be considered.

The PDFs of the output quantities Y_i, $i \in \{1, \ldots, |\boldsymbol{Y}|\}$, are then characterized by their mode and shortest coverage interval; i.e. in the form

$$\text{mode}(Y_i)^{+[\text{sc}_+(Y_i)-\text{mode}(Y_i)]}_{-[\text{mode}(Y_i)-\text{sc}_-(Y_i)]}. \tag{4.1}$$

The mode, which denotes the most probable value of Y_i, is determined by a Gaussian kernel-density estimator. In order to mimic the standard deviation of a normal distribution, the shortest coverage interval contains by construction 68.27% of the sample values. In Eq. (4.1) the upper and lower boundaries of the shortest coverage interval are denoted sc_+ and sc_-, respectively.

4.2. Data processing

Prior to the data analysis with respect to physical questions, the raw pulse-height spectra have to be energy and efficiency calibrated. The estimation of excitation strengths is facilitated by a calibration of the incident photon-flux distribution.

4.2.1. Energy calibration

The analysis of the experimental data necessitates energy information on observed structures. Thus, an energy calibration of the recorded pulse-height spectra is required. In the present experiments, the energy region between 1000 and 3200 keV is of special interest. Coincidentally, the calibration source ^{56}Co emits photons with energies that cover this range [265]. Since the source runs are mainly performed before and after the experiment, the energy calibration is prone to time-dependent drifts of the electronic equipment. In order to prevent this, the spectra of all runs are aligned using photons from ambient background at 511 (electron-positron annihilation [266]), 1436 (^{138}La decay [267]), 1461 (^{40}K decay [268]), 1765 (^{214}Bi decay [269]), and 2615 keV (^{208}Bi decay [270]).

In general, the calibration, which maps the channel c_i of an analog-to-digital converter (ADC) onto its associated energy $E(c_i)$, is expressed in terms of a polynomial $E(c_i) = \sum_{n=0}^{N} a_i c_i^n$. For HPGe detectors, a linear relation with small quadratic corrections, i.e. $N = 2$ with a_2 small, is recommended [Sec. 7.4 of [271]]. However,

the used ADCs exhibited a high degree of linearity in the decisive range [Sec. 9.4 of [271]]. Thus, a linear relation ($N = 1$) is sufficient. For the $LaBr_3$:Ce scintillators, $N = 3$ is needed to account for nonlinear effects in the read-out electronics [252]. The investigated nuclear states are found below 3200 keV, while data points for calibration are available up to 3451 keV [265]. Hence, no negative consequences of extrapolation have to be considered.

4.2.2. Efficiency calibration

In spectroscopic experiments, only the number of events counted in a detector is directly accessible. However, this quantity differs from the number of, in the present case, emitted γ-rays due to the intrinsic efficiency of the used detector, shielding or plain geometric effects. The energy-dependent proportionality factor between both is the efficiency $\epsilon(E_\gamma)$.

Since the energy range of the discussed experiments can be covered by γ-rays emitted from radioactive sources (cf. Section 4.2.1), a dedicated simulation of the setup's photopeak efficiency is not mandatory. Instead, the efficiency is determined experimentally for a set of energies E_γ using the standard calibration sources ^{56}Co and ^{152}Eu. In the case of the ^{154}Gd experiment, additional measurements with ^{22}Na, ^{60}Co, and ^{137}Cs were performed. For all isotopes, energies E_γ and intensities $I(E_\gamma)$ of the emitted γ-rays are well-known [183, 265, 272–274]. The sources, which are point-like in good approximation compared to the dimensions of the γ^3 setup, were placed in the actual target position. From the measured number of events $A(E_\gamma)$, the absolute efficiency at an energy E_γ is determined by

$$\epsilon_{\mathrm{abs}}(E_\gamma) = \frac{A(E_\gamma)}{I(E_\gamma)\dot{N}(t)t_{\mathrm{live}}},$$

where $\dot{N}(t)$ and $t_{\mathrm{live}} = t_{\mathrm{real}} - t_{\mathrm{dead}}$ are the source activity and the live time of the considered detector, respectively.[77] Choosing from a variety of phenomenological

[77] The actual time, during which the electronics accepts signals, is called the live time t_{live}. It is the difference of the wall time t_{real}, i.e. the time between start and stop of the measurement, and the dead time t_{dead}. The latter denotes the time needed for signal processing during which the electronics do not accept new signals.

models, the energy dependence of the efficiencies is interpolated by the function

$$\epsilon_{\text{abs}}(E) = \left(a_1 E + \frac{a_2}{E}\right) \exp\left[a_3 E + \frac{a_4}{E}\right],$$

which is adapted to the experimentally determined efficiencies via the parameters a_i, $i \in \{1, \ldots, 4\}$.

4.2.3. Photon-flux calibration

The number of photons per energy which is available for a reaction is quantified by the photon flux $N_\gamma(E)$. However, neither the energy dependence of the distribution nor its integral value are known a priori.[78] They can be extracted from spectra of the detector placed in the attenuated γ-ray beam (cf. Section 3.2).

Neglecting background contributions, the recorded spectra can generally be described as a convolution of the original spectrum of particles impinging on the detector and a nontrivial detector response. The latter originates from the physical processes causing an energy deposition inside the detector volume. From large-scale simulations of the beam's interaction with the detector in a realistic experimental environment, a deconvolution of the spectra, i.e. a removal of the detector response, can be performed [277]. This procedure yields the reconstructed initial photon-flux distribution. However, for beam energies around 3 MeV, the characteristics of the original distribution are retained[79] despite the detector response [92]. Thus, in the present case the spectral shape of the incident γ-ray beam can be extracted directly from the measured spectra. For further usage, it is normalized such that the photon flux is separated into a scaling factor N_γ and an energy-dependent shape $n_\gamma(E)$, i.e.

$$N_\gamma(E) = N_\gamma n_\gamma(E).$$

[78] This is a stark contrast to experiments with bremsstrahlung-generated γ-ray beams. For their spectra analytical expressions are known [275]; for instance the thin-target approximation known as the Schiff formula [276].

[79] This means that the majority of the incident photons deposits its complete energy in the detector. Around 3 MeV, Compton scattering dominates the γ-ray interaction with germanium [278]. The maximum mean free path after the first energy deposition, i.e. of the second interaction, is in the range of a few centimeter and, thus, has a large probability to end within the detector crystal once more.

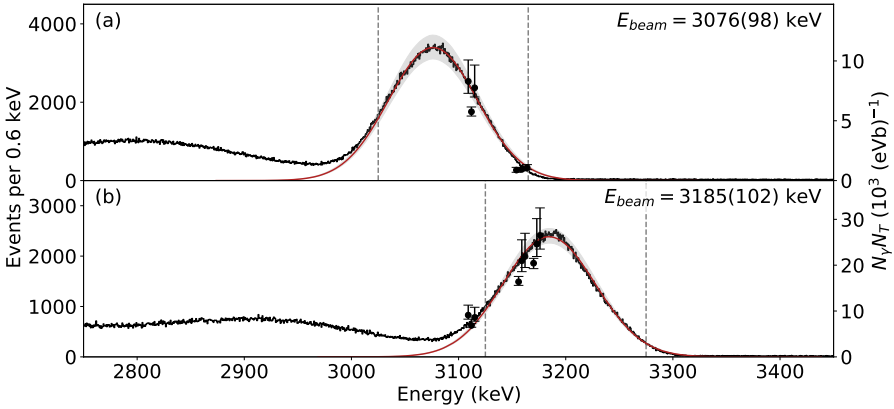

Figure 4.1.: Photon-flux calibration for beam settings $E_{\mathrm{beam}} = 3076(98)\,\mathrm{keV}$ [panel (a)] and $E_{\mathrm{beam}} = 3185(102)\,\mathrm{keV}$ [panel (b)] of the ^{164}Dy experiment. The red line corresponds to the extracted photon-flux distribution along with its gray uncertainty band. Its energy-dependent shape $n_\gamma(E)$ is taken from the range of the spectrum indicated by gray dashed lines. The time-integrated scaling factor $N_\gamma N_T$ relies on known cross sections of the 1^+ states at 3111.2(3), 3159.1(3), and 3173.6(3) keV. It is simultaneously adapted to all sensitive detectors. For better visibility, the data points are slightly displaced in the horizontal.

The second step of the photon-flux calibration concerns the determination of the scaling factor N_γ. In contrast to experiments using bremsstrahlung, a calibration of the total photon flux with well-known resonances of additional calibration targets [147] such as ^{11}B [279] or ^{27}Al [161, 280] is in most cases not possible due to the beam's small energy spread. Still, an absolute normalization can be obtained if the integrated cross section [cf. Eq. (3.1)] for at least one nuclear state in the excitation region is known. In the present case, information from bremsstrahlung experiments is available for the studied nuclei ^{154}Gd [19, 216], ^{162}Dy [154, 257], and ^{164}Dy [154, 257, 261].

Thus, integrated cross sections of excited dipole states in the region of interest are available for determination of N_γ.[80] In practice, the product of the scaling factor N_γ and the number of target nuclei available for an NRF reaction N_T is simultaneously adapted for all sensitive detectors[81] respecting the previously determined shape $n_\gamma(E)$ of the photon-flux distribution. Exemplarily, the results of this process are shown in Fig. 4.1 for the two beam settings of the ^{164}Dy experiment (cf. Section 3.3.2).

4.3. Extracted quantities

The incident photon flux, whose properties are discussed in Section 4.2.3, triggers NRF reactions in the target material.[82] The photons emitted in the decay of excited states are detected by γ-ray detectors which are subject to the calibrations described in Sections 4.2.1 and 4.2.2. From the recorded pulse-height spectra, only two quantities are directly accessible: the energy of the detected photons and their number, which is dependent on the photon flux. If the emitted photons are detected at different positions, additional information on their angular distribution can be obtained. Based on this information and using the methodology introduced in Section 4.1, further quantities are derived. Since the main focus is on the transitions of a state x, which is excited from the ground state, to final states f, i.e. on transitions of type $0 \rightarrow x \rightarrow f$, solely such cascades are discussed in the following.

4.3.1. Quantum numbers and multipole-mixing ratio

The photons emitted in the transition between two nuclear states follow a particular angular distribution. Since it is a function of angular momentum and parity quantum numbers of the involved states and the depopulating transition's multipole-mixing

[80] If knowledge on integrated cross sections is absent for individual beam settings, the γ-ray flux can still be obtained from a relative flux normalization [281–283]. It incorporates additional information on the nonresonant scattering of photons from realistic simulations [284].

[81] The term 'sensitive detectors' denotes all detectors for which the given angular distribution (3.5) does not evaluate to zero in the limit of a point-like geometry. For instance, this exemption applies to the positions $(\vartheta, \varphi) = (90°, 90°)$ and $(90°, 270°)$ for a $0^+ \rightarrow 1^+ \rightarrow 0^+$ cascade.

[82] Absorption of a beam photon is only possible, if a resonance condition is fulfilled. Naturally, NRF reactions can occur also in the surrounding material if primal or scattered photons fulfill this energy condition.

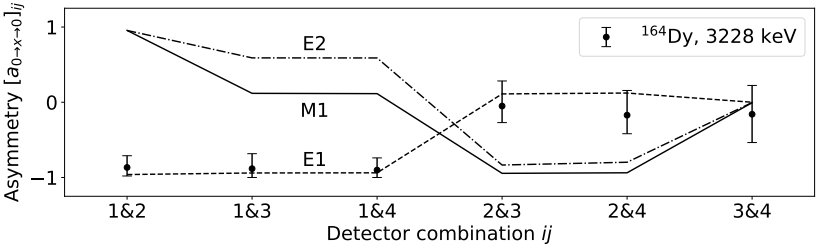

Figure 4.2.: Determination of angular momentum and parity quantum numbers for an excited state of ^{164}Dy at 3228.0(7) keV. From a comparison of experimental asymmetry values [cf. Eq. (4.2)] and analyzing powers [cf. Eq. (4.3)] for $M1$ (solid), $E1$ (dashed), and $E2$ (dash-dotted) character, $J_x^{\pi_x} = 1^-$ is obtained unambiguously.

ratio [cf. Eq. (3.3)], these quantities can be deduced from the photon's angular distribution. The method is a broader application of the concept of asymmetry, which is used for parity determination [249, 250]. The asymmetry $[a_{0\to x\to f}]_{ij}$ of the number of recorded events associated with a transition connecting the states x and f and between two distinct detectors i and j is defined as

$$[a_{0\to x\to f}]_{ij} = \frac{[A_{x\to f}]_i/[\epsilon(E_{\gamma,x\to f})]_i - [A_{x\to f}]_j/[\epsilon(E_{\gamma,x\to f})]_j}{[A_{x\to f}]_i/[\epsilon(E_{\gamma,x\to f})]_i + [A_{x\to f}]_j/[\epsilon(E_{\gamma,x\to f})]_j} \qquad \forall (i,j) : i < j. \tag{4.2}$$

Here, $[A_{x\to f}]_i$ is the number of counts associated with the transition between the states x and f, which is registered in a detector i with detection efficiency $[\epsilon(E_{\gamma,x\to f})]_i$ at the respective γ-ray energy $E_{\gamma,x\to f}$.[83] Respecting the spatial extensions of the target and the finite solid angle of the detectors with respect to photons of energy $E_{\gamma,x\to f}$, the asymmetry must be equal to the analyzing power

$$[\Sigma_{0\to x\to f}]_{ij} = \frac{[W_{0\to x\to f}]_i - [W_{0\to x\to f}]_j}{[W_{0\to x\to f}]_i + [W_{0\to x\to f}]_j} \qquad \forall (i,j) : i < j, \tag{4.3}$$

[83] The efficiency does not necessarily need to be absolute since common factors cancel in the ratio.

if the impinging photon beam is entirely linearly polarized. The latter assumption is in good approximation valid for the photon beams at HIγS [245, 256]. The asymmetry provides a connection of the experimentally observed peak areas to the analyzing power, which, in fact, is dependent on the potentially unknown quantities J_x, π_x or $\delta_{x\to f}$ [249, 250, 285]. In practice, their compatibility with the asymmetry is evaluated in terms of χ^2 values

$$\chi^2 = \sum_{(i,j):i<j} \left(\frac{[a_{0\to x\to f}]_{ij} - [\Sigma_{0\to x\to f}]_{ij}}{[\sigma_{a_{0\to x\to f}}]_{ij}} \right)^2, \tag{4.4}$$

where $[\sigma_{a_{0\to x\to f}}]_{ij}$ is the standard deviation of the asymmetry between detectors i and j. It is assumed that the most probable solution corresponds to minimum χ^2. In this way, the properties of excited states can be extracted. The potential quantum numbers $J_x^{\pi_x}$ of excited states are limited by the low momentum transfer of real photons. Consequently, only dipole and electric quadrupole excitations from the $J_0^{\pi_0} = 0^+$ ground state are considered. The assignment of angular momentum and parity quantum numbers is exemplarily shown in Fig. 4.2 for a state of ^{164}Dy at 3228.0(7) keV. Clearly, only $J_x^{\pi_x} = 1^-$ is consistent with the observed asymmetries.

The multipole-mixing ratio, on the other hand, is a continuous quantity. Exemplarily, its determination process is depicted in Fig. 4.3 for the $E2/M1$ transition between the 1^+ scissors-mode state at 2934.2(6) keV and the 2_1^+ state of ^{154}Gd. For varying values of $\delta_{x\to f}$, the resulting analyzing powers are tested against the experimental asymmetries [cf. panel (a)]. The evolution of the resulting χ^2 values with $\delta_{x\to f}$ is shown in panel (c). It exhibits two distinct minima corresponding to dominant $M1$ character ($\delta_{x\to f}$ close to zero) and a substantial $E2$ contribution ($\delta_{x\to f} \approx -2$).[84] The identification of the most probable scenario relies on two principles; on one hand, the multipole-mixing ratio corresponding to the global minimum in χ^2 values is favored and, on the other hand, it must be sound in the given physical context. The latter criterion is described in more detail in Chapter 5.

[84] In fact, $|\delta_{x\to f}| = 2$ implies an 80% share of the higher multipolarity in the transition.

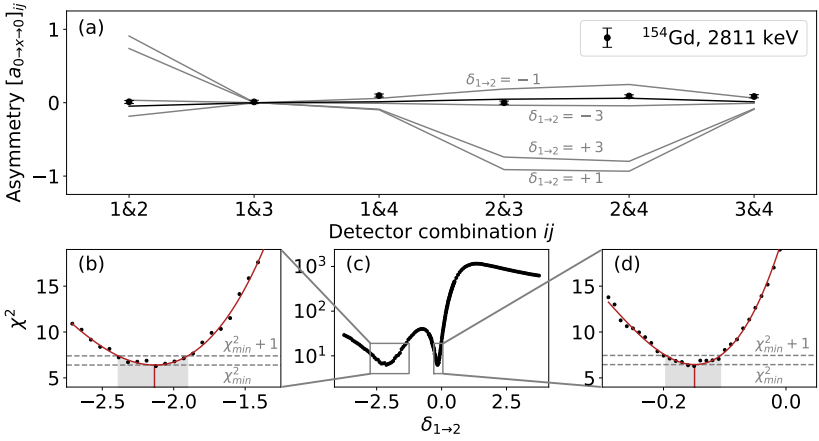

Figure 4.3.: Determination of the multipole-mixing ratio $\delta_{1\to2}$ for the decay of the 1^+ scissors-mode state of ^{154}Gd at 2934.2(6) keV to the 2^+_1 state. The experimental asymmetries alongside exemplary analyzing powers for different values of $\delta_{1\to2}$ are shown in panel (a) while the conformity of both is depicted in panel (c) in terms of χ^2 values. The local minima χ^2_{min} corresponding to dominant $M1$ and $E2$ character are highlighted in panels (b) and (d), respectively. In both cases, the most probable values for the multipole-mixing ratios along with their 1σ confidence intervals are obtained from fits to the data (red line) in the vicinity of χ^2_{min}. Minimum χ^2 and $\chi^2_{\text{min}} + 1$ are indicated by gray dashed lines in panels (b) and (d).

4.3.2. Branching ratio

A key signature of an excited nuclear state x is its electromagnetic decay behavior into lower-lying states. Apart from basic selection rules [cf. Eq. (3.2)], relative decay intensities are highly sensitive to the structure of the involved nuclear states. In general terms, the ratio of transition strengths

$$R_{x\to f/0} = \frac{B(\sigma\lambda; J_x^{\pi_x} \to J_f^{\pi_f})}{B(\sigma\lambda; J_x^{\pi_x} \to J_0^{\pi_0})} \overset{(3.4)}{=} \frac{\Gamma_{x\to f}}{\Gamma_{x\to 0}} \left(\frac{E_{\gamma,x\to 0}}{E_{\gamma,x\to f}}\right)^{2\lambda+1} \tag{4.5}$$

is a measure for the probability that an excited state x decays to a particular lower-lying state f, relative to the $x \to 0$ transition. In nuclear resonance fluorescence experiments, the branching ratio $\Gamma_{x\to f}/\Gamma_{x\to 0}$, which is intimately linked to the ratio of transition strengths [cf. Eq. (4.5)], is accessible via the ratio of integrated cross sections [cf. Eq. (3.1)]

$$\frac{\Gamma_{x\to f}}{\Gamma_{x\to 0}} = \frac{I_{0\to x\to f}}{I_{0\to x\to 0}} = \frac{[A_{0\to x\to f}]_i}{[A_{0\to x\to 0}]_i} \frac{[\epsilon(E_{\gamma,x\to 0})]_i [W_{0\to x\to 0}]_i}{[\epsilon(E_{\gamma,x\to f})]_i [W_{0\to x\to f}]_i} \qquad \forall i. \tag{4.6}$$

Since it is not guaranteed that all depopulating transitions are observed in an experiment, the branching ratios are normalized to the ground-state transition instead of the total transition width $\Gamma_x = \sum_f \Gamma_{x\to f}$.[85] In practice, the branching ratio can be determined for each detector individually. However, it is a characteristic of the transition and should be independent of the detector. In order to reflect this fact, the integrated cross sections from Eq. (4.6) are adapted to the experimental data for all detectors i simultaneously. The branching ratio is then obtained by the ratio of the integrated cross sections associated with the transitions to state f and to the ground state.

Since they are relative quantities, asymmetries [cf. Eq. (4.2)] and branching ratios [cf. Eq. (4.6)] are independent of the incident photon flux and the exact number of target nuclei (cf. Section 4.2.3). Thus, they can be determined precisely without any model dependency.

[85] Another convention, which is often used for transitions between well-developed rotational bands, features the normalization to the strongest decay branch.

4.3.3. Doublet decomposition

Although the excitation region of the incident γ-ray beam is rather low in energy, the expected level density of ^{162,164}Dy is already in the region of 10^3 states per MeV [286–289]. With higher level density also the probability increases that transitions of two states can no longer be resolved by the detector.[86] The presence of such a doublet can be traced through the asymmetries [cf. Eq. (4.2)], which are dependent on the involved angular momentum and parity quantum numbers. In practice, the asymmetries are especially sensitive to doublets consisting of $M1/E1$ and $E1/E2$ ground-state transitions (cf. Fig. 4.2). The experimental fingerprint for such a situation are damped, possibly even vanishing, asymmetry values in conjunction with transitions to lower-lying excited states. The latter condition is intended to ensure that no inelastic transition is mistaken for a doublet. In analogy to the procedure described in Section 4.3.1, the analyzing powers [cf. Eq. (4.3)] are calculated for a linear combination

$$W_{\text{Doublet}} = \alpha W_{0\to x_1\to f_1} + (1-\alpha) W_{0\to x_2\to f_2}$$

of two different[87] angular distribution functions $W_{0\to x_1\to f_1}$ and $W_{0\to x_2\to f_2}$. For each such combination, the parameter α is chosen such that the experimental asymmetries are reproduced in the best possible way. Subsequently, the overall conformity with the asymmetries is evaluated in terms of χ^2 values [cf. Eq. (4.4)]. This yields the most likely composition of the doublet.

From the knowledge of α, the integrated cross sections [cf. Eq. (3.1)] of the compounding transitions and, thus, branching ratios can be determined.[88] Since the asymmetries are only slightly pronounced for transitions to 2^+ states, the extraction of α is rather

[86] Naturally, the underlying problem comes with many variations. Multiplets may also occur due to ambient background radiation or transitions from other materials excited by photons of the γ-ray beam. For the sake of the argument, it is assumed that a doublet of transitions stemming from target nuclei is observed. Furthermore, it is taken for granted that the doublet peak exhibits an inconspicuous width, i.e. its composing peaks are separated by a small fraction of their FWHM.

[87] Naturally, a doublet can be composed of states with identical quantum numbers. With the present methods this is impossible to distinguish from a single excitation.

[88] It has to be stressed that α must be determined individually for each transition due to the potentially differing branching ratios of the composing states. Naturally, also the transitions to other lower-lying states are doublets if the ground-state transitions coincide.

complicated in these cases - especially if there are few statistics. An additional contribution to the uncertainty is then introduced which accounts for the possibility that one doublet state does not exhibit the particular branching transition.

5. Results

In this Chapter, the results of the experiments on ^{154}Gd and ^{162,164}Dy are presented. Using the methods outlined in Section 4.3, quantum numbers of previously unknown states as well as multipole-mixing and branching ratios of transitions to lower-lying states were determined. For each nucleus the results are summarized in tables. These include quantum numbers and energy-integrated cross sections for all observed states along with multipole-mixing ratios, branching ratios, and reduced transition strengths for depopulating transitions. Additional information is given for selected states.

5.1. The transitional nucleus ^{154}Gd

Dipole excitations of ^{154}Gd have previously been identified in the energy region of the scissors mode using electron scattering [253] and bremsstrahlung-induced photon scattering [19, 216]. In combination with $\gamma\gamma$-coincidence measurements after electron capture of ^{154}Tb, the latter experiments yielded branching ratios [cf. Eq. (4.6)] to lower-lying states for three 1^+ states at 2934.2(6), 3090.6(9), and 3122.55(24) keV [19]. The spectra of the present experiment, which was focused on the decay properties of the first state, are shown in Fig. 5.1 for detectors in the polarization plane and perpendicular to it [panel (a)] and at backward angles with respect to the beam axis [panel (b)]. Since the target material was enriched in ^{154}Gd to merely 66.78(20)% (cf. Appendix C.1) excitations of other stable gadolinium isotopes contribute to the spectra. The results for ^{154}Gd are summarized in Tab. 5.1. In the following, selected excited states are discussed in more detail.

The $J^\pi = 1^+_1$ state at 2934.2(6) keV represents the strongest known $M1$ excitation of ^{154}Gd. However, its excitation strength obtained from electron scattering [253]

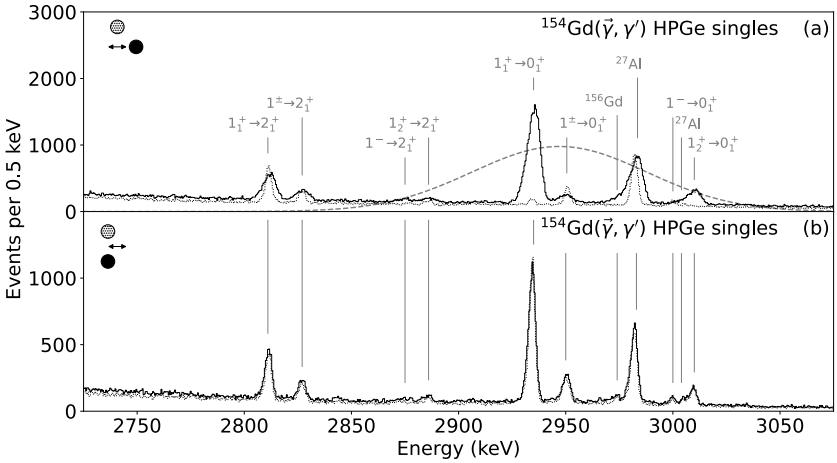

Figure 5.1.: Gamma-ray spectra from the ^{154}Gd($\vec{\gamma}, \gamma'$) reaction taken at HIγS with a beam energy $E_{\text{beam}} = 2948(95)$ keV. Besides excitations of ^{27}Al at 2982.00(5) and 3004.2(8) keV, the spectra are dominated by the $1_1^+ \to 0_1^+$ and $1_1^+ \to 2_1^+$ transitions of ^{154}Gd at 2934.1(6) and 2811.3(10) keV, respectively. Panel (a) shows the spectra of detectors placed in the polarization plane of the incident beam (solid) and perpendicular to it (dotted). The $\vec{\gamma}$-ray beam's energy distribution is indicated by a dashed Gaussian curve. Spectra of detectors at backward angles with respect to the beam axis are shown in panel (b).

is substantially smaller than the one from photon scattering [19, 216].[89] Due to the displacement of target and beam axes, whose consequences are outlined in Section 3.3.1, no independent value can be provided from the present work. Instead, all energy-integrated cross sections given in Tab. 5.1 are relative to the results of Refs. [19, 216]. The peak associated with the $1_1^+ \rightarrow 2_1^+$ transition is located at 2811.3(10) keV. Its asymmetry implies the existence of electric dipole strength and, thus, of a doublet structure. However, this possibility must be discarded due to the photon-flux distribution [cf. panel (a) of Fig. 5.1].[90] Instead, it is concluded that the measured asymmetry originates from a nonzero multipole-mixing ratio.

A $J^\pi = 2^+$ state at 2950 keV is listed in the data sheets [184]. From a later NRF experiment using bremsstrahlung [19], quadrupole character was excluded due to the incompatible angular distribution of the emitted photons. Instead, quantum numbers $J^\pi = 1^-$ were tentatively assigned due to the uncommon branching ratio but not without suggesting the possibility of a doublet. Indeed, this claim is supported by the present analysis of experimental asymmetries [cf. Eq. (4.2)]. It reveals the existence of a doublet consisting of 1^+ and 1^- states with energy-integrated cross sections of $9.6^{+1.8}_{-1.2}$ and $19.3^{+2.6}_{-2.7}$ eVb, respectively.[91]

Hitherto unknown electric dipole strength is identified at 3000 keV.[92] It does neither originate from ^{152}Gd nor from ^{160}Gd, both of which are present in the target material (cf. Appendix C.1) and excited states are reported at 2999.55(5) [183] and 2999(1) keV [186], respectively. While the parity does not match for the prior state,

[89] From electron scattering, a value $B(M1; 1_1^+ \rightarrow 0_1^+) = 0.32(3)\,\mu_N^2$ is reported [184, 253], in contrast to $B(M1; 1_1^+ \rightarrow 0_1^+) = 0.53(6)\,\mu_N^2$ from photon scattering [19, 216].

[90] The analysis of the peak's asymmetry yields an approximately 19% share of the $1^- \rightarrow 0_1^+$ component. In the data sheets of neither the isotopes contained in the target [79, 183–186, 290, 291] nor the surrounding material [254, 255, 280] such a transition is found. Assuming that the $E1$ contribution originates from the target material, an excitation strength in the range of $10^{-1}\,\mathrm{e}^2\mathrm{fm}^2$ is expected for the most abundant isotope ^{154}Gd. Even if the photon flux at this energy were underestimated by one order of magnitude, it is still unlikely that such a state would have remained undetected. For the less abundant gadolinium isotopes in the target material the situation is even more dramatic. Ultimately, independent experimental clarification is direly needed; for instance by an NRF experiment while effectively excluding the 1^+ state at 2934.2(6) keV from the excitation region.

[91] Their sum is in agreement with $I_{0\rightarrow x\rightarrow 0} = 34(8)$ eVb from Ref. [19].

[92] The peak at 3000 keV does not originate from a transition of ^{154}Gd which connects a 1^+ state at 3122.55(24) keV [184] and the 2_1^+ state. This can be ruled out in two ways; first, the corresponding 1^+ state is not excited by the photon beam since the ground-state transition is not observed and second, the asymmetry does not match the expected behavior for a $1^+ \rightarrow 2_1^+$ transition.

no transition to the 2_1^+ state of ^{160}Gd is observed at 2924(1) keV for the latter.[93] Instead, a γ-ray peak is observed at 2877 keV, which might stem from the transition to the 2_1^+ state of ^{154}Gd. Its count-rate asymmetry favors a $2^+ \rightarrow 2_1^+$ assignment while the evident $1^- \rightarrow 2_1^+$ nature cannot be completely ruled out. Correspondingly, the existence of a 1^- state of ^{154}Gd at 3000 keV with a branching transition to the 2_1^+ state at 2877 keV is tentatively adopted. In Section 6.2.3 the implications of a $J^\pi = 2^+$ state are discussed.

Eventually, a potential $J^\pi = 1^+$ state of ^{154}Gd is observed at 3009.7(4) keV along with its transition to the 2_1^+ state at 2887.1(8) keV. The existence of these γ-rays in the level scheme of ^{154}Gd is known from the decay of ^{154}Tb isomeric states [293]. However, states of ^{155}Gd and ^{156}Gd, which both have non-negligible shares of the target material, exist at 3011.0(1) [290, 294] and 3010 keV [79, 295], respectively. After correction of their contributions, an energy-integrated cross section of $43.3^{+9.8}_{-6.1}$ eVb is obtained.

[93] The upper limit for the branching ratio deduced from the sensitivity limit of the present experiment amounts to 0.14(1). It is significantly smaller than 0.39(13) reported in Ref. [292].

Table 5.1.: Properties of excited states of ^{154}Gd determined in the present work. Multipole-mixing ratios and branching ratios were determined as outlined in Sections 4.3.1 and 4.3.2, respectively. The latter are normalized to 100 for ground-state transitions. Energy-integrated cross sections are understood as upper limits in case of unobserved branching transitions.

E_x (keV)	$J_x^{\pi_x}$	$I_{0\to x\to 0}$ (eVb)	$E_{\gamma,x\to f}$ (keV)	$J_f^{\pi_f}$	$\delta_{x\to f}$	$R^{\mathrm{exp}}_{1\to f/0}$	$\sigma\lambda$	$B(\sigma\lambda; x\to f)$ (μ_N^2) or (10^{-3} e^{2}fm^2)
2934.2(6)[a]	1_1^+	$138^{+16b,c}_{-15}$	2934.1(6)[a]	0_1^+		100	$M1$	$0.517^{+0.061}_{-0.057}$
			2811.3(10)[a]	2_1^+	$-0.147^{+0.024}_{-0.032}$	$45.9^{+1.4}_{-1.7}$	$M1$	$0.237^{+0.026}_{-0.031}$
2950	1^+	$9.6^{+1.8}_{-1.2}$	2950	0_1^+		100	$M1$	$0.029^{+0.013}_{-0.015}$
			2827	2_1^+		23^{+56}_{-23}	$M1$	$0.002^{+0.026}_{-0.002}$
	1^-	$19.3^{+2.6}_{-2.7}$	2950	0_1^+		100	$E1$	$1.03^{+0.20}_{-0.20}$
			2827	2_1^+		103^{+33}_{-29}	$E1$	$0.93^{+0.58}_{-0.39}$
3000	1^-	$11.3^{+2.2}_{-1.4}$	3000	0_1^+		100	$E1$	$0.180^{+0.035}_{-0.032}$
			2877	2_1^+		$63.3^{+10.0}_{-\ 9.6}$	$E1$	$0.110^{+0.039}_{-0.031}$
3009.7(4)[a]	1_2^+	$43.3^{+9.8}_{-6.1}$	3009.6(5)[a]	0_1^+		100	$M1$	$0.161^{+0.026}_{-0.025}$
			2887.1(8)[a]	2_1^+		$49.7^{+5.2}_{-5.6}$	$M1$	$0.081^{+0.011}_{-0.014}$

[a] From Ref. [184].
[b] The integrated cross section of Ref. [19] was used for calibration of the incident photon flux.
[c] Using branching ratios to the $0^+_{2,3}$ and 1^-_1 states from Ref. [19].

5.2. The deformed nucleus ^{162}Dy

The dipole strength distribution in the energy region covered by the two beam settings is dominated by two $J^\pi = 1_i^+$ ($i \in \{1,2\}$) states. These are already known from NRF experiments using bremsstrahlung [154, 257, 258] and spectroscopy after inelastic neutron-scattering [259] and are interpreted as the main fragments of the $K = 1$ scissors mode. Their transitions to the ground-state are located at 2900.3(4) and 3061.4(4) keV and the transitions to the 2_1^+ state at 2819.0(4) and 2980.3(4) keV, respectively. For the latter, branching ratios and multipole-mixing ratios were determined. Beside these prominent states, additional weak excitations are identified in the $(\vec{\gamma}, \gamma')$ spectra shown in Fig. 5.2 for a detector in the polarization plane (solid) and perpendicular to it (dotted). These are briefly discussed in the following. A summary of the results for ^{162}Dy is given in Tab. 5.2.

At 2909.4(7) keV a $J^\pi = 1^-$ state is identified along with its transition to the 2_1^+ state at 2829 keV. It was already observed [154] but without parity assignment. The branching ratio is within two standard deviations in agreement with the Alaga prediction for $K = 0$.

Magnetic dipole excitations are found at 2929.4(7) and 2965 keV. Using Compton polarimetry, the first state was previously assigned negative parity [154], which is ruled out by the experimental asymmetries (cf. Section 4.3.1). While a branching transition to the 2_1^+ state is observed for the former, an upper limit of the latter's branching ratio can be inferred from the sensitivity limit. Agreement with the value reported in Ref. [154] is given.

In the spectra corresponding to a beam energy $E_{\mathrm{beam}} = 3069(119)$ keV [cf. panel (b) of Fig. 5.2] another weakly excited state is found at 3012.3(6) keV. Since it is also populated in thermal neutron capture of ^{161}Dy and the ^{163}Dy(d,t)^{162}Dy reaction [296], this state is attributed to ^{162}Dy. The measured asymmetries $[a_{0\to x\to 0}]_{ij}$ for all sensitive detector combinations (i, j), $i < j$, are inconclusive due to a lack of statistics. From a conformity analysis, negative parity is tentatively assigned. However, further clarification is needed since a doublet consisting of 1^- and 1^+ or 1^- and 2^+ states could also be present. A transition to the 2_1^+ state is observed at 2932 keV.

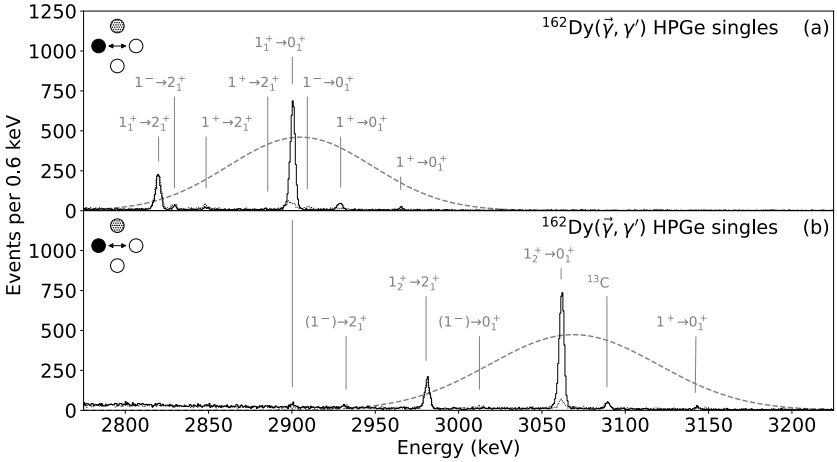

Figure 5.2.: Gamma-ray spectra from the ^{162}Dy($\vec{\gamma}, \gamma'$) reaction taken at HIγS with beam energies $E_{\text{beam}} = 2905(102)$ keV [panel (a)] and 3069(119) keV [panel (b)]. Detectors were placed at a polar angle of $\vartheta = 90°$ and azimuthally in the horizontal polarization plane (solid) of the incident $\vec{\gamma}$-ray beam or perpendicular to it (dotted). The luminosity profile of the $\vec{\gamma}$-ray beam in arbitrary units is indicated in gray by the dashed Gaussian curve. The spectra are dominated by the $1^+_i \to 0^+_1$ ($i \in \{1, 2\}$) transitions at 2900.3(4) and 3061.4(4) keV and the transitions to the 2^+_1 state at 2819.0(4) and 2980.3(4) keV, respectively.

Finally, an excited state is observed at 3142 keV. A resonance at that energy is reported from photon-scattering experiments off ^{163}Dy [297], which has a 1.79(1) percent[94] share of the target material (cf. Appendix C.2). Since no further γ-rays of ^{163}Dy are observed in the excitation energy region,[95] the γ-ray peak at 3142 keV is most likely not associated with ^{163}Dy. It is also neither associated with background radiation nor other isotopes excited by the incident photon beam. Due to the high resolution of the incident $\vec{\gamma}$-ray beam and the measured asymmetries, the state is tentatively attributed to ^{162}Dy with quantum numbers $J^\pi = 1^+$. Its expected decay to the 2_1^+ state is masked by the $1_2^+ \rightarrow 0_1^+$ transition at virtually the same energy.

In the excitation-energy region of the present experiment further states of ^{162}Dy are reported in the data sheets [187]. These were populated in particle-induced reactions [296, 298] but lack angular momentum and parity assignments. They either correspond to dipole excitations below the sensitivity limit of NRF experiments or rather are not excited from the ground state by absorption of photons.

[94] Uncertainties estimated from the last digit given in Ref. [262].

[95] The state of ^{163}Dy in question has an integrated cross section $I_{5/2^- \rightarrow x \rightarrow 5/2^-} = 2.07(19)$ eVb [297]. There exists, for instance, a state with a threefold larger integrated cross section at 3099 keV [297], which in addition also experiences a larger photon flux [cf. panel (b) of Fig. 5.2]. If the state were of ^{163}Dy it would most likely also be observed in the ^{164}Dy spectra. However, this is not the case (cf. Fig. 5.3).

Table 5.2.: Properties of excited states of ^{162}Dy determined in the present work. Multipole-mixing ratios and branching ratios were determined as outlined in Sections 4.3.1 and 4.3.2, respectively. The latter are normalized to 100 for ground-state transitions. Energy-integrated cross sections are understood as upper limits in case of unobserved branching transitions.

E_x (keV)	$J_x^{\pi_x}$	$I_{0\to x\to 0}$ (eVb)	$E_{\gamma,x\to f}$ (keV)	$J_f^{\pi_f}$	$\delta_{x\to f}$	$R^{\mathrm{exp}}_{1\to f\,/0}$	$\sigma\lambda$	$B(\sigma\lambda; x\to f)$ (μ_N^2) or (10^{-3} e^{2}fm^2)
2900.0(3)[a]	1_1^+	138^{+11}_{-10}[b]	2900.3(4)[a]	0_1^+		100	$M1$	$0.524^{+0.048}_{-0.036}$
			2819.0(4)[a]	2_1^+	$-0.053^{+0.051}_{-0.049}$	$53.1^{+3.7}_{-3.4}$	$M1$	$0.278^{+0.037}_{-0.029}$
2909.4(7)[a]	1^-	$3.49^{+0.73}_{-0.59}$	2909	0_1^+		100	$E1$	$0.249^{+0.038}_{-0.030}$
			2829	2_1^+		154^{+39}_{-25}	$E1$	$0.402^{+0.099}_{-0.091}$
2929.4(7)[a]	1^+	$10.4^{+1.0}_{-1.2}$[b]	2929	0_1^+		100	$M1$	$0.041^{+0.004}_{-0.004}$
			2849	2_1^+		$62.4^{+10.4}_{-9.7}$	$M1$	$0.026^{+0.005}_{-0.005}$
2965	1^+	$7.9^{+1.5}_{-1.4}$[b]	2965	0_1^+		100	$M1$	$0.028^{+0.005}_{-0.005}$
			2885	2_1^+		$\leq 42.6^{+8.8}_{-6.5}$	$M1$	$\leq 0.018^{+0.005}_{-0.004}$
3012.3(6)[a]	(1^-)	$1.94^{+0.72}_{-0.55}$	3012	0_1^+		100	$E1$	$0.117^{+0.034}_{-0.022}$
			2932	2_1^+		111^{+55}_{-39}	$E1$	$0.136^{+0.085}_{-0.052}$
3061.2(3)[a]	1_2^+	$85.9^{+6.3}_{-6.6}$[b]	3061.4(4)[a]	0_1^+		100	$M1$	$0.282^{+0.018}_{-0.025}$
			2980.3(4)[a]	2_1^+	$0.065^{+0.057}_{-0.058}$	$34.7^{+3.1}_{-2.5}$	$M1$	$0.096^{+0.013}_{-0.011}$
3142	1^+	$4.3^{+1.1}_{-0.9}$	3142	0_1^+		100	$M1$	$0.010^{+0.003}_{-0.002}$

[a] From Ref. [187].
[b] The integrated cross sections of Ref. [154] were used for calibration of the incident photon flux.

5.3. The deformed nucleus ^{164}Dy

Dipole states of ^{164}Dy around 3 MeV have previously been studied in NRF experiments using bremsstrahlung [154, 257, 261] and monochromatic photon beams [261], as well as in electron [144, 260], proton [299], and neutron scattering [259]. The dipole strength distribution in this energy region is dominated by three 1_i^+ states ($i \in \{1,2,3\}$)[96] at 3111.2(3), 3159.1(3), and 3173.6(3) keV. Decay branching ratios and multipole-mixing ratios were determined for their transitions to the 2_1^+ state at 3037.8(4), 3085.3(4), and 3100.1(4) keV, respectively. In addition, further weak dipole excitations are characterized from the $(\vec{\gamma},\gamma')$ spectra shown in Fig. 5.3 for a detector in the polarization plane (solid) and perpendicular to it (dotted). A summary of the obtained results is given in Tab. 5.3.

At 3069 and 3073 keV, two peaks are identified in the spectra corresponding to a beam energy of 3185(102) keV. Although the time- and energy-integrated photon flux around 3070 keV is significantly larger for $E_{\mathrm{beam}} = 3076(98)$ keV (cf. Fig. 4.1), the peaks are not observed in the corresponding spectra shown in Fig. 5.3, panel (a). Hence, they might be inelastic transitions of the previously conjectured ground-state transitions of $J = 1$ states [261]. The acquired statistics is not sufficient for a reliable determination of the excited states' quantum numbers.

A combination of the beam's high energy resolution and the coincidence capabilities of the γ^3 setup enables the final confirmation of the existence of nuclear states of ^{164}Dy at 3100 keV. Hitherto, the existence of a single excited state was tentatively conjectured [259, 261]. Concurrently, a state at 3099 keV was also reported from photon-scattering experiments off ^{163}Dy with energy-integrated cross sections $I_{0\to x\to 0} = 8.8(12)$ [154] and 6.83(51) eVb [297].[97] Since this state was observed in no other reaction [300] and the target materials of both NRF experiments contained notable amounts of ^{164}Dy,[98] it might be concluded that the level scheme of ^{163}Dy does not contain a state at 3099 keV. The measured asymmetries favor a doublet structure

[96] The 1_2^+ and 1_3^+ states at 3159.1(3) and 3173.6(3) keV, respectively, were not resolved in the (e,e') experiments of Refs. [144, 260].

[97] The energy-integrated cross sections reported in Ref. [154] are systematically larger than the ones given in Ref. [297].

[98] The targets contained 4.5% [154] and 8.02% [297] of ^{164}Dy and were enriched to 92.8% and 89.90% in ^{163}Dy, respectively. In fact, the authors of Ref. [297] claim to have observed transitions from 41 out of 44 known states of ^{164}Dy in the studied energy region.

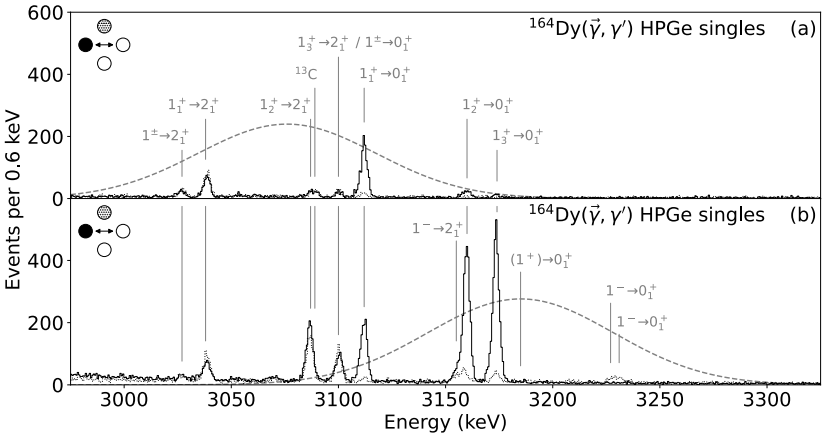

Figure 5.3.: Gamma-ray spectra from the ^{164}Dy($\vec{\gamma}, \gamma'$) reaction taken at HIγS with beam energies $E_{\text{beam}} = 3076(98)$ keV [panel (a)] and 3185(102) keV [panel (b)]. Detectors were placed at a polar angle of $\vartheta = 90°$ and azimuthally in the horizontal polarization plane (solid) of the incident $\vec{\gamma}$-ray beam or perpendicular to it (dotted). The luminosity profile of the $\vec{\gamma}$-ray beam in arbitrary units is indicated in gray by the dashed Gaussian curve. The spectra are dominated by the $1_i^+ \to 0_1^+$ ($i \in \{1,2,3\}$) transitions at 3111.0(4), 3159.4(4), and 3173.6(4) keV and the transitions to the 2_1^+ state at 3037.8(4), 3085.3(4), and 3100.1(4) keV, respectively.

consisting of $J^\pi = 1^+$ and 1^- states of ^{164}Dy instead. Due to the nearly isotropic angular distribution, no reliable decomposition is possible for the transitions to the 2^+_1 and 2^+_γ states. Thus, upper limits are deduced for the respective branching ratios (cf. Section 4.3.3).

Another state with an inconclusive asymmetry is found at 3125 keV. It is also reported from photon-scattering experiments off ^{163}Dy [297]. However, no further γ-rays of ^{163}Dy are observed in the excitation region.[99] The state is instead attributed to ^{164}Dy and features a transition to the 2^+_1 state at 3052 keV [261]. Due to the lack of statistics, no reliable determination of quantum numbers or branching ratios is possible.

For the 1^+_3 state at 3173.6(3) keV, the branching ratio to the 2^+_1 state deviates significantly from the Alaga prediction for transitions between $K = 1$ and $K = 0$ bands. The value determined in the present experiment is even smaller than the ones from Refs. [154, 261]; but it is in agreement with the results reported in Refs. [257, 259]. Moreover, a considerable decay branch to the 2^+_γ state at 761.815(7) keV is identified in the coincidence spectra [cf. panels (b) and (d) of Fig. 5.4].

Ultimately, negative parity is assigned to two excitations found at 3228.0(7) (cf. Fig. 4.2) and 3231.0(10) keV [154, 261]. While a branching ratio is determined for the former, no depopulating transition to the 2^+_1 state is identified for the latter state.

[99] The state of ^{163}Dy in question has an integrated cross section $I_{5/2^-\to x\to 5/2^-} = 0.50(11)$ eVb [297]. There exist, for instance, states with comparable integrated cross sections at 3137 and 3206 keV [297], which in addition also experience a larger photon flux [cf. panel (b) of Fig. 5.3].

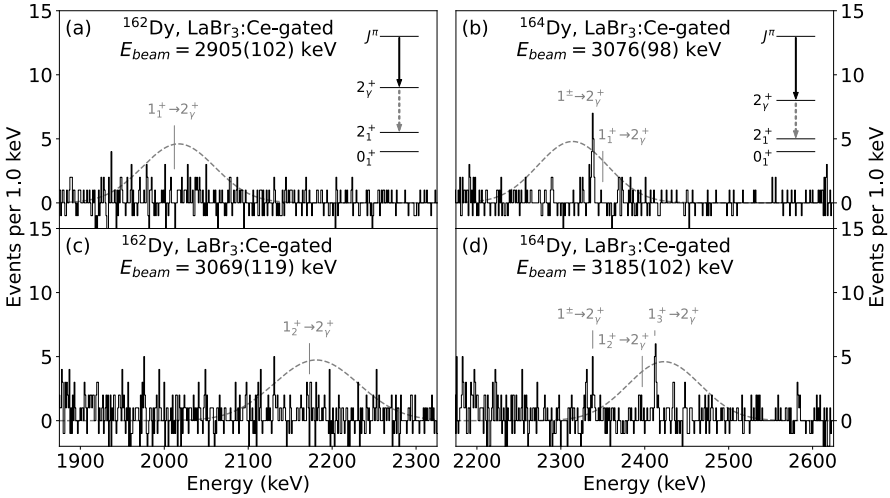

Figure 5.4.: Coincidence spectra from the ^{162}Dy$(\vec{\gamma},\gamma'\gamma'')$ [panels (a) and (c)] and ^{164}Dy$(\vec{\gamma},\gamma'\gamma'')$ reactions [panels (b) and (d)]. They feature an energy condition in the LaBr$_3$:Ce scintillators on the $2^+_\gamma \rightarrow 2^+_1$ transition, which is illustrated by grey dotted arrows in the levelschemes of panels (a) and (b). Schematic luminosity profiles of the incident $\vec{\gamma}$-ray beams, shifted by the excitation energy of the 2^+_γ state, are indicated in gray by dashed Gaussian curves. For ^{162}Dy, the existence of a decay branch to the 2^+_γ state can be excluded for the 1^+_1 state at 2900.0(3) keV [panel (a)]. The data is, however, not clear for the 1^+_2 state at 3061.2(3) keV [panel (c)]. In the case of ^{164}Dy, on the other hand, the $1^\pm \rightarrow 2^+_\gamma$ and $1^+_3 \rightarrow 2^+_\gamma$ transitions clearly manifest themselves in the coincidence spectra [panels (b) and (d)]. In addition, there is weak evidence for a coupling of the 1^+_2 state at 3159.1(3) keV to the γ vibration but not for the 1^+_1 state at 3111.2(3) keV.

Table 5.3.: Properties of excited states of ^{164}Dy determined in the present work. Multipole-mixing ratios and branching ratios were determined as outlined in Sections 4.3.1 and 4.3.2, respectively. The latter are normalized to 100 for ground-state transitions. Energy-integrated cross sections are understood as upper limits in case of unobserved branching transitions.

E_x (keV)	$J_x^{\pi_x}$	$I_{0\to x\to 0}$ (eVb)	$E_{\gamma,x\to f}$ (keV)	$J_f^{\pi_f}$	$\delta_{x\to f}$	$R^{\mathrm{exp}}_{1\to f/0}$	$\sigma\lambda$	$B(\sigma\lambda; x\to f)$ (μ_N^2) or (10^{-3} e^{2}fm^2)
3100	1^+	$5.0^{+1.2}_{-1.2}$	3100	0^+_1		100	$M1$	$0.066^{+0.012}_{-0.008}$
			3027	2^+_1		$\leq 184^{+60}_{-33}$	$M1$	$\leq 0.129^{+0.042}_{-0.028}$
			2338	2^+_γ		$\leq 514^{+163}_{-111}$	$M1$	$\leq 0.36^{+0.12}_{-0.09}$
	1^-	$5.9^{+1.3}_{-1.3}$	3100	0^+_1		100	$E1$	$0.79^{+0.10}_{-0.12}$
			3027	2^+_1		$\leq 168^{+38}_{-32}$	$E1$	$\leq 1.31^{+0.35}_{-0.28}$
			2338	2^+_γ		$\leq 444^{+115}_{-90}$	$E1$	$\leq 3.40^{+1.13}_{-0.79}$
3111.2(3)[a]	1^+_1	111^{+11}_{-13}[b]	3111.0(4)[a]	0^+_1		100	$M1$	$0.392^{+0.040}_{-0.038}$
			3037.8(4)[a]	2^+_1	$-0.13^{+0.08}_{-0.08}$	$49.5^{+5.2}_{-4.7}$	$M1$	$0.196^{+0.024}_{-0.023}$
3125			3125[c]	0^+_1		100		
			3052[c]	2^+_1				
3159.1(3)[a]	1^+_2	$74.2^{+6.9}_{-5.8}$[b]	3159.4(4)[a]	0^+_1		100	$M1$	$0.282^{+0.018}_{-0.024}$
			3085.3(4)[a]	2^+_1	$0.13^{+0.06}_{-0.06}$	$61.2^{+5.5}_{-5.8}$	$M1$	$0.167^{+0.021}_{-0.017}$
3173.6(3)[a]	1^+_3	$71.5^{+5.4}_{-4.7}$[b]	3173.6(4)[a]	0^+_1		100	$M1$	$0.225^{+0.014}_{-0.014}$
			3100.1(4)[a]	2^+_1	$0.07^{+0.09}_{-0.10}$	$26.9^{+2.9}_{-2.6}$	$M1$	$0.061^{+0.007}_{-0.007}$
			2411	2^+_γ		$15.5^{+3.2}_{-2.4}$	$M1$	$0.036^{+0.006}_{-0.007}$
3185	1^+	$1.04^{+0.31}_{-0.30}$	3185	0^+_1		100[c]	$0.0024^{+0.0007}_{-0.0007}$	
3228.0(7)[a]	1^-	$3.39^{+0.93}_{-0.85}$	3228	0^+_1		100	$0.326^{+0.042}_{-0.045}$	
			3154.5	2^+_1		253^{+90}_{-53}	$0.88^{+0.25}_{-0.23}$	
3231.0(10)[a]	1^-	$3.58^{+0.93}_{-0.93}$	3231	0^+_1		100	$0.092^{+0.024}_{-0.024}$	

[a] From Ref. [187].
[b] The integrated cross sections of Ref. [261] were used for calibration of the incident photon flux.
[c] Observed in only one detector.

6. Discussion

The results presented in Chapter 5 show that 1^+ states of ^{164}Dy, which were hitherto interpreted as pure scissors mode states, exhibit a decay behavior strongly deviating from the Alaga predictions. As shown in Section 6.1, this can be described by a K-mixing scenario involving previously unobserved 1^+ states which are characterized by projection quantum number $K = 0$ and negative $\mathscr{R}$ symmetry (cf. Section 2.1.2). Furthermore, it is observed that the multipole-mixing ratios for transitions between 1^+ states of the scissors mode and the 2^+_1 state of the ground-state band are larger in the transitional nucleus ^{154}Gd than in the axially deformed nuclei ^{162,164}Dy. In Section 6.2 it is demonstrated, that this enables a mapping of the quadrupole boson charges of the IBM-2 (cf. Section 2.3) across the $N = 90$ shape-phase transition (cf. Section 2.5).

The results presented in Section 6.1 have in parts already been published in Ref. [301]. The discussion in Section 6.2 represents a natural continuation of the work reported in Refs. [24, 302, 303].

6.1. $\Delta K = 0$ $M1$ strength from K mixing

The scissors-mode rotational band of quadrupole deformed nuclei is, as indicated in Chapter 1, characterized by projection quantum number $K = 1$. This assignment is corroborated by studies within a variety of geometrical nuclear models [138–141, 304], the random-phase approximation (RPA) [159, 208] or mean-field methods [305]. Thus, scissors-mode states are, by virtue of the Alaga rule [46], expected to exhibit a branching ratio [cf. Eq. (4.5)] of 0.5 in contrast to 2.0 for dipole states with $K = 0$. Indeed, a broad survey of experimental branching ratios [[306] and Fig. 9 of [17]] unveiled a predominance of these values for deformed rare-earth and actinide nuclei.[100] Deviations from these limits were generally taken as evidence for K mixing [17, 306]. In the case of the scissors mode, the only possible admixture to the wave function must be characterized by $K = 0$.[101] As shown in panel (a) of Fig. 2.2, a potential signature for considerable K mixing is the observation of two dipole states with opposite deviations from 0.5 for the branching ratio.

6.1.1. K-mixing analysis

In the case of ^{164}Dy (cf. Section 5.3), such a situation is observed for the 1^+_2 and 1^+_3 states at 3159.1(3) and 3173.6(3) keV, respectively. Their branching ratios into the $K = 0$ ground-state band deviate significantly from the Alaga estimate 0.5; especially the 12σ violation for the 1^+_3 state stands out. The branching ratio of the 1^+_1 state at 3111.2(3) keV, on the other hand, is in agreement with the Alaga prediction. Hence, it is reasonable to consider only the energetically close-lying 1^+_2 and 1^+_3 states in a K-mixing scenario. The formalism introduced in Section 2.2 tacitly presupposes a pure $K = 0$ configuration for the 2^+_1 state, i.e. that it is the rotational excitation of the

[100] Prior to the advent of entirely polarized photon beams (cf. Sections 3.2 and 4.3.1), parity assignments of dipole states were based upon the comparison of measured branching ratios to Alaga predictions. For mid-shell nuclei such as ^{172,174}Yb, the results have shown to be robust [307]. In general, however, the method is prone to errors since it assumes the nonexistence of $J^\pi = 1^+$ states with projection quantum number $K = 0$ (cf. Section 2.1.2) and the validity of the Alaga rule. Especially for transitional nuclei the latter is not applicable which resulted in incorrect parity assignments for e.g. ^{150,152}Sm [92, 230, 308].

[101] The K quantum number is the projection of the angular momentum quantum number J onto the intrinsic symmetry axis (cf. Section 2.1). Thus, K can only take values $K \in [-J, J] \cap \mathbb{Z}$. In the case of axial symmetry, this set is reduced to its largest nonnegative subset.

ground state.[102] First of all, this implies that the leading-order intensity relations for $E2$ transitions within a rotational band [Sec. 4-3b of [4]] have to be fulfilled. Indeed, the value

$$B(E2; 2_1^+ \to 0_1^+) = \frac{5}{16\pi} e^2 Q_0^2 \langle 2020|00\rangle^2 = 198^{+26}_{-31}\,\text{W.u.},$$

which is derived from the intrinsic quadrupole moment Q_0[103] [Eq. (4-68b) ibid.] of the 2_1^+ state, is in agreement with a transition strength of 211(4) W.u. adopted in the data sheets [188]. A similar behavior is expected for $E2$ transitions between states with higher angular momenta [Fig. 4-24 ibid.]. Additional evidence for the approximate K purity of the 2_1^+ state can be collected from branching ratios of higher-lying excited states into the lower ground-state band. For instance, these are known for a multitude of dipole states up to 4 MeV [154] and, in many cases, are in excellent agreement with the Alaga predictions for unique K assignments. Thus, the assumption of $K = 0$ for the 2_1^+ state is reasonable and the 1_2^+ and 1_3^+ states can be treated in the two-state K-mixing model of Section 2.2.

Adopting ansatz (2.4), wave functions of the considered states can be fully decomposed into basis states with pure projection quantum numbers $K = 0$ and $K = 1$, i.e.

$$\begin{aligned} |1_3^+\rangle &= \quad \alpha|1^+_{K=0}\rangle + \beta|1^+_{K=1}\rangle \text{ and} \\ |1_2^+\rangle &= -\beta|1^+_{K=0}\rangle + \alpha|1^+_{K=1}\rangle \end{aligned} \tag{6.1}$$

with normalized amplitudes α and β. As outlined in Section 2.2, the TSM parameters $Z = \langle K_f = 1|||\boldsymbol{T}(M1)|||K_i = 0\rangle / \langle K_f = 0|||\boldsymbol{T}(M1)|||K_i = 0\rangle$ and $\gamma = \beta/\alpha$ are obtained from the branching ratios $R_{1_2 \to 2/0}$ and $R_{1_3 \to 2/0}$ (cf. Tab. 5.3) and the ratio of transition strengths $B_{2/3} = B(M1; 0_1^+ \to 1_2^+)/B(M1; 0_1^+ \to 1_3^+)$ [154, 257, 259, 261]. Since a potential solution (Z, γ) to the TSM scenario must satisfy all three conditions simultaneously [cf. panel (a) of Fig. 6.1], the compatibility with respect to the experimental constraints is evaluated in terms of χ^2 values. As shown in panels (b) and (c) of Fig. 6.1, the most probable solution, which corresponds to minimum χ^2, is character-

[102] Naturally, the 0_1^+ state must have $K = 0$. See footnote [101].

[103] The intrinsic quadrupole moment Q_0 is obtained from the spectroscopic quadrupole moment Q by the relation $Q = \langle JK20|JK\rangle\langle JJ20|JJ\rangle Q_0 = (3K^2 - J(J+1))/((J+1)(2J+3))Q_0$ [Eq. (4-69) of [4]] using the experimental value $Q = -2.08(15)$ b [309, 310].

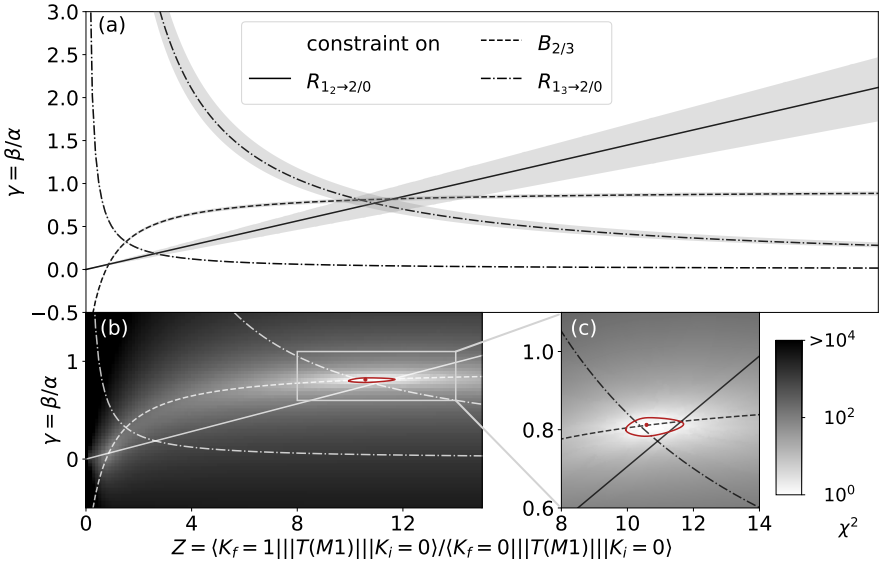

Figure 6.1.: Visualization of the experimental constraints $R_{1_2\to 2/0}$ (solid), $R_{1_3\to 2/0}$ (dash-dotted), and $B_{2/3}$ (dashed) in the Z-γ plane of the TSM parameters [panel (a)]. Due to an undefined phase of the initial problem, two constraints from $R_{1_3\to 2/0}$ have to be considered. A potential solution (Z, γ) to the TSM scenario must simultaneously satisfy three conditions, namely on $B_{2/3}$, $R_{1_2\to 2/0}$, and one on $R_{1_3\to 2/0}$. Their compatibility is evaluated in terms of χ^2 values. As depicted in panel (b) and highlighted in panel (c), mixing parameters corresponding to a dominant $\Delta K = 1$ matrix element and comparably strong mixing are favored by the experimental data. The adopted solution, which corresponds to minimum χ^2, along with its 1σ confidence interval are indicated in red.

ized by comparably strong mixing and a dominant $\Delta K = 1$ $M1$ matrix element.[104] The resulting TSM parameters are

$$\alpha^2 = 0.60^{+0.02}_{-0.01}, \qquad \beta^2 = 0.40^{+0.01}_{-0.02}, \text{ and}$$
$$Z = \frac{\langle K_\mathrm{f} = 1 | | | \boldsymbol{T}(M1) | | | K_\mathrm{i} = 0 \rangle}{\langle K_\mathrm{f} = 0 | | | \boldsymbol{T}(M1) | | | K_\mathrm{i} = 0 \rangle} = 10.6^{+1.0}_{-0.7}. \tag{6.2}$$

This means that the wave functions of the 1^+_2 and 1^+_3 states contain significant $K = 0$ and $K = 1$ contributions. Thus, both states are by no means pure $K = 1$ scissors-mode states as previously assumed [154, 257, 259]. The extracted value for Z indicates that $\Delta K = 0$ $M1$ excitations are suppressed by about two orders of magnitude. Compared to typical $\Delta K = 1$ $M1$ excitation strengths in this energy region [149, 150, 161], this explains why such excitations have never been observed directly and were assumed to be only weakly excited below 4 MeV [311]. In fact, the excitation strength of the unperturbed $1^+_{K=0}$ basis state is determined to [cf. Eq. (A.2)]

$$B(M1; 0^+_1 \to 1^+_{K=0}) = 0.008(1)\,\mu_N^2. \tag{6.3}$$

Merely by mixing with a strongly excited $1^+_{K=1}$ state, as encountered for ^{164}Dy, states with negative $\mathscr{R}$-symmetry quantum number are experimentally accessible.[105] In the disfavored case of weak mixing [cf. panel (b) of Fig. 6.1], comparable $\Delta K = 0$ and $\Delta K = 1$ $M1$ excitation strengths are expected leaving it unlikely that nuclear states with a dominant $K = 0$ component in the wave function remained undetected.

While this finding changes the interpretation of the involved states in terms of their intrinsic structure, the total low-lying orbital $M1$ strength[106] is not reduced appreciably. Quite to the contrary, the summed scissors-mode strength of ^{164}Dy even exceeds the value expected from systematics by approximately 50% [160]. The agreement can be

[104] From panel (a) of Fig. 6.1, two potential solutions can be identified; one corresponding to little mixing and comparable $\Delta K = 0$ and $\Delta K = 1$ $M1$ matrix elements, the other to strong mixing and a dominant $\Delta K = 1$ $M1$ matrix element. The analysis of their agreement with the experimental constraints [cf. panels (b) and (c) of Fig. 6.1] yields $\chi^2_\mathrm{min} \approx 45.7$ for the first option and $\chi^2_\mathrm{min} \approx 1.4$ for the second.

[105] At least for experiments at HIγS (cf. Section 3.2) and a typical beam time of about 100 hours. With the availability of ELI-NP's VEGA (Variable energy Gamma-ray) system, whose peak photon flux will surpass HIγS by at least one order of magnitude, the direct investigation of such states is within reach.

[106] The low-lying magnetic dipole strength of ^{164}Dy is split into two groups around 2.5 and 3.1 MeV [154, 257, 259, 260]. States of the first group were excluded from systematics [154] due to a nearly pure two-quasiparticle $M1$ excitation found in this region [312].

restored [154], taking into account a possible spin admixture[107] to the states around 3.1 MeV [299]. By construction, this contribution does not alter the results of the K-mixing analysis if orbital and spin $M1$ strength are distributed equally among the 1_2^+ and 1_3^+ states. Results from an RPA calculation with a self-consistent symmetry restoring quadrupole interaction indeed show, that all 1^+ states around 3.1 MeV have spin contributions [313], albeit their highly overestimated share in the transition strength [299]. Such spin strength is most likely not associated with the identified $1_{K=0}^+$ excitation. It is rooted in the shell structure of the nucleus, whereas the K quantum number is a concept of geometrical models.

In the past, the scissors mode of ^{164}Dy has also been investigated [314] in the framework of RPA and the quasiparticle-phonon nuclear model (QPNM) [315, 316]. The majority of the calculated magnetic dipole states below 4 MeV are of orbital nature and have a summed overlap of about 50% with the scissors-mode state.[108] Three $1_{K=1}^+$ states in the vicinity of 3 MeV are identified with the 1_i^+ ($i \in \{1,2,3\}$) states at 3011.2(3), 3159.1(3), and 3173.6(3) keV. Their excitation strengths are calculated to 0.32, 0.19, and 0.61 μ_N^2 using standard quenched gyromagnetic spin factors [17, 26, 317]. In addition, the QPNM calculation revealed three $1_{K=0}^+$ states at 1982, 3852, and 3965 keV, respectively. Microscopically, these are two-quasiparticle neutron states with excitation strengths equal to 0.0344, 0.0372, and 0.0025 μ_N^2. There is a caveat if a direct comparison of $\Delta K = 0$ and $\Delta K = 1$ $M1$ excitations is attempted. While the computed and experimental number of states as well as the total $M1$ strength are in agreement with each other, the results differ strongly for their distribution and intensity [314]. Thus, only bulk properties are discussed and a mapping of calculated to experimentally observed states is avoided. Invoking Eqs. (4-92) of Ref. [4] and (3.4), the quantity Z is extracted for all combinations of $\Delta K = 0$ and $\Delta K = 1$ $M1$ excitation strengths obtained from the QPNM via

$$Z_{\mathrm{QPNM}} = \frac{1}{\sqrt{2}} \sqrt{\frac{B(M1; 0_1^+ \to 1_{K=1}^+)_{\mathrm{QPNM}}}{B(M1; 0_1^+ \to 1_{K=0}^+)_{\mathrm{QPNM}}}}.$$

[107] From proton scattering, a sizeable spin $M1$ strength of $B(M1; 0_1^+ \to 1^+) = 0.50(7)\,\mu_N^2$ is identified at 3.14 MeV [299]. Due to the poor energy resolution, the corresponding peak encompasses at least the 1^+ states at 3111.2(3), 3159.1(3), and 3173.6(3) keV.

[108] In RPA, the remaining half is located in the region between 17 and 25 MeV. This might correspond to the rotational oscillation between rigid rotors, which was initially suggested in the TRM [139, 143]. Three groups of spin $M1$ strength are found at 6, 8, and 11 MeV [314].

This yields values for Z_{QPNM} which are in the same order of magnitude as the experimental value [cf. Eq. (6.2)], but are systematically smaller. Quantitatively, they range from 1.6 to 11.0 with 4.3 as mean value. Based on the previously mentioned shortcomings, there are two possible explanations. On average, the calculated $\Delta K = 1$ $M1$ excitation strengths are underestimated by a factor of about 2.5. In the unlikely case that this does not apply to the $1^+_{K=0}$ states, Z_{QPNM} is raised by about 60% only. If, on the other hand, the experimentally deduced $B(M1; 0^+_1 \rightarrow 1^+_{K=0})$ value [cf. Eq. (6.3)] is below average, a generally lower Z would be expected. Unless more experimental data on (dipole) states with negative $\mathscr{R}$-symmetry is available, these questions cannot be answered conclusively.

6.1.2. Mixing matrix elements from the Coriolis interaction

As shown in Section 6.1.1, deviations between the determined branching ratios and the Alaga predictions can be explained by K mixing of two close-lying $J^\pi = 1^+$ states with intrinsic projection quantum numbers $K = 0$ and $K = 1$. Such an admixture of different intrinsic configurations with good K quantum number is caused by a perturbation in a schematic Hamiltonian comprising intrinsic and rotational parts (cf. Section 2.2). In the following, mixing by means of the Coriolis interaction [Sec. 4-4 of [4]] is introduced.

The lowest-order coupling term of the Coriolis interaction is proportional to the rotational angular momentum [Eq. (4-196) ibid.] and couples in leading order intrinsic excitations differing by $\Delta K = \pm 1$ or if both are characterized by $K = 1/2$. Naturally, the mixing discussed in Section 6.1.1 corresponds to the first case. The magnitude of the involved mixing matrix element V_{mix} can be obtained from the mixing amplitudes α and β and the perturbed energies of the involved states (cf. Appendix A.2). Using the adopted TSM parameters [cf. Eq. (6.2)], a matrix element

$$V_{\mathrm{mix}} = \alpha\beta[E(1^+_3) - E(1^+_2)] = 6.85(4)\,\mathrm{keV}$$

and unperturbed energies 3164.5(2) and 3167.5(2) keV are obtained. Despite its small size, this matrix element produces a large mixture of both configurations due to their small energy difference. For even-even nuclei, additional experimental information on first-order Coriolis mixing is virtually inexistent.[109] Instead, extensive experimental

[109] Coriolis mixing with $\Delta K = \pm 1$ is commonly encountered in the spectra of heavy deformed odd-A nuclei; e.g. for the $K^\pi = 7/2^+$ and $5/2^+$ bands of ^{175}Lu [318].

data on rotational bands built upon low-lying quadrupole-collective excitation modes is available.

In second order, the Coriolis interaction admixes different intrinsic excitations with $\Delta K = \pm 2$ through intermediate states[110] with $\Delta K = \pm 1$. An example of this type is the mixing between the $K = 0$ ground-state and $K = 2$ γ-vibrational bands, which was studied systematically in even-even rare-earth nuclei [94, 319, 320]. Even slight mixing has a paramount effect on the transitions between the coupled bands, since the admixed collective matrix elements are large compared to typical interband transitions.[111] In the following, a small mixing amplitude and a mixing separable into spin-dependent and spin-independent parts [Eqs. (6.22) and (6.23) of [44]] are presupposed.[112] The associated mixing matrix element can then be extracted using the Mikhailov plot formalism [4, 323, 324]. It exploits the fact that the $E2$ transition matrix element can be rewritten [Eqs. (4-98) and (4-230) of [4]] as[113]

$$\sqrt{\frac{B(E2; J_\gamma \to J_1')}{2\langle J_\gamma 2\, 2 -2 | J_1' 0\rangle^2}} = M_1 - M_2[J_1'(J_1'+1) - J_\gamma(J_\gamma+1)], \tag{6.4}$$

where M_1 is related to the intrinsic unmixed $\Delta K = 2$ $E2$ matrix element and M_2 is directly proportional to the spin-independent part $\epsilon_{\Delta K=\pm 2}$ of the mixing amplitude. Since experimental values of interband transition strengths are known only for the $2_\gamma^+ \to 4_1^+$, $2_\gamma^+ \to 2_1^+$, and $2_\gamma^+ \to 0_1^+$ transitions [188], M_1 and M_2 are simultaneously also

[110] Details on these states do not need to be known for the presented analysis. It is only assumed that their excitation energies are large compared to the $\Delta K = \pm 2$ mode [4]. Naturally, also two bands with $K = 0$ can be admixed in second order.

[111] The effect on the intraband $E2$ transitions, on the other hand, is negligible since a fraction of an already small interband matrix element is added to a much larger intraband matrix element.

[112] The complete formalism of this mechanism, which is commonly referred to as bandmixing, is given e.g. in Refs. [44, 321, 322].

[113] In the derivation of Eq. (6.4), equal intrinsic quadrupole moments for $K = 0$ and $K = 2$ bands are presupposed. In the case of ^{164}Dy, experimental information on quadrupole moments is available solely for the 2_1^+ state [309, 310]. For ^{166,170}Er, on the other hand, absolute values have been determined [325] also for the spectroscopic quadrupole moments of the 2_γ^+ states. Assuming equal signs, the resulting intrinsic quadrupole moments for the $K = 0$ and $K = 2$ bands coincide within uncertainties. Since ^{166,170}Er exhibit an axially-symmetric deformation comparable to the one of ^{164}Dy, a similar behavior is expected for the latter nucleus. If this assumption is not fulfilled, a more general relation of Eq. (6.4) is given in Eqs. (4-235) and (4-236) of Ref. [4]. In fact, it is assumed that the intrinsic quadrupole moment of the γ-vibrational is about 10% larger than that of the ground-state band [326]. However, the corresponding original data is not published.

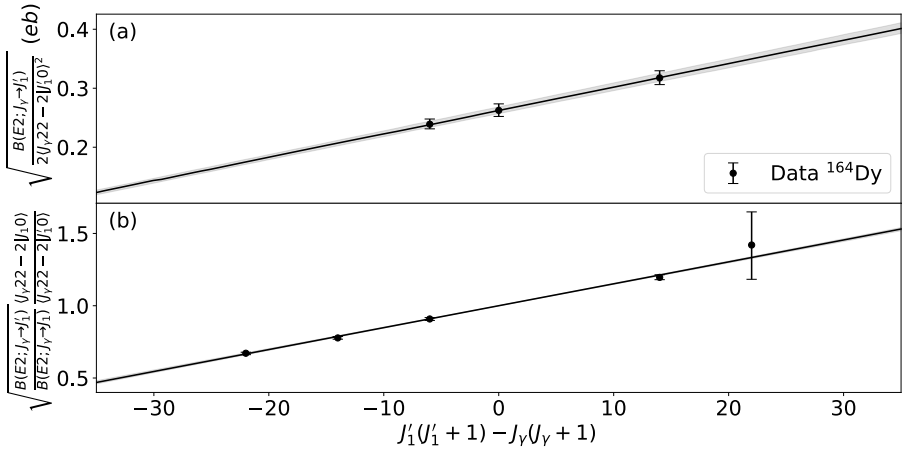

Figure 6.2.: Mikhailov plot for transitions between the γ-vibrational and ground-state bands of ^{164}Dy. The parameters M_1 and M_2 [cf. Eq. (6.4)] are given by the intercept and the slope of the adapted linear model shown in panel (a), respectively. Although transition strengths are available only for transitions originating from the 2^+_γ state, the obtained parameters (6.6) are dependable due to the inclusion of additional data on branching ratios [cf. Eq. (6.5)] depicted in panel (b).

adapted to branching ratios via

$$\sqrt{\frac{B(E2;J_\gamma \to J_1')}{B(E2;J_\gamma \to J_1)}}\frac{\langle J_\gamma 22-2|J_1 0\rangle}{\langle J_\gamma 22-2|J_1'0\rangle} = 1-\frac{M_2}{M_1}[J_1'(J_1'+1)-J_\gamma(J_\gamma+1)]. \tag{6.5}$$

This expression is valid if the branching ratios are defined relative to the transition that preserves angular momentum. For transitions between the γ-vibrational and the ground-state bands of ^{164}Dy, the resulting Mikhailov plot is shown in Fig. 6.2. Assuming pure $E2$ character for these [327],

$$M_1 = 0.263(6)\,e\mathrm{b} \qquad \text{and} \qquad M_2 = -0.0040(1)\,e\mathrm{b} \tag{6.6}$$

are obtained for the intercept at $J_\gamma = J_1'$ and the slope of the right-hand side of

Eq. (6.4), respectively. The bandmixing parameter Z_γ is determined to [44, 319]

$$Z_\gamma = -\frac{2M_2}{M_1 + 4M_2} = 0.0322(7).$$

This value agrees well with literature values [327] and the empirical systematics which show a parabolic behavior minimizing at midshell [319, 320]. On the other hand, Z_γ can also be determined from branching ratios only. As expected, the obtained value $Z_\gamma = 0.0321(6)$ is in perfect agreement with the result deduced from the Mikhailov plot formalism. Finally, the spin-independent mixing amplitude $\epsilon_{\Delta K=\pm 2}$ between the γ-vibrational and ground-state bands is obtained from the slope parameter M_2 and the intrinsic quadrupole moment Q_0 via [Eqs. (4-211) and (4-232) of [4]]

$$\epsilon_{\Delta K=\pm 2} = \sqrt{\frac{8\pi}{15}}\frac{M_2}{eQ_0}.$$

In order to obtain the full mixing matrix element between the $J = 2$ states of both bands, the spin-dependence [Eqs. (4-199) and (4-233) ibid.] as well as their relative energy are taken into account. This yields

$$V_{\text{mix}} = \epsilon_{\Delta K=\pm 2}\sqrt{2(J-1)J(J+1)(J+2)}\,[E(J_\gamma) - E(J_1)] = 3.35^{+0.25}_{-0.27}\,\text{keV}$$

for $J = 2$. The matrix element is approximately half as large as the one obtained for first-order Coriolis mixing. However, the exploration of the exact interrelation between first- and second-order effects is not trivial, if feasible at all. The Coriolis interaction is an interaction between the rotational and intrinsic, i.e. single-particle, motion. Its properties are therefore intimately linked to the underlying microscopic structure.[114] Since collective excitations, such as the γ vibration [328] or the scissors mode [329, 330], are commonly modeled by linear combinations of multiple single-particle configurations, their individual $\Delta K = \pm 1$ Coriolis matrix elements eventually contribute to the overall $\Delta K = \pm 2$ mixing. Hence, first- and second-order Coriolis mixing can potentially only be related to each other if the same matrix elements dominate both expressions. From these considerations it must be concluded that there is no simple functional relationship between the two.

[114] For instance, this manifestes itself in a dependence of the decoupling parameter [Eq. (5-46) of [4]] on single-particle configurations of the involved rotational bands. In the $150 < A < 190$ mass region, these are approximately equal for identical single-particle configurations but vary considerably if the underlying structure changes [Tab. (5-16) ibid.].

Last but not least, it should be mentioned that the results from the Mikhailov plot provide a test for the nature of the $K^\pi = 2^+$ excitation of ^{164}Dy. It can either be interpreted as a vibrational excitation around an axially-symmetric equilibrium or as a rotational excitation of a body with rigid triaxial deformation. If the nuclear shape deviates slightly from axial symmetry, intrinsic quadrupole moments can be defined with respect to the unequal minor axes [Eq. (4-245) of [4]]; Q_0 still denotes the intrinsic quadrupole moment associated with an axially-symmetric nucleus, whereas Q_2 is interpreted as a measure for the asymmetry. While Q_0 is known experimentally [309], the latter moment is determined from the Mikhailov parameter M_1 [Eq. (4-247) of [4]]. The triaxial deformation parameter γ is then obtained from the ratio of Q_2 and Q_0, i.e. [Eq. (4-246) ibid.]

$$\tan\gamma = \sqrt{2}\,\frac{Q_2}{Q_0} = \sqrt{4\pi}e^{-1}\,\frac{M_1}{Q_0}.$$

This yields a deformation $\gamma = 9.1(7)^\circ$ for ^{164}Dy, which is more substantial than some estimates found in literature (e.g. $\gamma \approx 0.8^\circ$ [313] or $\gamma \approx 3^\circ$ [331, 332]). In fact, it is somewhat close to $\gamma = 12.3^\circ$[115] obtained from the energy ratio $E(2^+_\gamma)/E(2^+_1)$ in the asymmetric rotor model of Davydov, Filippov, and Chaban [334–336]. While small values of γ are found for many predominantly quadrupole-deformed nuclei [Tab. 6.11 of [44]], there is, apart from some candidates in the germaniums [337–339], virtually no firm evidence for pronounced rigid triaxiality.[116] Axial asymmetry is instead most likely associated with γ-soft behavior [121]. These different paradigms are empirically distinguished by their predictions for the staggering of the γ-vibrational band [44, 341, 342]. In the case of ^{164}Dy, it is only weakly developed[117] and, thus, testifies a predominantly axially-symmetric character and the presence of small rotation-vibration coupling.

[115] The uncertainty for γ is negligible since the energies are known precisely. If, on the other hand, γ is adapted to the ratio of transition strengths $B(E2;2^+_2 \to 2^+_1)/B(E2;2^+_2 \to 0^+_1)$ [333], a triaxial deformation parameter $\gamma = 9.2(-2.6)(+2.0)^\circ$ is obtained, which is in perfect agreement with the result from the Mikhailov formalism. That is plausible since both approaches are – in the present case – based upon transitions between the 2^+_γ state and the ground-state band. In general, however, the Mikhailov plot gives a value averaged over all considered transitions.

[116] Recent triaxial beyond-mean-field calculations indicate that superheavy ^{284}Cn with $\gamma \approx 20^\circ$ might be one of the best candidates for rigid triaxiality [340].

[117] The staggering factor is defined as $S(4) = \{[E(4^+_\gamma) - E(3^+_\gamma)] - [E(3^+_\gamma) - E(2^+_\gamma)]\}/E(2^+_1)$ [342]. For ^{164}Dy a value $S(4) \approx 0.29$ is obtained. This is close to the analytical result $1/3$ for the symmetric rotor whereas -2 is expected for the γ-unstable rotor.

6.1.3. Transitions to the 2^+_γ state

As outlined in Section 5.3, a transition between the 1^+_3 and 2^+_γ states of ^{164}Dy is established from the analysis of $\gamma\gamma$ coincidences [cf. panel (d) of Fig. 5.4]. Hitherto, it has been interpreted [261] as the coupling between the $K = 1$ scissors mode and the $K = 2$ γ-vibrational band. This decay was previously experimentally observed for soft nearly spherical nuclei [103, 156, 157, 343–345] and is allowed in both the Q-phonon scheme [220, 221, 346] and the IBM-2. Using the F-spin limit [59] of the latter's SU(3) dynamical symmetry, the analytical expression[118]

$$\frac{B(M1;1^+ \to 2^+_\gamma)}{B(M1;1^+ \to 0^+_1)} = \frac{3(N-2)(4N^2-1)}{N(2N-3)(4N^2-8N+1)},$$

which is a function of solely the total boson number N, is obtained for the $M1$ branching ratio. This yields expected values of 0.11 and 0.10 for ^{162,164}Dy, respectively. While this agrees to some extent with the determined branching ratio for the 1^+_3 state (cf. Tab. 5.3), no transitions to the 2^+_γ state are observed for the 1^+_1 state of ^{164}Dy as well as the investigated scissors-mode states of ^{162}Dy (cf. Section 5.2). Further experiments [19, 24, 92, 216, 230] actually suggest that the $M1$ matrix element connecting scissors-mode and γ-vibrational states is minuscule for deformed and transitional nuclei. Thus, the observed $1^+_3 \to 2^+_\gamma$ transition is most likely not attributed to the scissors mode, i.e. the $K = 1$ component of the initial dipole state.

This assumption is further corroborated by the results of the K mixing analysis (cf. Section 6.1.1). If the transitions were of $\Delta K = 1$ nature, a stronger transition to γ-vibrational states would be expected from the 1^+_2 state with 60% $K = 1$ component in the wave function [cf. Eqs. (6.1) and (6.2)] than from the 1^+_3 state with only 40%. Since this is in contradiction to the data (cf. Tab. 5.3), transitions to the γ-vibrational band are tentatively attributed to the $K = 0$ contribution of the states' wave functions. This implies a stronger transition to the 2^+_γ state from the 1^+_3 state which is characterized by a 60% $K = 0$ component. By virtue of the standard K selection rules [Sec. 4-3d

[118] This corresponds to a $1/N$ dependence of the branching ratio on the total boson number N. In the limit of infinite boson number ($N \to \infty$) transitions between the scissors mode and the γ band are forbidden. The nonzero value for the branching ratio is a consequence of the finite size of the quantum system (cf. Section 2.3.3).

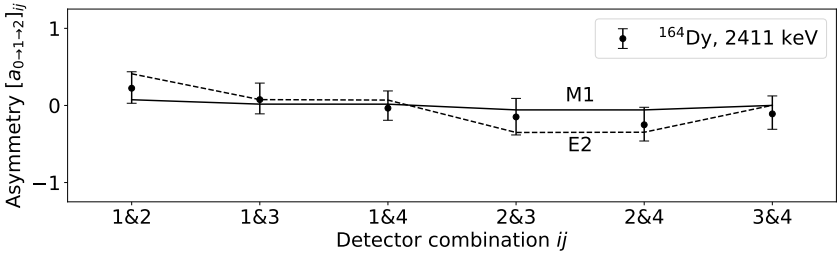

Figure 6.3.: Comparison of experimental asymmetries [cf. Eq. (4.2)] to analyzing powers [cf. Eq. (4.3)] for the $1_3^+ \to 2_\gamma^+$ transition of ^{164}Dy at 2.411 MeV. The data is consistent with both $M1$ (solid line) and $E2$ (dashed line) radiation character.

of [4]], the $1^+_{K=0} \to 2^+_\gamma$ transition must be of $E2$ character.[119] As shown in Fig. 6.3, this assignment is consistent with the observed asymmetries (cf. Section 4.3.1) even though $M1$ radiation cannot be excluded. Assuming pure $E2$ character, a reduced transition probability $B(E2; 1^+_3 \to 2^+_\gamma) = 1.96^{+0.32}_{-0.30}$ W.u. is obtained from the determined $M1$ branching ratio and the excitation strength of the 1^+_3 state [261]. This is comparable to typical $E2$ transition strengths between $K = 0$ and $K = 2$ bands of ^{164}Dy [188]. Ultimately, a future precision measurement of experimental asymmetries is crucial for the establishment of predominant $E2$ character in the $1^+_{2,3} \to 2^+_\gamma$ transition.

The transition to the γ vibration might serve as a distinguishing feature for the experimental investigation of states with negative $\mathscr{R}$ symmetry. With regard to NRF experiments only the observation of a $J^\pi = 1^+$ state is discussed.[120] For a pure $K = 0$ nature, a minuscule $M1$ excitation strength [cf. Eq. (6.3)] and an Alaga-compliant

[119] Invoking Eq. (4-92) of Ref. [4], the matrix element $\langle K_f \neq 0, J_f \| \boldsymbol{T}(\sigma\lambda) \| K_x = 0, J_x \rangle$ is proportional to the Clebsch-Gordan coefficient $\langle J_x 0 \lambda K_f | J_f K_f \rangle$. Thus, this matrix element vanishes if a transition with $|K_f - K_x| > \lambda$ [Eq. (4-93) ibid.] is considered, i.e. the component of angular momentum along the intrinsic symmetry axis cannot be conserved. This criterion is clearly fulfilled for an $M1$ transition between states with $K = 0$ and $K = 2$. Hence, solely the $1^+_{K=0} \to 2^+_\gamma$ $M1$ transition is singly K forbidden but not the corresponding $E2$ transition.

[120] Of course it is assumed that the nucleus is sufficiently quadrupole deformed (cf. Section 2.1.2).

branching ratio to the 2_1^+ state of two are expected. If in the other hand $K = 0$ and $K = 1$ excitations are mixed, the situation discussed in Sections 2.2 and 6.1.1 is obtained. This requires the experimental observation of two 1^+ states with branching ratios oppositely deviating from the Alaga predictions for $K = 1$ excitations.[121] In the case of weak mixing, an appreciable $E2$ transition to the 2_γ^+ state is expected for a single state, which is subsequently assigned predominant $K = 0$ character. For strong mixing comparable branching transitions are expected. The identification of these might require coincidence-capable detection setups.

Dipole states with branching ratios suggesting K mixing have been identified for several rare-earth nuclei [Tab. 1 of [306]]. However, it must be considered that a deviating decay behavior can also be an indication of a doublet (cf. Section 4.3.3). Incorporating the newly proposed coupling to the γ-vibrational band, two 1^+ states of ^{164}Dy at 3316.8 and 3414.7 keV come into focus. They predominantly decay to the 2_γ^+ state and feature branching ratios to the 2_1^+ state which deviate from the Alaga prediction [261]. Ultimately, a dedicated investigation of such candidate states is direly needed.

[121] It is assumed that Z is of the order of 10 [cf. Eq. (6.2)] and that a certain amount of mixing is present. As shown in panel (a) of Fig 2.2, the expected signature is not valid for very little mixing.

6.2. $\Delta F = 1$ $E2$ strength of the scissors mode across the $N = 90$ QPT

The scissors mode's gross properties such as its mean excitation energy and the salient $M1$ excitation strength have in the past been, as outlined in Section 2.4, studied extensively [148, 150, 161]. At the latest with the study of the relationship between $M1$ strength and nuclear deformation [152, 163], the scissors mode has been linked to the phase transition (cf. Section 2.5.3). After the turn of the millennium, the focus also shifted to the study of individual decay channels and their significance for shape isomerism [215] and shape evolution [19, 216]. Only with the results of the present work this connection can also be made for the $E2$ properties of the scissors mode. Once again, gadolinium isotopes have been given a pioneering role in this context.

6.2.1. Systematics of the scissors mode in gadolinium isotopes

The stable even-even gadolinium isotopes are located across the $N = 90$ QPT ranging from vibrational ^{152}Gd via transitional ^{154}Gd to rotational ^{156,158,160}Gd. Primarily from electron and photon scattering, their low-lying dipole strength is known. Hence, they are a perfectly suitable testing ground for the study of the scissors mode's evolution with nuclear shape. Panel (a) of Fig. 6.4 exemplarily shows the summed $M1$ strength between 2.7 and 3.7 MeV as a function of the P-factor [173, 176]. It exhibits a monotonous increase with deformation saturating towards midshell; this is similar to other fingerprint observables such as the $R_{4/2}$ ratio [cf. panel (a) of Fig. 2.3] or the $B(E2; 2_1^+ \rightarrow 0_1^+)$ transition strength shown in panel (c). The correlation between the latter and the low-lying $M1$ strength is depicted in panel (b) of Fig. 6.4 alongside the empirical relation[122] [161]

$$\sum\nolimits_i B(M1; 1_i^+ \rightarrow 0_1^+) = \frac{10.6}{Z^2} B(E2; 2_1^+ \rightarrow 0_1^+). \tag{6.7}$$

Given its simplicity the agreement with data is good, especially since outliers can be explained. The NRF experiment off ^{152}Gd suffered from a low isotopic enrichment

[122] For dimension purposes, both transition strengths are given in units of single-particle estimates [Eq. (3C-38) of [28]]. In Fig. 6.4, however, the summed $M1$ strength is given in units of squared nuclear magnetons. Although the conversion to and from single-particle units is usually dependent on the mass number A, the relevant factor is constant for all values of A in the case of $M1$ radiation.

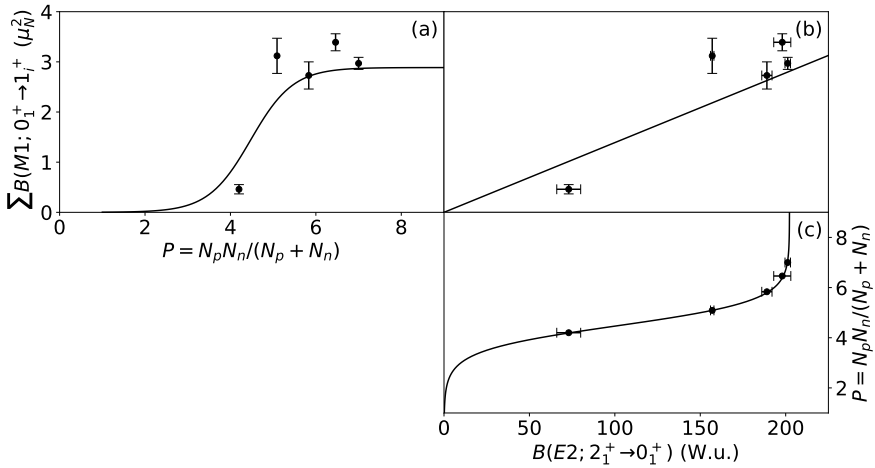

Figure 6.4.: Systematics of the summed $M1$ strength associated with the scissors mode for even-even stable gadolinium isotopes. Data for ^{152,154}Gd and ^{156,158,160}Gd are taken from Refs. [19] and [161], respectively. Panel (a) depicts the evolution of the summed $B(M1; 1_i^+ \rightarrow 0_1^+)$ strength with the P-factor. A scaled phenomenological logistic function, which is adapted to the evolution of the $B(E2; 2_1^+ \rightarrow 0_1^+)$ strength shown in panel (c), is indicated by the solid line. It has the sole purpose of guiding the eye across the $N = 90$ QPT. The correlation between the low-lying $M1$ and $E2$ strength is shown in panel (b) together with the empirical relation from Ref. [161] for $Z = 64$ [cf. Eq. (6.7)].

of only 32.47(30)% [19]. The quoted $M1$ strength represents a lower limit because further scissors-mode states might have remained undetected. Noticeable is also the enhanced value for ^{158}Gd in contrast to the neighboring ^{156,160}Gd which all share a comparable structure.[123] For the latter two nuclei parities are known from the usage of polarized photons in the entrance channel [19, 24, 281] and Compton polarimetry [292]. For the dipole states of ^{158}Gd, on the other hand, this information

[123] Indicators are, for instance, similar $R_{4/2}$ ratios or nuclear deformation parameters.

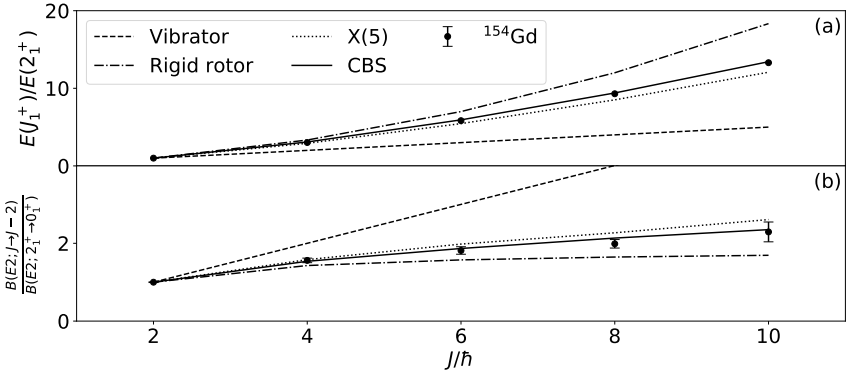

Figure 6.5.: Comparison of experimental data with theoretical predictions from the vibrator (dashed), X(5) (dotted), CBS (solid), and rigid-rotor (dash-dotted) models for relative energies [panel (a)] and transition strengths [panel (b)] in the ground-state band of ^{154}Gd. The small deviations from the X(5) predictions place ^{154}Gd just past the critical point towards the rigid-rotor limit. Data are taken from Ref. [184].

is missing [295], resulting in a potentially overestimated $M1$ strength. Furthermore, the large summed $M1$ strength of ^{154}Gd stands out. It is comparable to the deformed gadolinium nuclei and, thus, would suggest that also ^{154}Gd is located on the deformed side of the QPT. However, basically all other observables favor a placement near the critical point. Figure 6.5 shows the evolution of relative yrast energies [panel (a)] and intraband transition strengths [panel (b)] with angular momentum. The experimental data lies between the vibrator and rigid-rotor limits, fairly close to the predictions of the X(5) critical point symmetry [347]. In fact, the small deviations place it slightly towards the rotational limit [348], just past the critical point. Using the confined β-soft rotor model [349], a small structural parameter $r_\beta = 0.19$ is needed to describe the ground-state band. This placement is comparable to the other $N = 90$ isotones ^{150}Nd [350, 351] and ^{152}Sm [349, 352].[124] A plausible origin of this ambiguity is

[124]For ^{156}Dy, the situation is more complicated. Transition strengths in the ground-state band deviate significantly from the X(5) prediction [353], whereas better agreement is found for the first excited $K^\pi = 0^+$ band [354]. In this context, the potential influence of the γ degree of freedom is highlighted.

rooted in the scissors mode's fragmentation. It is large for ^{156,158,160}Gd, potentially resulting in an underestimated value for the summed $M1$ strength, especially in combination with the restricted excitation-energy region. For ^{154}Gd, on the other hand, the scissors-mode strength is concentrated in just a few states. To make matters worse, the 1^+ state at 3090.6 keV forms a doublet with an $^1/_2{}^+ \rightarrow {}^1/_2{}^-$ transition of ^{13}C. Hence, the $M1$ excitation strength obtained from photon scattering [19] represents only an upper limit.[125] Ultimately, further precision experiments can complete the picture.

6.2.2. Implications of $\Delta F = 1$ $E2$ strength in the IBM-2

The most prominent hallmark of scissors-mode states is their collective $M1$ nature. Access to this observable is granted through a straightforward measurement of excitation cross sections of positive-parity dipole states. Experimental information on the elusive $E2$ properties, on the other hand, can be obtained from precision measurements of the $1^+_{\mathrm{sc}} \rightarrow 2^+_1$ transition's multipole-mixing ratio. Technically, the partial transition widths which correspond to $M1$ and $E2$ radiation are given by (cf. Section 3.1)

$$\Gamma_{1\rightarrow 2,M1} = \frac{1}{1+\delta^2_{1\rightarrow 2}}\Gamma_{1\rightarrow 2} \qquad \text{and} \qquad \Gamma_{1\rightarrow 2,E2} = \frac{\delta^2_{1\rightarrow 2}}{1+\delta^2_{1\rightarrow 2}}\Gamma_{1\rightarrow 2},$$

respectively. Since $\Gamma_{1\rightarrow 2}$ can be inferred from the branching ratio and the excitation strength of the scissors-mode state in question, the resulting reduced transition strengths $B(E2; 1^+_{\mathrm{sc}} \rightarrow 2^+_1)$ are obtained. In Tab. 6.1, a compilation of available data in vicinity of the $N = 90$ QPT is given. Due to their dependence on the squared difference of the quadrupole boson charges, such $E2$ transitions with $\Delta F = 1$ individually fix the values for e_π and e_ν in the IBM-2.

Starting from the IBM-1 Hamiltonian of Eq. (2.17), a reproduction of the low-energy nuclear structure is attempted. Employing the extended consistent-Q formalism [93–95], the same quadrupole operator is used in the Hamiltonian and the $E2$ transition operator. Hence, along with ζ the absolute magnitude of χ, i.e. the degree of axial asymmetry, is inferred from the experimental level scheme. In practice, contours

[125] From the (γ,γ') measurement $B(M1; 1^+ \rightarrow 0^+_1) = 0.38(8)\,\mu_N^2$ is reported [19] in contrast to a value of $B(M1; 1^+ \rightarrow 0^+_1) \approx 0.2\,\mu_N^2$ from the (e,e') experiment [Fig. 3 of [253]]. In view of the differing excitation strengths for the 1^+ state at 2934.2(6) keV (cf. Section 5.1), no correction of the summed $M1$ excitation strength is attempted here.

Table 6.1.: Compilation of experimental data on $\Delta F = 1$ $E2$ strength in the vicinity of the $N = 90$ QPT. Results on ^{154}Gd and ^{162,164}Dy are obtained in the present work, whereas $B(E2; 1^+_{sc} \rightarrow 2^+_1)$ transition strengths of ^{152}Sm and ^{156}Gd are found in Refs. [230] and [24], respectively.

Nucleus	$E_x(1^+_{sc})$ (keV)	$\Gamma_{1\rightarrow 2,E2}$ (meV)	$B(E2; 1^+_{sc} \rightarrow 2^+_1)$ (W.u.)
^{152}Sm[a]	2930.6(4)		≤ 0.058
	2991.6(4)		$0.125^{+0.176}_{-0.079}$
	3025.3(4)		$1.121^{+0.394}_{-0.519}$
^{154}Gd	2934.2(6)	$1.25^{+0.53}_{-0.42}$	$0.181^{+0.076}_{-0.061}$
^{156}Gd[b]	3070		0.037(26)
^{162}Dy	2900.0(3)	$0.01^{+0.43}_{-0.01}$	$0.001^{+0.058}_{-0.001}$
	3061.2(3)	$0.006^{+0.226}_{-0.006}$	$0.0006^{+0.0229}_{-0.0006}$
^{164}Dy	3111.2(3)	$0.05^{+1.65}_{-0.05}$	$0.004^{+0.149}_{-0.004}$
	3159.1(3)	$0.51^{+0.84}_{-0.51}$	$0.043^{+0.070}_{-0.043}$
	3173.6(3)	$0.006^{+0.258}_{-0.006}$	$0.0005^{+0.0211}_{-0.0005}$

[a] From Ref. [230].
[b] From Ref. [24].

of observables are evaluated in the parameter space of the IBM-1. Their crossings pinpoint the appropriate values of the Hamiltonian parameters [355]. Especially the fundamental $R_{4/2}$, $R_{\gamma/2} = E(2^+_\gamma)/E(2^+_1)$, and $R_{0/2} = E(0^+_2)/E(2^+_1)$ ratios are sensitive indicators of axially-symmetric deformation and, thus, of the parameter ζ. Their evolution illustrates the transition from the U(5) phonon structure to intrinsic excitations in SU(3) and O(5)-like excitations in O(6) [Fig. 1 ibid.]. However, these contours are not particularly sensitive to χ. This requires a signature which, for instance, incorporates energy differences of distinct intrinsic excitations such as the (quasi-) β and γ bands. In the phonon picture, the 0^+_2 and 2^+_2 states are both two-phonon excitations and, thus, degenerate. For SU(3) [O(6)], on the other hand, the 0^+_2 state is lower (higher) in energy than the 2^+_γ state.[126] A suitable contour of this type is

[126] Typical spectra for illustration are given by Figs. 2.1., 2.2., and 2.3. of Ref. [13].

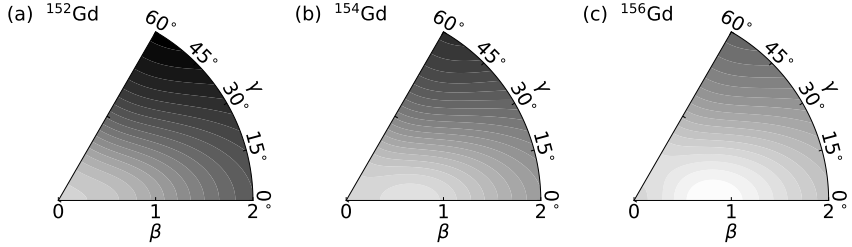

Figure 6.6.: Potential energy surfaces [cf. Eq.(2.18)] obtained from the IBM-1 Hamiltonian (2.17) for ^{152}Gd [panel (a)], ^{154}Gd [panel (b)], and ^{156}Gd [panel (c)]. They reflect the evolution across the $N = 90$ QPT in terms of incipient axially-symmetric deformation along with increasing γ-softness. The latter manifests itself in an extension of the potential minimum towards $\gamma > 0°$. The color code ranges from white (small) to black (large) and is shared among all panels.

given by $R_{0\gamma} = [E(0_2^+) - E(2_\gamma^+)]/E(2_1^+)$ [355].[127] Starting from available parameter sets [358] and employing an iterative approach, the description of the low-energy level scheme can subsequently be improved with respect to the above signatures. Resulting IBM-1 potential energy surfaces [cf. Eq. (2.18)] are depicted in Fig. 6.6 for the nuclei ^{152,154,156}Gd. Their evolution across the $N = 90$ QPT is governed by two discernible patterns. As expected, the potential minimum moves towards larger deformation parameters β. In addition, the degree of γ-softness increases with mass. While ^{152}Gd is γ-stiff ($\chi = -1.323$), ^{156}Gd ($\chi = -0.898$) already exhibits a broadened potential minimum allowing $\gamma > 0°$. This trend continues for heavier gadolinium isotopes and is also found in dysprosium and erbium chains [Fig. 14 of [358]].[128]

[127] An alternative observable is given by $R_{02} = E(0_2^+)/[E(2_\gamma^+) - E(2_1^+)]$ [95, 356, 357]. However, the obtained contours around $\zeta \approx 0.5$ are similar to, for example, the $R_{4/2}$ ratio [Fig. 3 of [355]].

[128] An alternative method for the determination of Hamiltonian parameters is the mapping from a microscopically calculated potential energy surface [359]. Due to its microscopic foundation, this procedure is applied to the IBM-2. Studies of the $N = 90$ QPT revealed a qualitative agreement with the experimental data [360] but tend to overestimate energies of off-yrast states [361, 362]. Potentially due to the larger number of degrees of freedom in the IBM-2, no increase in γ-softness is discernible from the mapped χ_π and χ_ν values.

These considerations show that prematurely selecting $\chi = -\sqrt{7}/2$ might cut a relevant part of the physics incorporated in the IBM. Instead, the excitation energies of the (quasi-) β and γ bands deserve special attention.

The obtained parameters are subsequently used for IBM-2 calculations, which employ the Hamiltonian given in Eq. (2.16) along with the $M1$ and $E2$ operators of Eqs. (2.13) and (2.15), respectively. By virtue of the Hamiltonian's F-spin symmetry, all states have good F-spin quantum numbers and, thus, incorporation of the Majorana operator does not affect the level scheme of symmetric states. Its parameters ξ_i, $i \in \{1,2,3\}$, are adapted to properties of a proxy state which resides at the excitation strength-weighted energy [cf. Eq. (2.20)] of all experimentally observed scissors-mode states and carries their summed $M1$ and $E2$ strength. If only information on the $M1$ transitions between the scissors mode and the ground-state band are available, which is the case for ^{162,164}Dy,[129] all Majorana parameters ξ_i are chosen equal. For ^{154,156}Gd, on the other hand, information on transitions between the scissors mode and other intrinsic excitation modes is available [19]. In the spirit of Ref. [92], additional calculations are performed selecting $\xi_1 = \xi_3$ and ξ_2 independently. Details on the IBM-2 calculations are collected in Appendix B.

With respect to one of the introductory questions (cf. Section 1), the comparison of both parameter choices provides significant insight. In the case of the transitional nucleus ^{154}Gd, the mixed-symmetric 2^+ state is found below the scissors mode for both sets of Majorana parameters (cf. Tab. B.2). For axially-deformed ^{156}Gd, on the other hand, the emergence of a scissors-mode rotational band is expected [14]. It becomes evident from Tab. B.4, that this is only the case if all ξ_i are equal. If the reproduction of the $B(M1; 1^+_{\text{sc}} \rightarrow 0^+_2)$ value is imposed as an additional constraint, the comparatively small value of the ξ_2 parameter (cf. Tab. B.3) forces the mixed-symmetric 2^+ state to lower excitation energies. This effect is shown in Fig. 6.7 from schematic calculations in the IBM-2. From a naive perspective, two potential conclusions can be drawn; either the scissors mode does not (yet) form a rotational band for ^{156}Gd or a determination of Majorana parameters solely based upon transitions of the 1^+_{sc} state is not viable. The first option is unlikely given the well-developed rotational bands which emerge from other intrinsic excitations of ^{156}Gd [79]. In fact, an approximately nine times larger $M1$ transition strength between the scissors mode and the 0^+_β state, which is especially

[129] The transition to the 2^+_γ state, which is observed for the 1^+_3 state of ^{164}Dy (cf. Tab. 5.3), is not considered while selecting the Majorana parameters. As outlined in Section 6.1.3, it is attributed to the $K = 0$ components in the wave functions of the mixed 1^+_2 and 1^+_3 states.

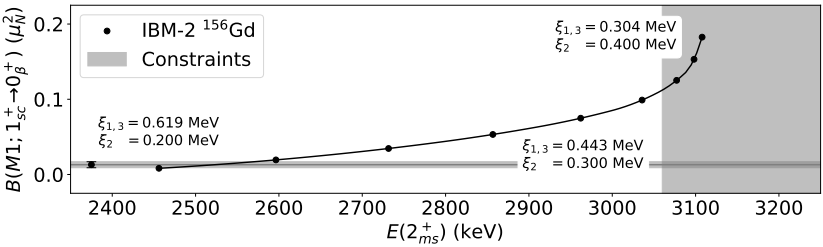

Figure 6.7.: Mutual dependence of the excitation energy of the mixed-symmetric 2^+ state and the $B(M1; 1^+_{\text{sc}} \rightarrow 0^+_\beta)$ transition strength on the Majorana parameter ξ_2 in the IBM-2. While the Hamiltonian parameters ϵ, κ, and χ are constant for all calculations and take the values collected in Tab. B.3, the Majorana parameters $\xi_1 = \xi_3$ and the boson g factor g_π are required to reproduce the excitation energy and $M1$ strength of the scissors mode. The results of the IBM-2 calculations, which were performed for nine equidistant values $\xi_2 \in [0.2, 0.4]$, are depicted by black dots together with an interpolation. The available experimental constraint for the $B(M1; 1^+_{\text{sc}} \rightarrow 0^+_\beta)$ value of ^{156}Gd is indicated by the horizontal gray line. The gray area highlights the allowed energy range for the 2^+_{sc} state if the formation of a rotational band is requested.

sensitive to the Majorana parameter ξ_2 [92], is needed for a restoration of the scissors mode's rotational band. Since the microscopic structure of initial and final states might play an important role in the magnitude of transitions, a critical evaluation of the conjectured 0^+_β state is in order. Indeed, the β-vibrational nature of the 0^+_2 state of ^{156}Gd, which is located at 1049.487(2) keV, is under discussion [363, 364].[130] Impurities in its wave function, which are beyond the model space of the IBM, might significantly alter the $M1$ matrix element. Conversely, also experimentally observed scissors-mode states are not necessarily pure mixed-symmetry states as obtained in the

[130] Criteria are, for instance, the compliance of its transitions to the ground-state band with the Alaga predictions [46] or $\rho^2(E0)$ values to the ground state [363]. In contrast, an investigation in terms of the SU(3) (partial) dynamical symmetry supports the interpretation of the fist excited $K^\pi = 0^+$ band as the β band [365].

IBM-2. The mechanism which causes the scissors mode's fragmentation might proceed through mixing of the collective mode with weakly-excited microscopic states [211]. As evident from Sections 2.2 and 6.1, such mixing can trigger a stark change in decay properties. Depending on the nature of this microscopic background, the simple extrapolation of the decay properties to all states is not necessarily correct. The investigation of a larger sample of scissors-mode states is inevitable to study the fragmentation process. Ultimately, it seems more purposeful to experimentally establish the 2^+_{sc} state and, thus, fix ξ_2 by its excitation energy. A combination of both approaches enables the study of the influence of microscopic configurations on the gross properties of the scissors mode.

The absolute strength of $M1$ transitions in IBM-2 calculations is scaled by the boson g factors g_π and g_ν. Microscopic considerations indicate that for vibrational nuclei g_ν is approximately zero whereas g_π is on the order of one [366, 367]. Hitherto, data-driven strategies to choose their appropriate values came in two different ways. Either, they were adapted to experimental g factors of the 2^+_1 state [368] assuming constancy [369, 370] or were adjusted to collective $M1$ transitions of mixed-symmetry states. In principle, the latter approach yields local values, which enable the consideration of the underlying microscopic structure. The $M1$ transition strengths are proportional to the factor $(g_\nu - g_\pi)^2$ [59] and, thus, sensitive to the relative magnitude of the boson g factors. However, their absolute values cannot be fixed from transitions alone due to the absence of 1^+ states with maximum F-spin. In practice, g_ν is commonly put to zero and g_π is adjusted such that, for instance, the excitation strength of the scissors mode is exactly reproduced. Combining both strategies, the vast experimental information on magnetic moments (or equivalently g factors) [371] enables a determination of local values for the boson g factors also for deformed nuclei. For any F-spin invariant Hamiltonian, the magnetic moment of the 2^+_1 state is given by [Sec. 5.5.1 of [13]]

$$\mu(2^+_1) = (g_\pi N_\pi + g_\nu N_\nu)\frac{2}{N}, \tag{6.8}$$

irrespective of a dynamical symmetry [59]. The obtained values deviate from free orbital g factors;[131] noteworthy are negative values for g_ν (cf. Tabs. B.1, B.3, B.5, and

[131] At least, boson-mapping techniques suggest an approximate translation from free orbital to boson g factors [367, 372]. Other approaches, which focus on the description of $g(2^+_1)$ systematics in the rare-earth region, drop the requirement of F-spin symmetry for the Hamiltonian [367, 372, 373] or employ concepts such as effective boson numbers to account for subshell closures [369, 370].

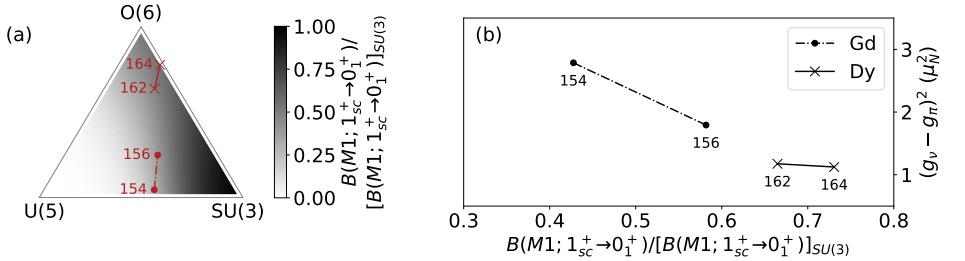

Figure 6.8.: Interplay of structural evolution and relative magnitude of boson g factors. The schematic calculations presented in panel (a) feature boson numbers $N_\pi = N_\nu = 2$ and Majorana parameters $\xi_i = 0.5$, $i \in \{1,2,3\}$. For a placement in the IBM symmetry triangle, the conversion of Hamiltonian parameters ϵ, κ, and χ to polar coordinates of Ref. [200] is employed. Depending on the position of the nuclei, which is indicated in red, different values for the $B(M1;1^+_{sc}\to0^+_1)$ strength relative to the SU(3) systematic are obtained. Since ratios of $M1$ transition strengths are discussed, they are independent of g_π and g_ν. For comparable values of the scissors mode's summed $M1$ excitation strength, as found for ^{154,156}Gd and ^{162,164}Dy, the boson g factors are enhanced to compensate this effect. This results in an inverse proportionality as evident from panel (b).

B.7 of Appendix B). Their occurrence can be explained with rather simple considerations. For given boson numbers N_ρ and g factors g_ρ, $\rho \in \{\pi, \nu\}$, the maximum possible $M1$ excitation strength of the scissors mode is found in the SU(3) limit. Panel (a) of Fig. 6.8 exemplarily illustrates the evolution of the $B(M1;1^+_{sc}\to0^+_1)$ strength in the symmetry triangle of the IBM relative to the SU(3) systematic given in Eq. (2.19).[132] Since roughly comparable summed $M1$ strengths are found for the considered nuclei [cf. panel (b) of Fig. 2.6 and panel (a) of Fig. 6.4], the decreasing intrinsic[133] strength must be counterbalanced by the boson charges. This effect is highlighted in panel (b) of Fig. 6.8. The upper limit on the modified sum of g_π and g_ν, which is obtained

[132] To be specific, Eq. (2.19) must be divided by three since depopulating $M1$ transitions are considered.

[133] In this context, intrinsic strength denotes the part of the transition strength which is independent of the choice of boson g factors. Panel (a) of Fig. 6.8 shows that differences in the $M1$ excitation strength of the scissors mode arise from the placement of the considered nucleus in the IBM symmetry triangle.

from the magnetic moment [cf. Eq. (6.8)], forces the occurrence of negative boson g factors. This raises the question of whether the complete $M1$ strength considered can be attributed to the scissors mode. In fact, also two-quasiparticle strength can be found in the energy region of interest [312, 374] and the states might have, for example, not negligible spin contributions [299, 313].[134]

The knowledge of at least one $\Delta F = 1$ $E2$ transition strength enables the determination of the quadrupole boson charges e_π and e_ν. Currently, their experimental investigation is limited to strongly excited scissors-mode fragments (cf. Tab. 6.1). The obtained $B(E2; 1^+_{sc} \rightarrow 2^+_1)$ value is scaled to account for remaining states assuming an equal distribution of $M1$ and $E2$ strength among all fragments. For ^{156}Gd, e_π and e_ν have already been determined in the F-spin limit of the SU(3) dynamical symmetry [24]. Respecting the deviation of ^{156}Gd from SU(3) [cf. panel (c) of Fig. 6.6], the reduction in χ must be compensated by the quadrupole boson charges. Hence, the values given in Ref. [24] change to $e_\pi = 0.148$ and $e_\nu = 0.134$ eb. This corresponds to the expected increase of the factor $(e_\pi N_\pi + e_\nu N_\nu)$ for transitions between states with maximum F-spin and simultaneously an assimilation of the individual charges.

The available experimental information on quadrupole boson charges is depicted in panel (a) of Fig. 6.9, showing the evolution of scalar and vector charges with the P-factor. For vibrational ^{148}Sm, the individual charges are small and vary considerably. On the deformed side of the QPT, their sum remains rather constant due to the saturating $E2$ collectivity [cf. panel (b) of Fig. 2.3]. The difference of e_π and e_ν, on the other hand, is small, testifying the dominance of quadrupole-quadrupole interactions. From charges alone, the phase transition is better mapped by their sum, for which no information on $\Delta F = 1$ $E2$ transitions is needed. Conversely, products of the latter with $\Delta F = 0$ $E2$ transition strengths classify as signatures for the QPT. As evident from panels (b) and (c) of Fig. 6.9, both peak, as motivated in Section 2.5.3, at $P \approx 5$. For ^{164}Dy, an enhancement is encountered in panel (b). It is, however, spurious since no uncertainties are assigned to IBM parameters. Considering the product of $E2$ strengths [panel (c)], which is entirely obtained from experiment, the values for ^{162,164}Dy agree with each other. This is reasonable since both exhibit a comparable structure.[135]

[134] As already mentioned several times, the summation limits for the $M1$ strength [150, 161] are chosen quite arbitrarily. Actually, each 1^+ state should be carefully examined and only orbital strength should be considered. The latter can be fulfilled by a comparison of data from, for instance, high resolution proton- and photon-scattering experiments.

[135] See footnote [123].

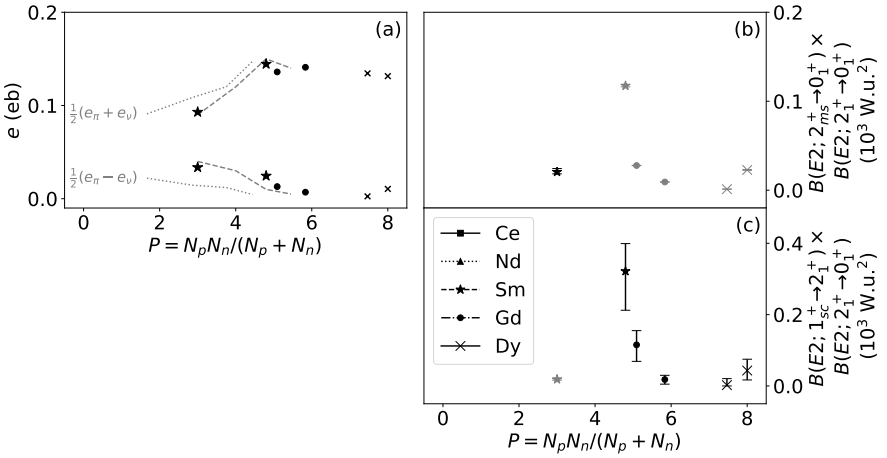

Figure 6.9.: Evolution of $E2$ quantities across the $N = 90$ QPT. Panel (a) depicts available data on scalar and vector quadrupole boson charges for samarium, gadolinium, and dysprosium isotopes along with predictions for the neodymium [226] and samarium [224] isotopic chains. Panels (b) and (c) show (semi-) experimental values for products of $\Delta F = 0$ and $\Delta F = 1$ $E2$ transition strengths. Predictions for the latter from the IBM-2 calculations, which employ the charges from panel (a), are identified by gray markers. Similar to the $M1$ signatures from panel (b) of Fig. 2.7, a maximum marks the QPT.

Even though the current data supports the manifestation of these novel signatures, additional information on $\Delta F = 1$ $E2$ transitions is needed. This concerns in particular the spherical side of the QPT, where results are only available for ^{148}Sm from identification of the 2^+_{ms} state [20]. On the contrary, vanishing multipole-mixing ratios were found for some investigated $1^+ \to 2^+_1$ transitions of ^{150}Sm [375] and ^{150}Nd [92]. At least as important is a test of the relative magnitudes of the $B(E2; 1^+_{\mathrm{sc}} \to 2^+_1)$ and $B(E2; 2^+_{\mathrm{ms}} \to 0^+_1)$ transition strengths obtained from the IBM-2. Currently, the evolu-

tion shown in panel (b) of Fig. 6.9 is almost exclusively relying on these predictions. This requires knowledge on both $E2$ transitions between fully- and mixed-symmetric states for the same nucleus. Promising candidates for such a test are the transitional nuclei with $N = 90$ since none of the two transitions in question vanishes.

The overall discussion on these potential new signatures relies heavily on the Interacting Boson Model. As introduced in Section 2.3, it is by construction a collective model, which employs a heavy truncation even of the shell-model space and features bosons instead of fermions as its most basic building blocks. Naturally, the model cannot respect subtleties which are rooted in the underlying shell structure; examples of which are subshell closures or fragmented collective modes. The higher the level of detail, the more these shortcomings become apparent. Ultimately, the IBM might no longer be the suitable model for these scenarios and a microscopic approach is needed instead. Previous calculations have shown that collective $M1$ strength can indeed be obtained from single-particle motion of nucleons [Sec. III.2.c. of [17]]. Hitherto, deformed rare-earth nuclei were mostly treated in terms of RPA and its derivatives. Due to computational limitations, shell-model calculations were available solely for light and medium-heavy nuclei.[136] The Monte-Carlo shell model enables the study of scissors-mode states [378] of deformed nuclei in the immediate future and places the above discussion on a microscopic footing.

6.2.3. Indications for states of the scissors mode's rotational band

The parameter values of the Majorana interaction remain, as emphasized in Section 6.2.2, one of the last enigmas of the IBM-2. Especially its influence on the excitation energy of the mixed-symmetric 2^+ state implies a straightforward possibility for the determination of ξ_2. However, experimental information on multiple mixed-symmetry states in a single nucleus is available only for vibrational ^{94}Mo [21, 22]. The combination of experiments and theoretical studies of the last four decades allows at least some conclusions also for transitional and deformed nuclei.

For transitional ^{154}Gd, which is the cornerstone nucleus of the evolution across the $N = 90$ QPT, a potential candidate for the mixed-symmetric 2^+ state might be found at 3000 keV (cf. Section 5.1). The asymmetries of its transition to the 2^+_1 state,

[136] For 2^+_{ms} states of spherical-vibrational nuclei, on the other hand, large-scale shell model calculations are available also in the rare-earth region [376, 377].

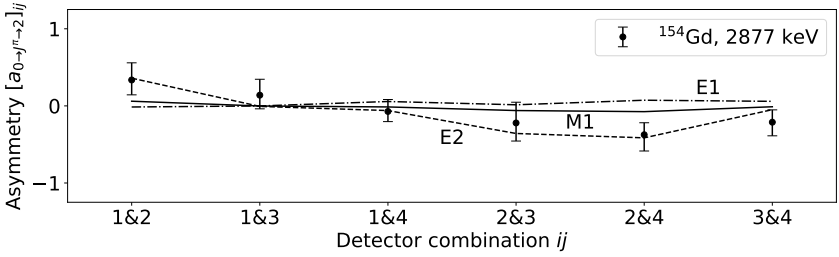

Figure 6.10.: Comparison of experimental asymmetries [cf. Eq. (4.2)] to analyzing powers [cf. Eq. (4.3)] for the $J^\pi \to 2_1^+$ transition of ^{154}Gd at 2877 keV. The data is consistent with a $2^+ \to 2_1^+$ assignment, while a $J = 1$ initial state cannot be excluded. A dedicated discussion is given in Section 5.1.

which are shown in Fig. 6.10, are consistent with this assignment while a $1^- \to 2_1^+$ transition cannot be excluded.[137] If this were indeed the 2_{sc}^+ state, a rotational-like configuration of the mixed-symmetry states would be present. A reanalysis of data from electron-capture reactions, which were used for the study of scissors-mode states of ^{152,154}Gd [19, 216], might yield firm assignments for angular momentum and parity quantum numbers of the initial state at 3000 keV based on its transition to the 2_1^+ state. Furthermore, an extraction of a small multipole-mixing ratio for the latter transition might enable the identification of mixed-symmetric 2^+ states, but without lifetime information.

Inelastic electron- and photon-scattering experiments off ^{156}Gd independently place a candidate for the 2_{sc}^+ state at 3089 keV[138] [23, 24]. Assuming that this represents the rotational excitation of the strongest scissors-mode fragment at 3070 keV, the corresponding moment of inertia ϑ can be obtained from rotational energies [Eqs. (4-61) and (4-62) of [4]]

$$E_{\mathrm{rot}}(K,J) = \frac{\hbar^2}{2\vartheta}\left[J(J+1) + \tilde{a}(-1)^{J+1}J(J+1)\delta(K,1)\right].$$

[137] See discussion in Section 5.1.

[138] From electron scattering, an excitation energy of 3096 keV is quoted [23]. However, also the energy of the most prominent scissors-mode state, which is found at 3070 keV [79], is reported 5 keV higher. Thus, it is likely that the states reported from electron and photon scattering do indeed coincide.

Table 6.2.: Comparison of experimental moments of inertia to predictions from the rigid rotor[139], the IBM-2, and the QPNM. The experimental value for ^{156}Gd is given relative to the 1^+_{sc} state at 3070 keV [24], whereas the IBM-2 employs proxy states as outlined in Section 6.2.2 and Appendix B. Details on the QPNM calculations are found in Ref. [379].

Nucleus	δ	Moment of inertia $2\vartheta_{sc}/\hbar^2$ (MeV^{-1})			
		Experiment	Rigid rotor	IBM-2	QPNM
^{156}Gd	0.271[a]	210.5	135.8	153.8	171.2[b]
^{162}Dy	0.274[a]		144.8	125.0	108.8[b]
^{164}Dy	0.278[a]		148.0	137.9	127.8[b]

[a] From Ref. [150].
[b] From Ref. [379].

Here, $\tilde{a}$ is the $K = 1$ decoupling parameter with signature $(-1)^{J+1}$. Since both the decoupling parameter and the moment of inertia are unknown, assumptions must be made in the presence of a single known rotational energy. Previously, comparable values of ϑ were expected for ground-state and scissors-mode rotational bands, leading to estimates for $\tilde{a}$ [24]. Studies in the QPNM, however, suggest that the scissors mode's moment of inertia can even exceed the rigid-body value (cf. Tab. 6.2) while the influence of decoupling is negligible [379]. In the case of ^{156}Gd, the deviation of the calculated moment of inertia from the experimental value is on the same order as for the 2^+_γ state.[140] Predictions for the moments of inertia can also be derived from the IBM-2 calculations with equal Majorana parameters (cf. Appendix B). In fact, the values deviate less than 15% from those obtained in the QPNM. This finding might be an indication that the individual parameters of the Majorana interaction should differ only slightly.

[139] The moment of inertia of a rigid rotor with axial symmetry is given by $\vartheta = (2/5)AMR^2(1 + \delta/3)$ [Eq. (4-104) of [4]], where $R = 1.2A^{1/3}$ fm denotes the nuclear radius and M is the atomic mass unit.

[140] To be precise, the calculated moments of inertia for the ground-state band systematically underestimate the experimental data while the trend is exactly opposite for the γ-vibrational band [379]. Still, a larger moment of inertia is rightly predicted for the latter and the calculations follow the experimental trend for several rare-earth nuclei.

As mentioned in Section 6.2.2, the structure of the scissors mode's rotational band can only be conclusively clarified by experimental identification of the 2^+_{sc} and 3^+_{sc} states.[141] Since the $E2$ and $M3$ matrix elements which connect these states with the ground state are expected to be small, direct single-step excitation mechanisms are no longer expedient. In contrast to ^{152,154}Gd, also electron-capture reactions cannot be used due to their insufficient Q values. Concerning deformed nuclei such as ^{156}Gd and ^{162,164}Dy discussed in this work, multi-step Coulomb excitation [381–383] can be the method of choice. It exploits the collective $B(E2; 2^+_1 \rightarrow 0^+_1)$ and $B(M1; 2^+_{sc} \rightarrow 2^+_1)$ transitions to create a sufficient population of the 2^+_{sc} state.[142] However, the $M1$ nature of the latter transition is a bottleneck since magnetic excitations are suppressed by the velocity factor β^2 [Sec. II A.3. of [382]]. In this case, a potential mixture of the 2^+_{sc} state with close-lying symmetric 2^+ states might be advantageous since it can enhance the excitation cross section significantly. A dedicated analysis must clarify whether a combination of intense beams and a high-Z projectile[143] is sufficient.

If an adequate population from the ground-state cannot be guaranteed, neutron-capture reactions of thermal neutrons can be employed instead. Such experiments can, for instance, be performed at the high-flux reactor of the Institut Laue-Langevin (ILL) in Grenoble, France. In the present case of odd-mass stable samarium, gadolinium, and dysprosium isotopes around $N = 90$, the (n, γ) cross sections range between 10^2 and 10^5 b [384]. The s-wave capture of thermal neutrons populates low-spin states at high excitation energies, which subsequently decay to energetically lower-lying states. These transitions are largely statistical and of dominant $E1$ nature. They can directly populate states of the scissors-mode band if the capture state has negative parity.[144] From angular-correlation measurements, multipole-mixing ratios of secondary transitions can be obtained. In the present case, especially the $2^+_{sc} \rightarrow 2^+_1$, $3^+_{sc} \rightarrow 4^+_1$, and $3^+_{sc} \rightarrow 2^+_1$ transitions are of interest. A small value of the multipole-mixing ratio, i.e. dominant $M1$ character, is a first indication for mixed-symmetric nature of the

[141] The observation of the latter state is also of interest with respect to entanglement in the two-rotor model [380].

[142] In the framework of the IBM-2, only $M1$ transitions of the 2^+_{sc} state exhibit sizeable matrix elements. All $E2$ transitions, on the other hand, are inhibited by the factor $(e_\nu - e_\pi)^2$ which is small for deformed nuclei (cf. Section 6.2.2).

[143] It is assumed that the experiment is performed in normal kinematics, i.e. that the target is composed of the isotope of interest.

[144] This is the case for ^{148,150,152}Sm, all accessible gadolinium isotopes (^{154,156,158}Gd), and ^{164}Dy [79, 181–185, 188]. On the other hand, ^{153}Sm and ^{161}Dy have positive-parity ground states [385, 386] which results in capture states with the same parity quantum numbers.

initial state. Using low-energy photon spectrometers [Sec. 13.I.4. of [387]], even the identification of transitions within the scissors-mode band, which are particularly low in energy, might be achievable. Ultimately, lifetimes of these states can be measured with the GAMS spectrometer [388], which employs the γ-ray induced Doppler broadening (GRID) technique [389]. In particular the ^{157}Gd$(n,\gamma)^{158}$Gd reaction stands out in the region of interest, since it benefits from one of the largest neutron-capture cross sections in the entire nuclear chart. This makes it a perfectly suitable test case for further experiments using reactions with lower cross sections.

7. Summary and outlook

Quantum phase transitions in the equilibrium shapes of even-even atomic nuclei manifest themselves in a multitude of observables. Some, such as excitation energies of the lowest-lying excited states and their transition strengths, belong to the most fundamental quantities studied in nuclei. Others, such as the properties of mixed-symmetry states in general and the scissors mode in particular, are much more involved and require additional knowledge for their interpretation.

The present work is focused on $J^\pi = 1^+$ scissors-mode states of the transitional and deformed rare-earth nuclei ^{154}Gd and ^{162,164}Dy, respectively. These were studied by nuclear resonance fluorescence with quasi-monochromatic, linearly polarized photon beams provided by the High Intensity γ-ray Source. Angular momentum and parity quantum numbers of states in the excitation-energy regions were determined alongside branching and multipole-mixing ratios of their depopulating transitions.

For the well-deformed nucleus ^{164}Dy, significant deviations from the rotational intensity relations are observed for the decays of two dipole states. A K-mixing analysis unveiled comparatively strong mixing between $K = 0$ and $K = 1$ components in the wave functions of both states and yielded first information on the excitation strength of positive-parity dipole states with $K = 0$. It is roughly two orders of magnitude smaller than commonly known $M1$ transitions with $\Delta K = 1$ of axially-symmetric deformed nuclei. The corresponding K mixing matrix element, which arises from first-order Coriolis interaction, is about twice as large as the one admixing ground-state and γ-vibrational bands. Since both effects are rooted in the same underlying mechanism, the exploration of the interrelation of both matrix elements is desirable. This, however, requires the identification of dominant single-particle configurations in the collective modes which might be subject of future microscopic investigations.

The determination of multipole-mixing ratios deviating from zero yields information on $E2$ transition strengths between the scissors mode and the 2_1^+ state. This motivates the preparation of improved calculations in the proton-neutron version of the Interacting Boson Model incorporating local values for the effective quadrupole boson charges. A combination of these predictions and the experimental values yields two novel signatures for phase transitions based on decays of mixed-symmetry states. Still, additional weakly excited 1^+ states, which are associated with the scissors mode, must be included requiring further precision studies. Along with this, the impact of fragmentation on the decay properties of the collective mode must also be addressed. Systematic studies indicate that the parameters of the Majorana interaction in the IBM-2 Hamiltonian cannot be chosen solely relying on transitions of the 1^+ scissors-mode states. Future experiments are needed to identify mixed-symmetric 2^+ states for deformed nuclei, which provides a reliable anchor point for determining these parameters.

For a completion of the systematics across the $N = 90$ quantum phase transition, precision spectroscopy of unstable and low-abundant isotopes is essential. Especially data on neutron-rich cerium and neodymium as well as neutron-deficient dysprosium isotopes can complement the existing data at the low-Z and low-N boundaries.

A. Derivations for the TSM

A.1. Fundamental equations for K mixing

For the derivation of Eqs. (2.6) two mixed dipole states 1_A and 1_B are considered. They can only be composed of parts with K quantum numbers $K = 0$ and $K = 1$. This is modeled in terms of the TSM ansatz

$$\begin{pmatrix} |1_A\rangle \\ |1_B\rangle \end{pmatrix} = \begin{pmatrix} \alpha & \beta \\ -\beta & \alpha \end{pmatrix} \begin{pmatrix} |1_{K=0}\rangle \\ |1_{K=1}\rangle \end{pmatrix} \tag{A.1}$$

with amplitudes α and β normalized to $\alpha^2 + \beta^2 = 1$. Using this ansatz, the branching ratio is given by

$$\begin{aligned} R_{1_A \to 2/0} &= \frac{B(\sigma 1; 1_A \to 2_1^+)}{B(\sigma 1; 1_A \to 0_1^+)} \\ &\overset{(1)}{=} \frac{|\langle 1_A \| \boldsymbol{T}(\sigma 1) \| 2_1^+ \rangle|^2}{|\langle 1_A \| \boldsymbol{T}(\sigma 1) \| 0_1^+ \rangle|^2} \\ &\overset{(2)}{=} \left[\frac{\alpha \langle 1_{K=0} \| \boldsymbol{T}(\sigma 1) \| 2_1^+ \rangle + \beta \langle 1_{K=1} \| \boldsymbol{T}(\sigma 1) \| 2_1^+ \rangle}{\alpha \langle 1_{K=0} \| \boldsymbol{T}(\sigma 1) \| 0_1^+ \rangle + \beta \langle 1_{K=1} \| \boldsymbol{T}(\sigma 1) \| 0_1^+ \rangle} \right]^2 \\ &\overset{(3)}{=} \left[\frac{\alpha \sqrt{5} \langle 2010|10 \rangle \langle \Delta K = 0 \rangle + \beta \sqrt{10} \langle 2011|11 \rangle \langle \Delta K = 1 \rangle}{\alpha \sqrt{5} \langle 0010|10 \rangle \langle \Delta K = 0 \rangle + \beta \sqrt{10} \langle 0011|11 \rangle \langle \Delta K = 1 \rangle} \right]^2 \\ &\overset{(4)}{=} 5 \left[\frac{\langle 2010|10 \rangle + \sqrt{2} \gamma Z \langle 2011|11 \rangle}{\langle 0010|10 \rangle + \sqrt{2} \gamma Z \langle 0011|11 \rangle} \right]^2 \\ &\overset{(5)}{=} \left[\frac{\gamma Z + \sqrt{2}}{1 + \sqrt{2} \gamma Z} \right]^2 \end{aligned}$$

with

$$\langle \Delta K = 0 \rangle = \langle K_f = 0 ||| \boldsymbol{T}(\sigma 1) ||| K_i = 0 \rangle \text{ and}$$
$$\langle \Delta K = 1 \rangle = \langle K_f = 1 ||| \boldsymbol{T}(\sigma 1) ||| K_i = 0 \rangle.$$

The definition of the reduced transition strength [Eq. (1A-67) of [28]] along with the symmetry properties of matrix elements are exploited in Step (1). The resulting mixed matrix elements are subsequently expressed as linear combinations of matrix elements with good K quantum number according to Eq. (A.1) [cf. Step (2)]. Since the ground-state band is characterized by $K = 0$, the dependence of the matrix elements on J, which is purely geometrical, can be reduced using the relation [Eq. (4-92) of [4]]

$$\langle J'_{K_f} \| \boldsymbol{T}(\sigma\lambda) \| J_{K_i=0} \rangle$$
$$= \sqrt{2J+1} \langle J 0 \lambda K_f | J' K_f \rangle \langle K_f ||| \boldsymbol{T}(\sigma\lambda) ||| K_i = 0 \rangle \begin{cases} 1 & \text{if} \quad K_f = 0 \\ \sqrt{2} & \text{else.} \end{cases}$$

This property is exploited in Step (3). Finally, the TSM parameters $\gamma = \beta/\alpha$ and $Z = \langle K_f = 1 ||| \boldsymbol{T}(\sigma 1) ||| K_i = 0 \rangle / \langle K_f = 0 ||| \boldsymbol{T}(\sigma 1) ||| K_i = 0 \rangle$ are introduced and Clebsch-Gordan coefficients are evaluated in Steps (4) and (5), respectively. In completely analogous procedures, the relations

$$R_{1_B \to 2/0} = \frac{B(\sigma 1; 1_B \to 2_1^+)}{B(\sigma 1; 1_B \to 0_1^+)} = \left[\frac{\sqrt{2}\gamma + Z}{\sqrt{2}Z - \gamma} \right]^2 \text{ and}$$
$$B_{A/B} \quad = \frac{B(\sigma 1; 1_A \to 0_1^+)}{B(\sigma 1; 1_B \to 0_1^+)} = \left[\frac{1 + \sqrt{2}\gamma Z}{\sqrt{2}Z - \gamma} \right]^2$$

are obtained for the branching ratio of the 1_B state and the ratio of absolute transition strengths, respectively.

Once the final values for γ and Z are obtained, underlying parameters of the TSM can be determined. Using information on γ the amplitudes α and β are calculated via

$$\alpha^2 = \frac{1}{1+\gamma^2} \qquad \text{and} \qquad \beta^2 = \frac{\gamma^2}{1+\gamma^2}.$$

As required, the normalization condition $\alpha^2 + \beta^2 = 1$ is fulfilled. Furthermore, the excitation strength of the unperturbed $1_{K=0}$ basis state can be extracted by

$$\begin{aligned} B(\sigma 1; 0_1^+ \to 1_{K=0}) &\overset{(1)}{=} |\langle 1_{K=0} \| \boldsymbol{T}(\sigma 1) \| 0_1^+ \rangle|^2 \\ &\overset{(3)}{=} [\langle 0010|10\rangle \langle \Delta K = 0 \rangle]^2 \\ &\overset{(5)}{=} [\langle \Delta K = 0 \rangle]^2. \end{aligned} \tag{A.2}$$

The individual Steps (1), (3), and (5) are as introduced above.

A.2. Determination of V_{mix}

In the following, a generic two-state model for a Hamiltonian $\boldsymbol{H} = \boldsymbol{H_0} + \boldsymbol{H_1}$ is considered. It features two mixed states $|A\rangle$ and $|B\rangle$ with energies E_A and E_B, which are composed of eigenstates $|\varphi_I\rangle$ and $|\varphi_{II}\rangle$ of $\boldsymbol{H_0}$, i.e.

$$\begin{pmatrix} |A\rangle \\ |B\rangle \end{pmatrix} = \begin{pmatrix} \alpha & \beta \\ -\beta & \alpha \end{pmatrix} \begin{pmatrix} |\varphi_I\rangle \\ |\varphi_{II}\rangle \end{pmatrix}$$

with $\alpha^2 + \beta^2 = 1$. The mixing matrix element V_{mix} can be calculated from the mixing strength $\gamma = \beta/\alpha$ and the known final energies E_A and E_B. Since $|A\rangle$ and $|B\rangle$ are eigenstates of $\boldsymbol{H}$ with eigenvalues E_A and E_B, they obey the eigenvalue equations

$$\begin{aligned} \begin{pmatrix} E_I & V_{\text{mix}} \\ V_{\text{mix}} & E_{II} \end{pmatrix} \begin{pmatrix} \alpha \\ \beta \end{pmatrix} &= E_A \begin{pmatrix} \alpha \\ \beta \end{pmatrix} \text{ and} \\ \begin{pmatrix} E_I & V_{\text{mix}} \\ V_{\text{mix}} & E_{II} \end{pmatrix} \begin{pmatrix} -\beta \\ \alpha \end{pmatrix} &= E_B \begin{pmatrix} -\beta \\ \alpha \end{pmatrix}. \end{aligned}$$

Solving these equations yields two expressions each for the unperturbed energies E_I and E_{II} as functions of the mixing amplitudes α and β, the perturbed energies E_A and E_B, and the mixing matrix element V_{mix}. Subsequently, the latter is given by

$$V_{\text{mix}} = \alpha\beta(E_A - E_B) = \frac{\gamma}{1+\gamma^2}(E_A - E_B).$$

B. IBM calculations

The calculations within the framework of the Interacting Boson Model (cf. Section 2.3) employ the F-spin symmetric IBM-2 Hamiltonian given in Eq. (2.16) along with the $M1$ and $E2$ operators of Eqs. (2.13) and (2.15), respectively. The diagonalization of the Hamiltonian matrix and the calculation of transition matrix elements are executed with the computer code ArbModel [390].

Starting from available parameter sets [358] the parameters ϵ, κ, and χ of an IBM-1 Hamiltonian are chosen in an iterative procedure. Particular emphasis is placed on the exact reproduction of the $R_{4/2}$ ratio and a close match of the 0^+_β and 2^+_γ energies. Switching to the IBM-2, the Majorana parameters ξ_i, $i \in \{1,2,3\}$, are determined along with boson g factors. Here, exact reproduction of the mean excitation energy $\overline{E}(1^+_{sc})$ [cf. Eq. (2.20)] and the summed $B(M1; 1^+_{sc} \rightarrow 0^+_1)$ transition strength is required. If additional decay channels of the scissors mode are known, e.g. to the 0^+_β and 2^+_γ states, $\xi_1 = \xi_3$ and ξ_2 are chosen independently. Otherwise, $\xi_1 = \xi_2 = \xi_3$ is used. The boson g factors g_π and g_ν are inferred from the experimental values for the magnetic moment of the 2^+_1 state [371]. Ultimately, the quadrupole boson charges e_π and e_ν are set such that the $\Delta F = 0$ and $\Delta F = 1$ transition strengths $B(E2; 2^+_1 \rightarrow 0^+_1)$ and $B(E2; 1^+_{sc} \rightarrow 2^+_1)$ are exactly reproduced, respectively.

In the following, the parameter sets for ^{154,156}Gd and ^{162,164}Dy, which were determined in this work, are collected in combination with a comparison of IBM-2 predictions and experimental values. By virtue of the iterative approach an improved description of the gadolinium isotopes is obtained while at the same time reducing the number of adapted parameters.

B.1. ^{154}Gd

The experimental energies of the low-lying symmetric states and their transitions are taken from Ref. [184]. The 0^+_β and 2^+_γ states are identified as the 0^+_2 and 2^+_3 states at 660.6673(18) and 996.2568(16) keV, respectively. Data on $M1$ properties of scissors-mode states is collected in Ref. [19]; in particular an excitation strength-weighted energy [cf. Eq. (2.20)] of $\overline{E}(1^+_{\mathrm{sc}}) = 3015(10)$ keV and a summed $M1$ decay strength of $1.04(12)\,\mu_N^2$ are given.

The $B(E2; 1^+_{\mathrm{sc}} \to 2^+_1)$ strength (cf. Tab. 6.1) is extracted for the scissors-mode state at 2934.2(6) keV, which makes up roughly 51% of the summed $M1$ strength. Hence, the $\Delta F = 1$ $E2$ transition strength is multiplied by a factor of 1.96 to account for the remaining states assuming that $M1$ and $E2$ strength are equally distributed among all considered states.

The adopted IBM-2 parameters are collected in Tab. B.1 and a comparison of experimental observables to model predictions is given in Tab. B.2.

Table B.1.: Parameters of the F-spin symmetric Hamiltonian given in Eq. (2.16) and the $M1$ and $E2$ operators of Eqs. (2.13) and (2.15) for the nucleus ^{154}Gd, respectively.

Parameter	$\xi_1 = \xi_2 = \xi_3$	$\xi_1 = \xi_3$, ξ_2	Unit
ϵ	0.580	0.580	MeV
κ	−0.018	−0.018	MeV
χ	−1.288	−1.288	
ξ_1	0.384	0.715	MeV
ξ_2	0.384	0.234	MeV
ξ_3	0.384	0.715	MeV
g_π	1.062	1.124	μ_N
g_ν	−0.607	−0.715	μ_N
e_π	0.148	0.149	eb
e_ν	0.124	0.123	eb

Table B.2.: Comparison of experimental excitation energies and transition strengths of ^{154}Gd to results obtained in the IBM-2 using the Hamiltonian given in Eq. (2.16) and the $M1$ and $E2$ operators of Eqs. (2.13) and (2.15), respectively. The calculations are performed using the computer code ArbModel [390]. Experimental data is, if not indicated otherwise, taken from Ref. [184].

Observable	Experiment	IBM		Unit
		$\xi_1 = \xi_2 = \xi_3$	$\xi_1 = \xi_3, \xi_2$	
$E(0_1^+)$	0.000	0.000	0.000	MeV
$E(2_1^+)$	0.123	0.123	0.123	MeV
$E(4_1^+)$	0.371	0.371	0.371	MeV
$E(6_1^+)$	0.718	0.729	0.729	MeV
$E(0_\beta^+)$	0.681	0.692	0.692	MeV
$E(2_\gamma^+)$	0.996	0.966	0.966	MeV
$E(0_3^+)$	1.182	1.478	1.478	MeV
$\overline{E}(1_{\mathrm{sc}}^+)$	3.015[a]	3.015	3.015	MeV
$\overline{E}(2_{\mathrm{ms}}^+)$		2.984	2.321	MeV
$B(E2; 2_1^+ \to 0_1^+)$	157(1)	157	157	W.u.
$B(E2; 4_1^+ \to 2_1^+)$	245(9)	232	232	W.u.
$B(E2; 6_1^+ \to 4_1^+)$	285(15)	259	259	W.u.
$B(E2; 0_\beta^+ \to 2_1^+)$	52(8)	46.4	46.4	W.u.
$B(E2; 2_\gamma^+ \to 0_1^+)$	1.12(25)	0.307	0.307	W.u.
$B(E2; 1_{\mathrm{sc}}^+ \to 2_1^+)$	$0.36^{+0.15}_{-0.12}$[b]	0.372	0.355	W.u.
$B(E2; 2_{\mathrm{ms}}^+ \to 0_1^+)$		0.177	0.128	W.u.
$\mu(2_1^+)$	0.91(4)[c]	0.910	0.910	μ_N
$B(M1; 1_{\mathrm{sc}}^+ \to 0_1^+)$	1.04(12)[a]	1.040	1.040	μ_N^2
$B(M1; 1_{\mathrm{sc}}^+ \to 2_1^+)$	0.52(6)[a]	0.709	0.688	μ_N^2
$B(M1; 1_{\mathrm{sc}}^+ \to 0_\beta^+)$	0.094(14)[a]	0.309	0.094	μ_N^2
$B(M1; 1_{\mathrm{sc}}^+ \to 2_\gamma^+)$	0.10(5)[a]	0.206	0.064	μ_N^2
$B(M1; 2_{\mathrm{ms}}^+ \to 2_1^+)$		1.626	0.721	μ_N^2

[a] From Ref. [19].
[b] This work.
[c] From Ref. [371].

B.2. ^{156}Gd

The experimental energies of the low-lying symmetric states and their transitions are taken from Ref. [79]. The 0^+_β and 2^+_γ states are identified as the 0^+_2 and 2^+_3 states at 1049.487(2) and 1154.152(2) keV, respectively. Data on $M1$ properties of scissors-mode states is collected in Ref. [19]; in particular an excitation strength-weighted energy [cf. Eq. (2.20)] of $\overline{E}(1^+_{sc})$ =3060(7) keV and a summed $M1$ decay strength of $1.02(9)\,\mu_N^2$ are given.

The $B(E2; 1^+_{sc} \rightarrow 2^+_1)$ strength (cf. Tab. 6.1) is extracted for the scissors-mode state at 3070 keV [24], which makes up roughly 40% of the summed $M1$ strength. Hence, the $\Delta F = 1$ $E2$ transition strength is multiplied by a factor of 2.53 to account for the remaining states assuming that $M1$ and $E2$ strength are equally distributed among all considered states.

The adopted IBM-2 parameters are collected in Tab. B.3 and a comparison of experimental observables to model predictions is given in Tab. B.4.

Table B.3.: Parameters of the F-spin symmetric Hamiltonian given in Eq. (2.16) and the $M1$ and $E2$ operators of Eqs. (2.13) and (2.15) for the nucleus ^{156}Gd, respectively.

Parameter	$\xi_1 = \xi_2 = \xi_3$	$\xi_1 = \xi_3$, ξ_2	Unit
ϵ	0.423	0.423	MeV
κ	−0.021	−0.021	MeV
χ	−0.898	−0.898	
ξ_1	0.358	0.595	MeV
ξ_2	0.358	0.212	MeV
ξ_3	0.358	0.595	MeV
g_π	0.945	0.983	μ_N
g_ν	−0.394	−0.447	μ_N
e_π	0.148	0.148	eb
e_ν	0.134	0.134	eb

Table B.4.: Comparison of experimental excitation energies and transition strengths of ^{156}Gd to results obtained in the IBM-2 using the Hamiltonian given in Eq. (2.16) and the $M1$ and $E2$ operators of Eqs. (2.13) and (2.15), respectively. The calculations are performed using the computer code ArbModel [390]. Experimental data is, if not indicated otherwise, taken from Ref. [79].

Observable	Experiment	IBM		Unit
		$\xi_1 = \xi_2 = \xi_3$	$\xi_1 = \xi_3, \xi_2$	
$E(0_1^+)$	0.000	0.000	0.000	MeV
$E(2_1^+)$	0.089	0.089	0.089	MeV
$E(4_1^+)$	0.288	0.288	0.288	MeV
$E(6_1^+)$	0.585	0.591	0.591	MeV
$E(0_\beta^+)$	1.049	1.036	1.036	MeV
$E(2_\gamma^+)$	1.154	1.133	1.133	MeV
$E(0_3^+)$	1.168	1.836	1.836	MeV
$\overline{E}(1_{sc}^+)$	3.060[a]	3.060	3.060	MeV
$\overline{E}(2_{sc}^+)$		3.086	2.523	MeV
$B(E2; 2_1^+ \to 0_1^+)$	189(3)	189	189	W.u.
$B(E2; 4_1^+ \to 2_1^+)$	264(4)	269	269	W.u.
$B(E2; 6_1^+ \to 4_1^+)$	295(8)	293	292	W.u.
$B(E2; 0_\beta^+ \to 2_1^+)$	8^{+4}_{-7}	11.9	11.9	W.u.
$B(E2; 2_\gamma^+ \to 0_1^+)$	4.68(16)	1.581	1.581	W.u.
$B(E2; 1_{sc}^+ \to 2_1^+)$	0.093(66)[b]	0.113	0.094	W.u.
$B(E2; 2_{sc}^+ \to 0_1^+)$		0.049	0.019	W.u.
$\mu(2_1^+)$	0.774(8)[c]	0.774	0.774	μ_N
$B(M1; 1_{sc}^+ \to 0_1^+)$	1.02(9)[a]	1.020	1.020	μ_N^2
$B(M1; 1_{sc}^+ \to 2_1^+)$	0.51(6)[a]	0.619	0.614	μ_N^2
$B(M1; 1_{sc}^+ \to 0_\beta^+)$	0.013(4)[a]	0.134	0.013	μ_N^2
$B(M1; 2_{sc}^+ \to 2_1^+)$		1.608	0.410	μ_N^2

[a] From Ref. [19].
[b] This work.
[c] From Ref. [371].

B.3. ^{162}Dy

The experimental energies of the low-lying symmetric states and their transitions are taken from Ref. [187]. The 0^+_β and 2^+_γ states are identified as the 0^+_2 and 2^+_2 states at 1400.26(6) and 888.161(3) keV, respectively. The lifetime of the former state and, thus, the transition strengths of its depopulating transitions are unknown. Data on scissors-mode states is collected in Ref. [154]. It yields, in combination with results of the present work (cf. Section 5.2), an excitation strength-weighted energy [cf. Eq. (2.20)] of $\overline{E}(1^+_{sc}) = 2934(225)$ keV and a summed $M1$ decay strength of $0.960(51)\,\mu_N^2$.[145]

The $B(E2; 1^+_{sc} \rightarrow 2^+_1)$ strength (cf. Tab. 6.1) is extracted for the scissors-mode states at 2900.0(3) and 3061.2(3) keV, which make up roughly 83% of the summed $M1$ strength. Hence, the summed $\Delta F = 1$ $E2$ transition strength is multiplied by a factor of 1.20 to account for the remaining states assuming that $M1$ and $E2$ strength are equally distributed among all considered states.

The adopted IBM-2 parameters are collected in Tab. B.5 and a comparison of experimental observables to model predictions is given in Tab. B.6.

Table B.5.: Parameters of the F-spin symmetric Hamiltonian given in Eq. (2.16) and the $M1$ and $E2$ operators of Eqs. (2.13) and (2.15) for the nucleus ^{162}Dy, respectively.

Parameter	$\xi_1 = \xi_2 = \xi_3$	Unit
ϵ	0.194	MeV
κ	−0.028	MeV
χ	−0.335	
ξ_1	0.243	MeV
ξ_2	0.243	MeV
ξ_3	0.243	MeV
g_π	0.851	μ_N
g_ν	−0.233	μ_N
e_π	0.137	eb
e_ν	0.132	eb

[145] In contrast to Ref. [150], the $J^\pi = 1^+$ state at 2929.4(7) keV (cf. Section 5.2) is included.

Table B.6.: Comparison of experimental excitation energies and transition strengths of ^{162}Dy to results obtained in the IBM-2 using the Hamiltonian given in Eq. (2.16) and the $M1$ and $E2$ operators of Eqs. (2.13) and (2.15), respectively. The calculations are performed using the computer code ArbModel [390]. Experimental data is, if not indicated otherwise, taken from Ref. [187].

Observable	Experiment	IBM $\xi_1 = \xi_2 = \xi_3$	Unit
$E(0_1^+)$	0.000	0.000	MeV
$E(2_1^+)$	0.081	0.081	MeV
$E(4_1^+)$	0.266	0.266	MeV
$E(6_1^+)$	0.549	0.544	MeV
$E(0_\beta^+)$	1.400	1.411	MeV
$E(2_\gamma^+)$	0.888	0.916	MeV
$E(0_3^+)$	1.666	2.002	MeV
$\overline{E}(1_{sc}^+)$	2.934[a,b]	2.934	MeV
$\overline{E}(2_{sc}^+)$		2.966	MeV
$B(E2; 2_1^+ \to 0_1^+)$	204(3)	204	W.u.
$B(E2; 4_1^+ \to 2_1^+)$	289(12)	292	W.u.
$B(E2; 6_1^+ \to 4_1^+)$	301(17)	320	W.u.
$B(E2; 0_\beta^+ \to 2_1^+)$		2.569	W.u.
$B(E2; 2_\gamma^+ \to 0_1^+)$	4.6(3)	9.283	W.u.
$B(E2; 1_{sc}^+ \to 2_1^+)$	$0.011^{+0.089}_{-0.011}$[b]	0.011	W.u.
$B(E2; 2_{sc}^+ \to 0_1^+)$		0.006	W.u.
$\mu(2_1^+)$	0.69(3)[c]	0.690	μ_N
$B(M1; 1_{sc}^+ \to 0_1^+)$	0.96(5)[a,b]	0.960	μ_N^2
$B(M1; 1_{sc}^+ \to 2_1^+)$	0.46(3)[a,b]	0.542	μ_N^2
$B(M1; 2_{sc}^+ \to 2_1^+)$		1.446	μ_N^2

[a] From Ref. [154].
[b] This work.
[c] From Ref. [371].

B.4. ^{164}Dy

The experimental energies of the low-lying symmetric states and their transitions are taken from Ref. [188]. The 0^+_β and 2^+_γ states are identified as the 0^+_2 and 2^+_2 states at 1654.71(3) and 761.815(7) keV, respectively. The lifetime of the former state and, thus, the transition strengths of its depopulating transitions are unknown. Data on scissors-mode states is collected in Refs. [150]; in particular an excitation strength-weighted energy [cf. Eq. (2.20)] of $\overline{E}(1^+_{sc})$ =2.97(1) MeV[146] and a summed $M1$ decay strength of 1.08(14) μ_N^2 are given.

The $B(E2; 1^+_{sc} \rightarrow 2^+_1)$ strength (cf. Tab. 6.1) is extracted for the scissors-mode states at 3111.2(3), 3159.1(3), and 3173.6(3) keV, which make up roughly 87% of the summed $M1$ strength. Hence, the summed $\Delta F = 1$ $E2$ transition strength is multiplied by a factor of 1.15 to account for the remaining states assuming that $M1$ and $E2$ strength are equally distributed among all considered states.

The adopted IBM-2 parameters are collected in Tab. B.7 and a comparison of experimental observables to model predictions is given in Tab. B.8.

Table B.7.: Parameters of the F-spin symmetric Hamiltonian given in Eq. (2.16) and the $M1$ and $E2$ operators of Eqs. (2.13) and (2.15) for the nucleus ^{164}Dy, respectively.

Parameter	$\xi_1 = \xi_2 = \xi_3$	Unit
ϵ	0.000	MeV
κ	−0.031	MeV
χ	−0.236	
ξ_1	0.227	MeV
ξ_2	0.227	MeV
ξ_3	0.227	MeV
g_π	0.870	μ_N
g_ν	−0.190	μ_N
e_π	0.142	eb
e_ν	0.121	eb

[146] Uncertainty estimated from the last digit given in Ref. [150].

Table B.8.: Comparison of experimental excitation energies and transition strengths of ^{164}Dy to results obtained in the IBM-2 using the Hamiltonian given in Eq. (2.16) and the $M1$ and $E2$ operators of Eqs. (2.13) and (2.15), respectively. The calculations are performed using the computer code ArbModel [390]. Experimental data is, if not indicated otherwise, taken from Ref. [188].

Observable	Experiment	IBM $\xi_1 = \xi_2 = \xi_3$	Unit
$E(0_1^+)$	0.000	0.000	MeV
$E(2_1^+)$	0.073	0.073	MeV
$E(4_1^+)$	0.242	0.242	MeV
$E(6_1^+)$	0.501	0.495	MeV
$E(0_\beta^+)$	1.655	1.367	MeV
$E(2_\gamma^+)$	0.762	0.836	MeV
$E(0_3^+)$	1.780	2.218	MeV
$\overline{E}(1_{sc}^+)$	2.97(1)[a,b]	2.970	MeV
$\overline{E}(2_{sc}^+)$		2.999	MeV
$B(E2; 2_1^+ \to 0_1^+)$	211(4)	211	W.u.
$B(E2; 4_1^+ \to 2_1^+)$	271(11)	302	W.u.
$B(E2; 6_1^+ \to 4_1^+)$	303(9)	332	W.u.
$B(E2; 0_\beta^+ \to 2_1^+)$		1.535	W.u.
$B(E2; 2_\gamma^+ \to 0_1^+)$	4.3(3)	10.665	W.u.
$B(E2; 1_{sc}^+ \to 2_1^+)$	$0.20^{+0.15}_{-0.13}$[c]	0.205	W.u.
$B(E2; 2_{sc}^+ \to 0_1^+)$		0.108	W.u.
$\mu(2_1^+)$	0.68(2)[d]	0.680	μ_N
$B(M1; 1_{sc}^+ \to 0_1^+)$	1.08(14)[a]	1.080	μ_N^2
$B(M1; 1_{sc}^+ \to 2_1^+)$	0.54(7)[a,e]	0.597	μ_N^2
$B(M1; 2_{sc}^+ \to 2_1^+)$		1.584	μ_N^2

[a] From Ref. [150].
[b] See footnote [146].
[c] This work.
[d] From Ref. [371].
[e] Assuming a branching ratio [cf. Eq. (4.5)] of 0.5 according to Alaga.

C. Experimental supplement

Comprehensive information on the experiments presented in Section 3.3 are collected in this Appendix. This includes detector arrangements, target compositions, and run plans taken from Refs. [262, 391].

C.1. ^{154}Gd

The nuclear resonance fluorescence experiment on the scissors mode of ^{154}Gd was performed at the High Intensity γ-ray Source in May and June 2018.

Detector setup

The experiment utilized the γ^3 setup [247] comprising four high-purity germanium (HPGe) detectors and four 3 in × 3 in cerium-doped lanthanum bromide ($LaBr_3$:Ce) scintillators. The positions of the former in terms of polar and azimuthal angles ϑ and φ are collected in Tab. C.1, respectively. It is complemented by further information specifying the exact position of the detectors with respect to the beam pipe. The $LaBr_3$:Ce scintillators, which take the remaining positions in the γ^3 setup, are not of importance for the present work.

Table C.1.: Positions of the detectors mounted in the γ^3 setup during the ^{154}Gd experiment. Each HPGe detector featured one sheet made of copper and one of lead with thicknesses of $1/16$ in each. The detectors placed at polar angles $\vartheta = 90°$ were equipped with an additional lead sheet of the same dimensions.

Detector	Serial number	ϑ (°)	φ (°)	Distance[a] (mm)	Projection[b] (mm)
HPGe1	36-TN40663A	135	315	40(1)	182(1) / 299(1)
HPGe2	36-TN30986A	90	90	57(1)	170(1) / 253(1)
HPGe3	36-TN31061A	135	45	40(1)	174(1) / 299(1)
HPGe4	43-TP31670A[c]	90	180	65(1)	174(1) / 286(1)

[a] Measured from the detector front cap (with shielding attached) to the beam pipe.
[b] Projection of the detector crystal onto the beam pipe relative to an arbitrary zero which is located 4 mm downstream of the γ^3 wheel. The target position is found at a distance of 219(1) mm.
[c] HPGe detector on loan from Argonne National Laboratory.

Target

The irradiated gadolinium oxide was on loan from Oak Ridge National Laboratory with Batch No. 160791. The material was enclosed in a high-density polyethylene (HDPE, C_2H_4) container with 0.75 in inner diameter. It was equipped with two 0.5 mm thick aluminum sheets up- and downstream of the gadolinium weighing 531.05(1) and 551.51(1) mg, respectively. These were produced from Alfa Aesar Puratronic® (Product No. 43425, Lot No. H01Z037) aluminum foil.

Table C.2.: General characteristics of the compound target used in the experiment described in Section 3.3.1.

Property	Value		Unit
	Gd	Al	
Chemical form	Gd_2O_3	Al	
Physical form	powder	metal	
Compound weight	5711.1		mg
Element weight	4978(25)[a]	531.05(1)[b]	mg
		551.51(1)[b]	mg
Enrichment/purity	66.78(20)[c]	99.9997[c]	%
Container material	HDPE (C_2H_4)		

[a] See footnote [69] of Section 3.3.1.
[b] Up- and downstream of gadolinium target.
[c] Enrichment in ^{154}Gd (cf. Tab. C.3) and purity in aluminum.

The gadolinium target was only 66.78(20)% enriched in ^{154}Gd. In Tab. C.3, its isotopic composition is given. Further impurities are negligible.

Table C.3.: Isotopic composition of the ^{154}Gd target used in the experiment described in Section 3.3.1. The values are taken from the assay provided by Oak Ridge National Laboratory.

Isotope	^{152}Gd	^{154}Gd	^{155}Gd	^{156}Gd	^{157}Gd	^{158}Gd	^{160}Gd
Share	< 0.05	66.78(20)	17.52(10)	7.23(5)	3.16(5)	3.44(5)	1.87(2)

Run plan

During the experiment, distances and shielding of the $LaBr_3$:Ce scintillators as well as their settings and thresholds in the MBS data-acquisition system were changed. All setups are identical for the HPGe detectors if the analogue GENIE data acquisition is considered. In Tab. C.4, a schematic run plan is given.

Table C.4.: Run plan for the ^{154}Gd experiment at HIγS. It is based on the electronic logbook of Ref. [391]. Modifications of the experimental setup or the data-acquisition system are indicated by unnumbered lines. If no beam energy is given, radioactive sources were used for energy and efficiency calibrations.

Run number	E_{beam} (keV)	Target	Setup[a]	Real time (h)
281	Measurement of natural background.			9.96
282		^{56}Co, ^{60}Co[b]		0.82
	Changed shielding of HPGe2 and HPGe4. Changed shielding of all LaBr.			
283	2948(95)	^{154}Gd in vacuum	1	2.53
284	2948(95)	^{154}Gd in vacuum	1	4.62
285[c]	2948(95)	^{154}Gd in vacuum	1	
	Changed shielding of all LaBr. Changed MBS settings and thresholds.			
286	2948(95)	^{154}Gd in vacuum	2	3.15
287[d]	2948(95)	^{154}Gd in vacuum	2	10.15
	Changed distances of LaBr1 and LaBr2.			
288[c]		^{22}Na, ^{137}Cs[b]	3	
289[c]		^{22}Na, ^{137}Cs[b]	3	
290	2948(95)	^{154}Gd in vacuum	3	11.11
291	2948(95)	^{154}Gd in vacuum	3	12.55
292	2948(95)	^{154}Gd in vacuum	3	10.09
293	2948(95)	^{154}Gd in vacuum	3	0.47

Table C.4.: Run plan for the ^{154}Gd experiment at HIγS. (continued)

294	2948(95)	^{154}Gd in vacuum	3	10.00
295[d]	2948(95)	empty target container	3	2.44
296		^{22}Na at target position	3	0.38
297		^{60}Co at target position	3	0.27
298		^{137}Cs at target position	3	0.33
299		^{56}Co at target position	3	9.38
300		^{152}Eu at target position	3	4.54
	Changed distances and shielding of LaBr to setup 2.			
301		^{152}Eu at target position	2	6.13
302		^{22}Na at target position	2	0.34
303		^{60}Co at target position	2	0.49
304		^{137}Cs at target position	2	0.48
305		^{56}Co at target position	2	10.38
	Changed distances and shielding of LaBr to setup 1.			
306		^{56}Co at target position	1	4.60
307		^{22}Na at target position	1	0.31
308		^{60}Co at target position	1	0.29
309		^{137}Cs at target position	1	0.25
310[e]		^{152}Eu at target position	1	5.52

[a] Setups 1, 2, and 3 are identical for the HPGe detectors (cf. Tab. C.1).
[b] Sources placed on beam pipe for a quick energy calibration.
[c] Run was used for adjustment of thresholds in the MBS DAQ. The GENIE DAQ was not running.
[d] Beam profile recorded prior to run using zero-degree detector.
[e] MBS-based DAQ crashed after approximately 1.3 h.

C.2. ^{162}Dy

The nuclear resonance fluorescence experiment on the scissors mode of ^{162}Dy was performed at the High Intensity γ-ray Source in October 2013 prior to the similar measurement on ^{164}Dy.

Detector setup

The experiment utilized the γ^3 setup [247] comprising four high-purity germanium (HPGe) detectors and four 3 in × 3 in cerium-doped lanthanum bromide ($LaBr_3$:Ce) scintillators. Their positions in terms of polar and azimuthal angles ϑ and φ are collected in Tab. C.5, respectively. No information on the exact distances of the detectors from the beam pipe as well as filter settings are available.

Table C.5.: Positions of the detectors mounted in the γ^3 setup during the ^{162}Dy experiment. The exact distances of the detectors from the beam pipe as well as filter settings are not known.

Detector	Serial number	ϑ (°)	φ (°)	Distance[a] (mm)	Projection[b] (mm)
HPGe1		90	0		
HPGe2		90	90		
HPGe3		135	315		
HPGe4		135	225		
LaBr1		135	45		
LaBr2		135	135		
LaBr3		90	180		
LaBr4		90	270		

Target

The irradiated dysprosium oxide was enclosed in a container whose material composition is not known. Since transitions of ^{13}C occur in the spectra (cf. Fig. 5.2), it can at least be concluded that the container most likely contains carbon. Assuming a cylindrical shape, its inner diameter is estimated to be 0.75 in.[147]

Table C.6.: General characteristics of the ^{162}Dy target used in the experiment described in Section 3.3.2.

Property	Value	Unit
Chemical form	Dy_2O_3	
Physical form	unknown	
Compound weight	4692.1(1)[a]	mg
Element weight		mg
Enrichment	96.17(1)	%
Container material	unknown	

[a] Uncertainties estimated from the last digit given in Ref. [262].

The dysprosium itself was 96.17(1)% enriched in ^{162}Dy. In Tab. C.7, its complete isotopic composition is given. Further impurities are negligible.

Table C.7.: Isotopic composition of the ^{162}Dy target used in the experiment described in Section 3.3.2. The values are taken from Ref. [262].

Isotope	^{161}Dy	^{162}Dy	^{163}Dy	^{164}Dy	other
Share	1.24(1)[a]	96.17(1)[a]	1.79(1)[a]	0.72(1)[a]	$< 0.1(1)$[a]

[a] Uncertainties estimated from the last digit given in Ref. [Entry 648 of [262]].

[147] See Section 3.3.2, footnote [73].

Run plan

The experiments on ^{162}Dy and ^{164}Dy were performed directly one after the other. They share source measurements for energy and efficiency calibration. Thus, in Tab. C.8, a schematic run plan of the combined experiments is given.

Table C.8.: Run plan for the ^{162,164}Gd experiment at HIγS. It is based on the electronic logbook of Ref. [262]. If no beam energy is given, radioactive sources were used for energy and efficiency calibrations.

Run number	E_{beam} (keV)	Target	Real time (h)
330[a]	Tuning of the beam.		
	Changed MBS settings and thresholds.		
331	2905(102)	^{162}Dy at target position	8.74
332-334[a]	3069(119)	^{162}Dy at target position	
	Reduced beam curent.		
335	3069(119)	^{162}Dy at target position	8.83
336	3069(119)	^{162}Dy at target position	4.83
337	3069(119)	^{162}Dy at target position	4.60
338	3069(119)	^{162}Dy at target position	2.47
339		^{56}Co[b]	0.78
340[a]	3076(98)	^{164}Dy at target position	5.21
341[a]	3076(98)	^{164}Dy at target position	0.84
342[a]	3076(98)	^{164}Dy at target position	4.17
343	3076(98)	^{164}Dy at target position	4.81
344[a]	3185(102)	^{164}Dy at target position	5.10
345	3185(102)	^{164}Dy at target position	1.73
346	3185(102)	^{164}Dy at target position	0.31
347	3185(102)	^{164}Dy at target position	4.62
348	Measurement of natural background.		10.11
349	3185(102)	^{164}Dy at target position	1.12
350[a]	3185(102)	^{164}Dy at target position	8.43

Table C.8.: Run plan for the ^{162,164}Gd experiment at HIγS. (continued)

351	3185(102)	^{164}Dy at target position	4.25
352[c]		^{56}Co at target position	6.08

[a] Beam profile recorded prior to run using zero-degree detector.
[b] Source placed on beam pipe for a quick energy calibration.
[c] GENIE-based DAQ crashed in the middle of the run.

C.3. ^{164}Dy

The nuclear resonance fluorescence experiment on the scissors mode of ^{164}Dy was performed at the High Intensity γ-ray Source in October 2013 after the similar measurement on ^{162}Dy.

Detector setup

The detector positions are identical to the ones given in Tab. C.5 for the ^{162}Dy experiment. It is not known whether distances or filter settings were changed in between.

Target

The target used in the experiment on ^{164}Dy, which is presented in Section 3.3.2, was composed of two pieces. The 98(1)% enriched dysprosium oxide, which was provided by the Wright Nuclear Structure Laboratory at Yale University, was combined with metallic ^{164}Dy from the Institute for Nuclear Physics, University of Cologne. For these materials neither the isotopic composition nor the exact weight and dimensions are known.

Table C.9.: General characteristics of the ^{164}Dy target used in the experiment described in Section 3.3.2.

Property	Value		Unit
	Target 1	Target 2	
Chemical form	Dy_2O_3	Dy	
Physical form	powder	metallic	
Compound weight	770(1)[a]		mg
Element weight		1100(100)[a]	mg
Enrichment	98(1)[a]		%
Container material	unknown		

[a] Uncertainties estimated from the last digit given in Ref. [Entry 577 of [262]].

Run plan

The experiments on ^{162}Dy and ^{164}Dy were performed directly one after the other. They share source measurements for energy and efficiency calibration. Thus, in Tab. C.8, a combined schematic run plan is given.

D. Compilation of experimental spectra

This Appendix collects the summed HPGe spectra for all runs with the same beam-energy setting. It starts with the ^{154}Gd spectra followed by the ones from ^{162}Dy and ^{164}Dy; each for low and high beam energies. The schematic beam profile is always indicated by a gray dashed line. For better visibility, the number of counts is given in logarithmic order. In Chapter 5, spectra of the excitation-energy regions, which are linear in the number of counts, are found.

The detectors are ordered according to their occurrence in Tabs. C.1 and C.5 and their positions with respect to the beam's horizontal polarization plane are denoted by filled circles. Empty circles indicate the positions of further HPGe detectors with the same polar angle ϑ.

The positions of all identified background lines are marked in the spectra. They mostly originate from the decay of radioactive ^{214}Bi, which is a member of the uranium-radium chain and contained in the surrounding lead, to ^{214}Po [269]. The background line at 1435.795(10) keV stems from ^{138}Ba [267], which is populated after internal conversion of ^{138}La found in the $LaBr_3$:Ce scintillators. Furthermore, single- and double-escape lines are encountered roughly 511 and 1022 keV below their corresponding full-energy peaks, respectively.

D.1. ^{154}Gd

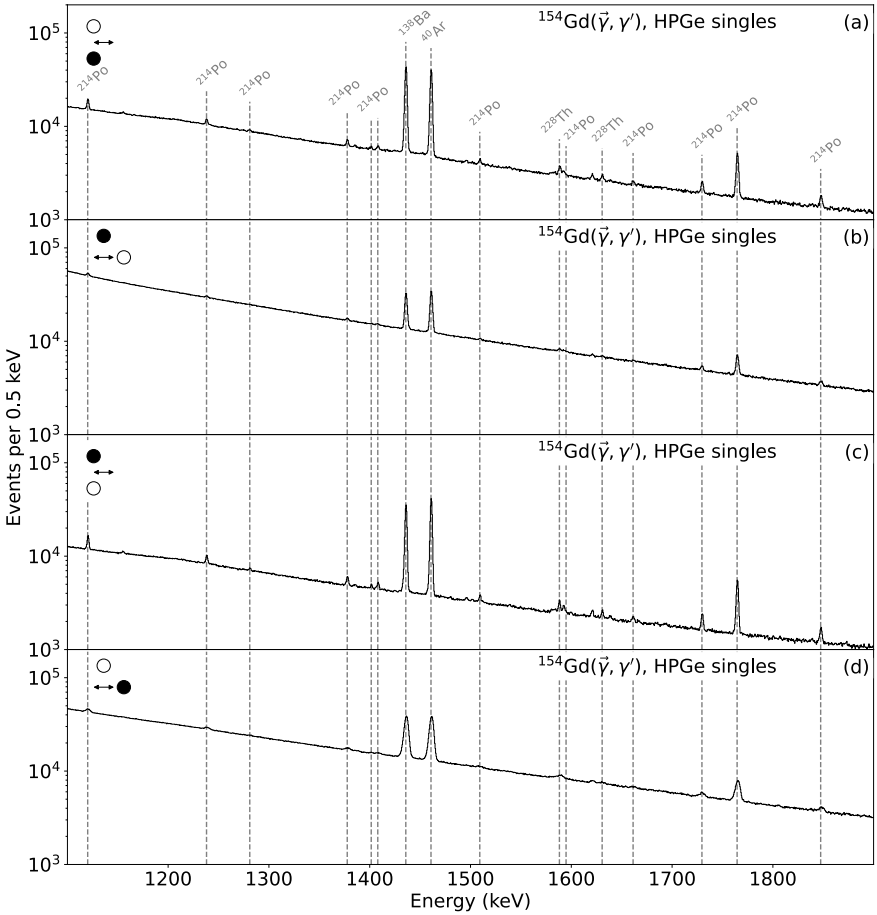

Figure D.1.: Spectra from the ^{154}Gd($\vec{\gamma}, \gamma'$) reaction for a beam energy of 2.935 MeV between 1100 and 1900 keV.

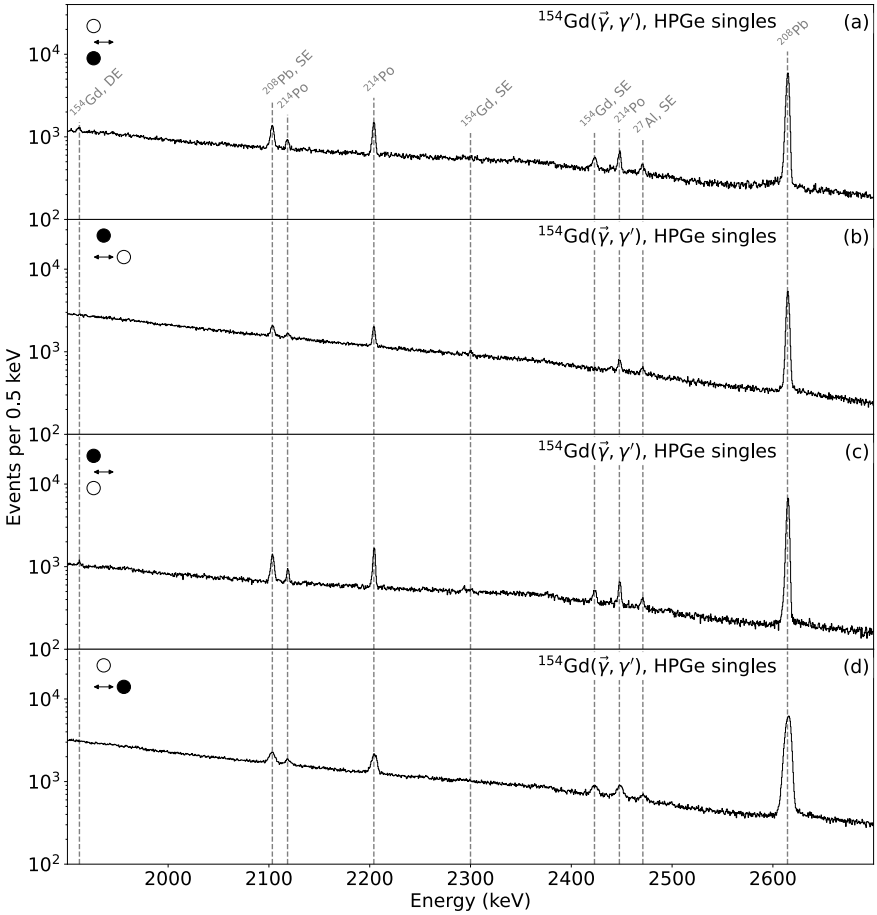

Figure D.2.: Spectra from the ^{154}Gd($\vec{\gamma}, \gamma'$) reaction for a beam energy of 2.935 MeV between 1900 and 2700 keV.

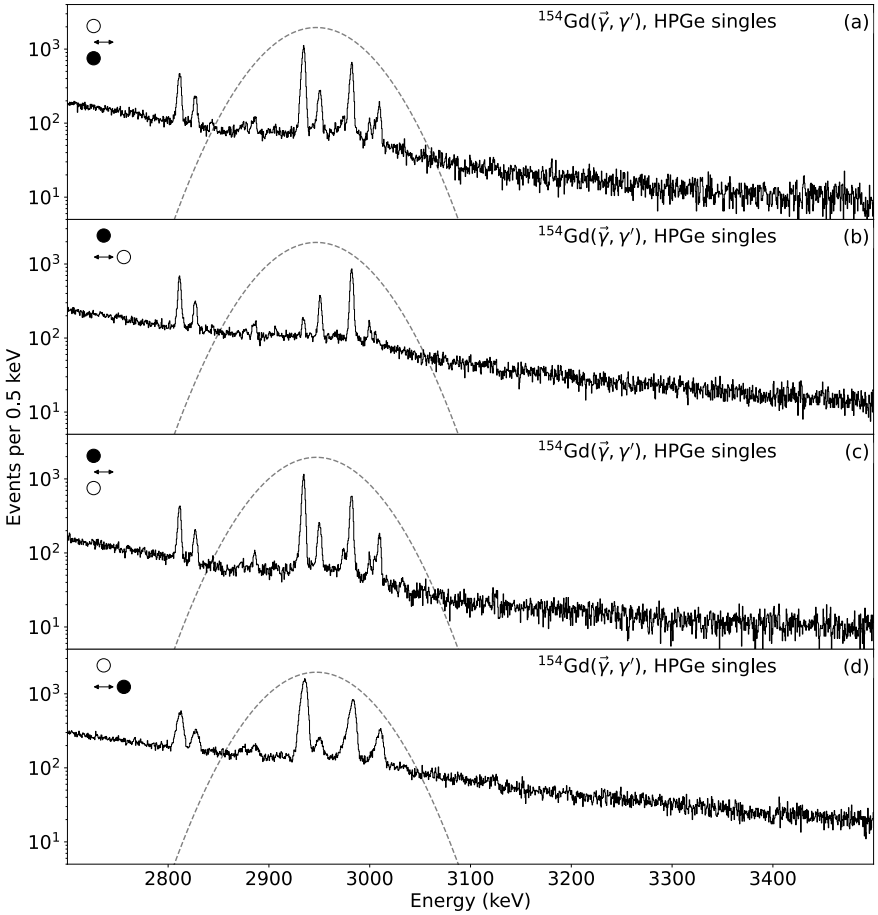

Figure D.3.: Spectra from the ^{154}Gd($\vec{\gamma}, \gamma'$) reaction for a beam energy of 2.935 MeV between 2700 and 3500 keV.

D.2. ^{162}Dy

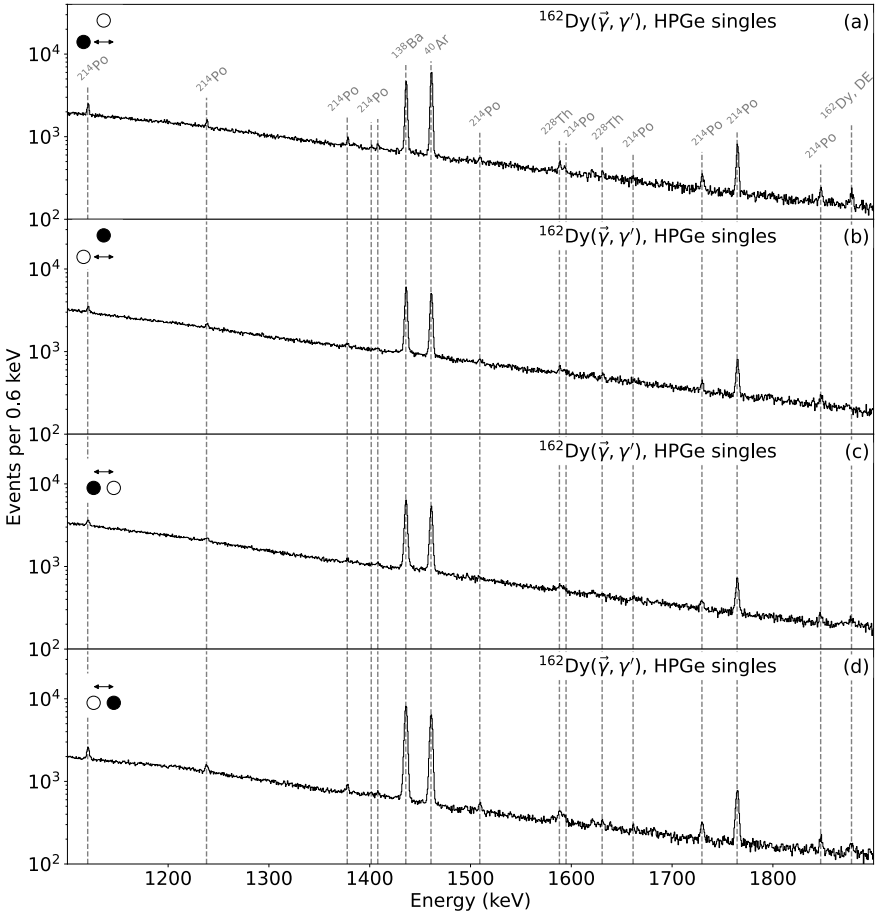

Figure D.4.: Spectra from the ^{162}Dy($\vec{\gamma}$, γ') reaction for a beam energy of 2.900 MeV between 1100 and 1900 keV.

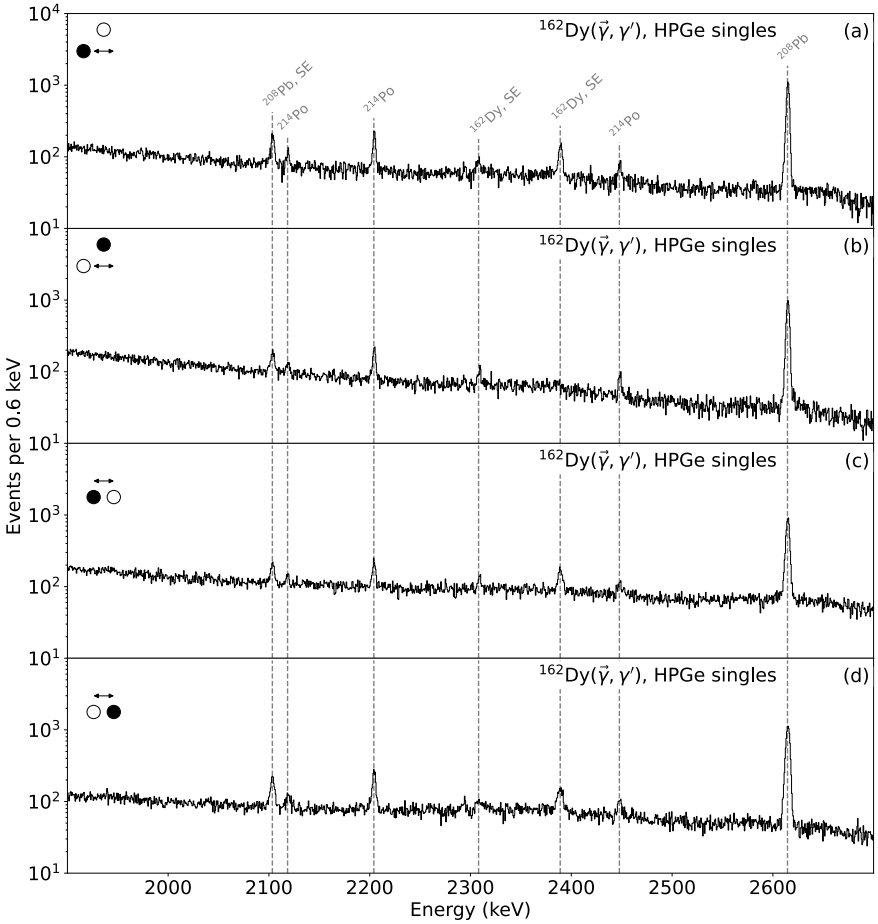

Figure D.5.: Spectra from the ^{162}Dy($\vec{\gamma}, \gamma'$) reaction for a beam energy of 2.900 MeV between 1900 and 2700 keV.

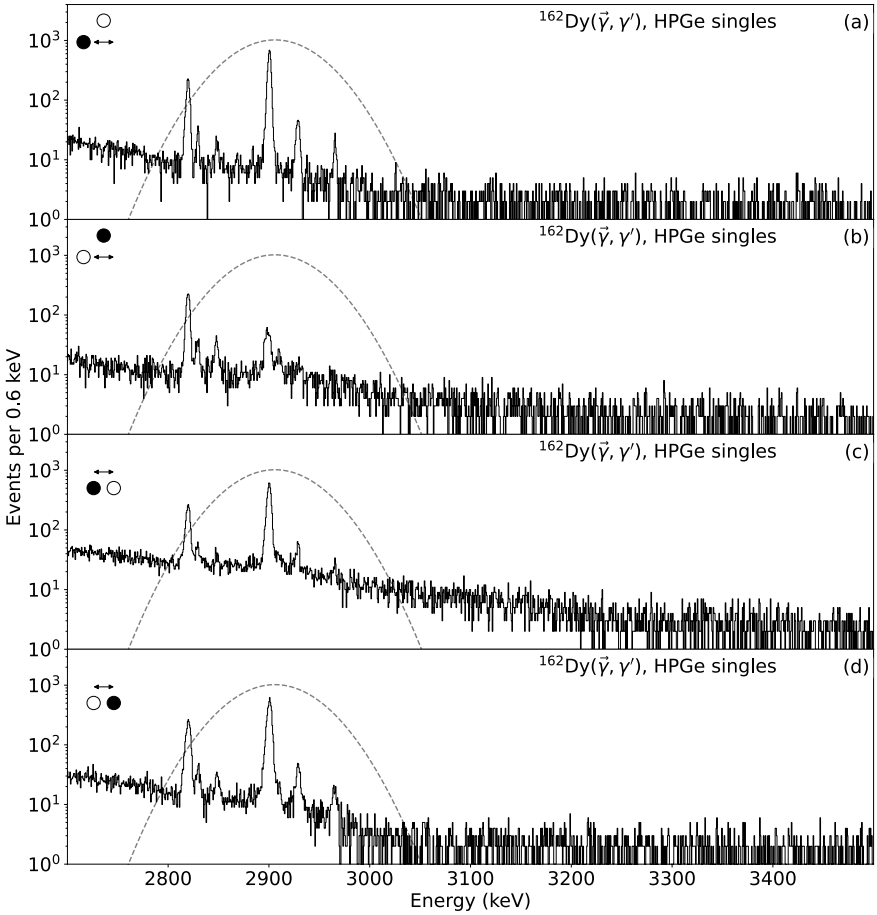

Figure D.6.: Spectra from the ^{162}Dy($\vec{\gamma}, \gamma'$) reaction for a beam energy of 2.900 MeV between 2700 and 3500 keV.

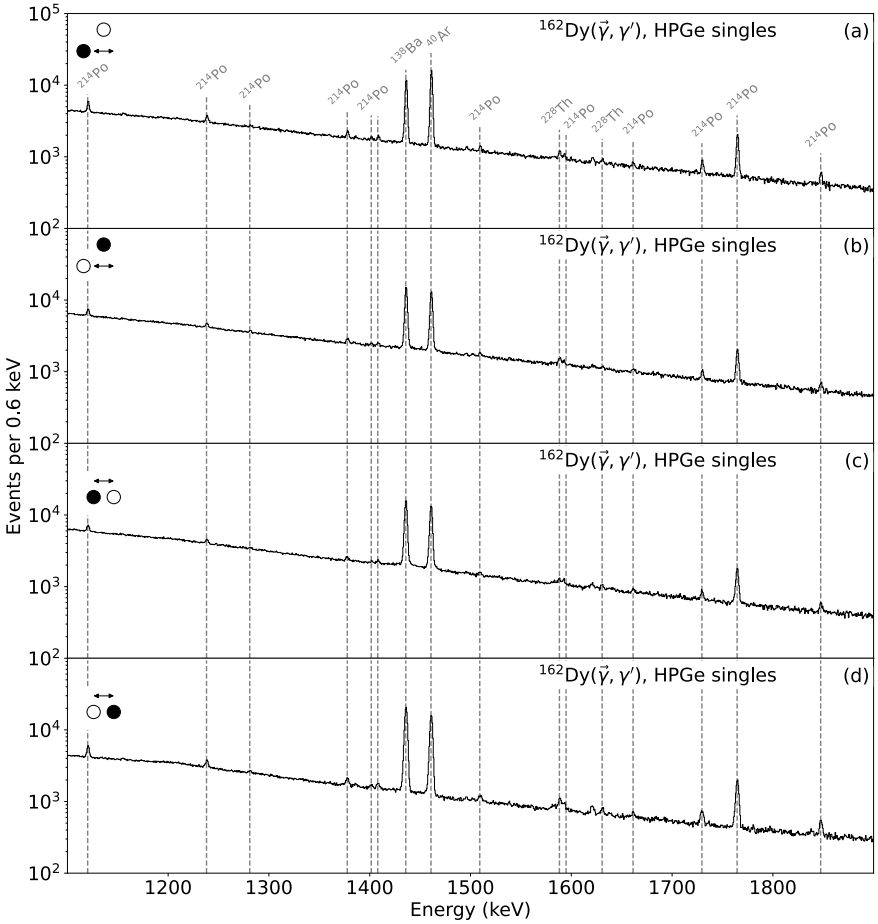

Figure D.7.: Spectra from the ^{162}Dy($\vec{\gamma}, \gamma'$) reaction for a beam energy of 3.060 MeV between 1100 and 1900 keV.

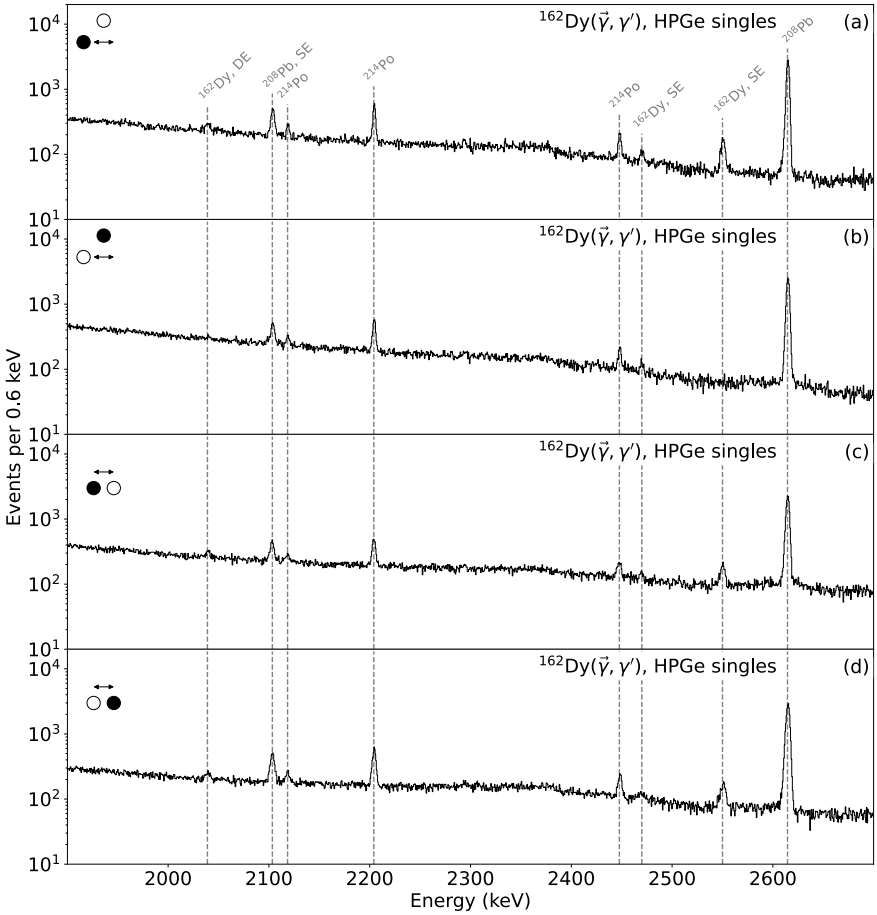

Figure D.8.: Spectra from the ^{162}Dy($\vec{\gamma}, \gamma'$) reaction for a beam energy of 3.060 MeV between 1900 and 2700 keV.

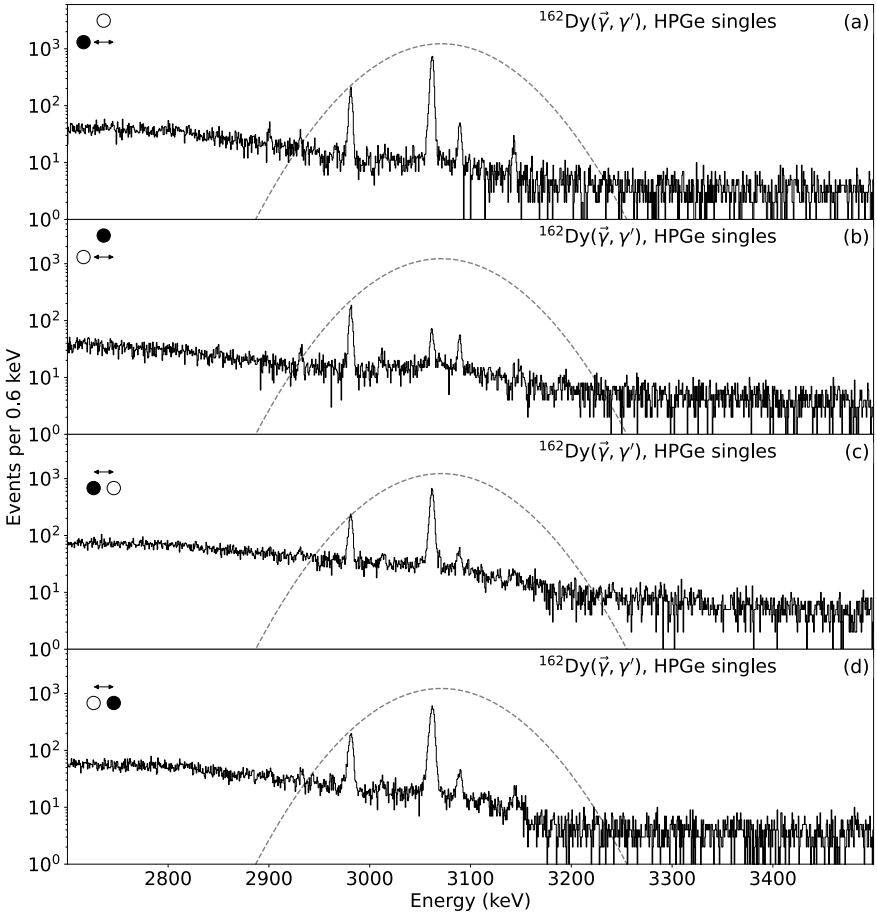

Figure D.9.: Spectra from the ^{162}Dy($\vec{\gamma}, \gamma'$) reaction for a beam energy of 3.060 MeV between 2700 and 3500 keV.

D.3. ^{164}Dy

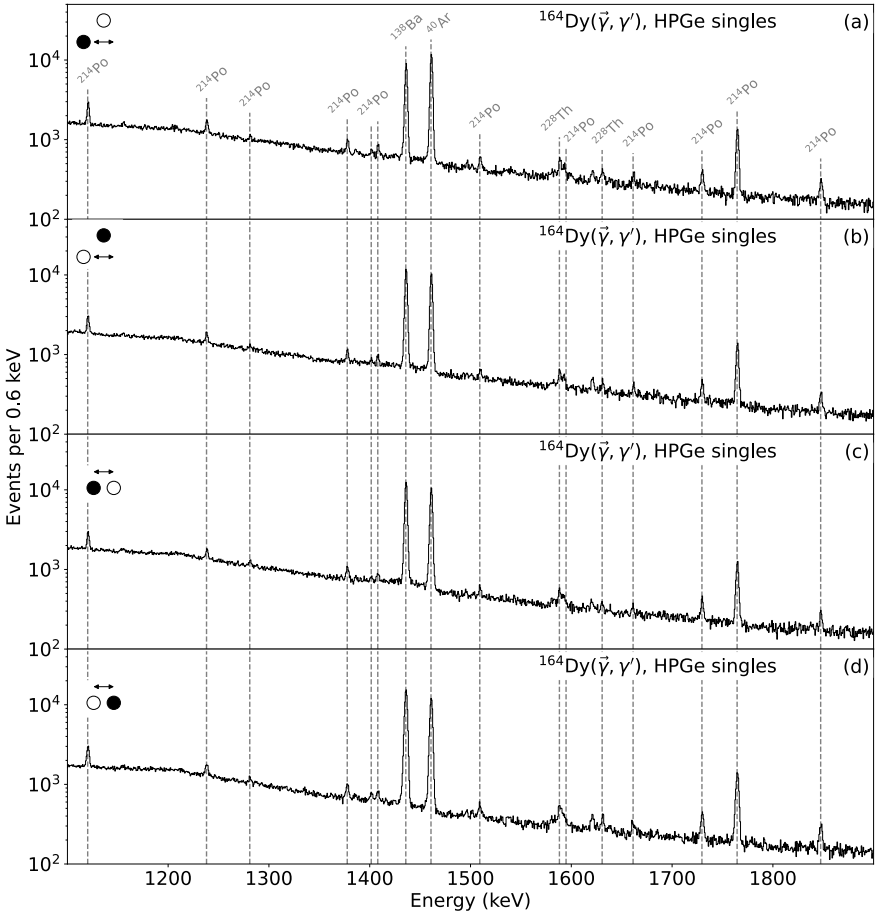

Figure D.10.: Spectra from the ^{164}Dy($\vec{\gamma}, \gamma'$) reaction for a beam energy of 3.075 MeV between 1100 and 1900 keV.

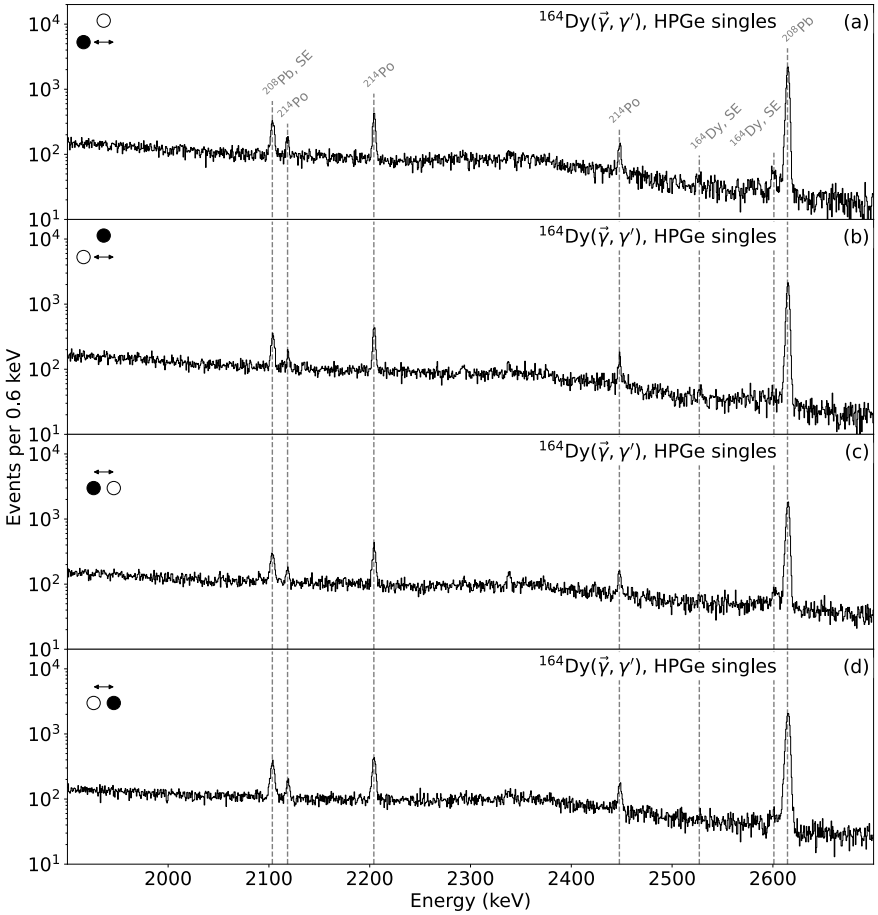

Figure D.11.: Spectra from the ^{164}Dy($\vec{\gamma}, \gamma'$) reaction for a beam energy of 3.075 MeV between 1900 and 2700 keV.

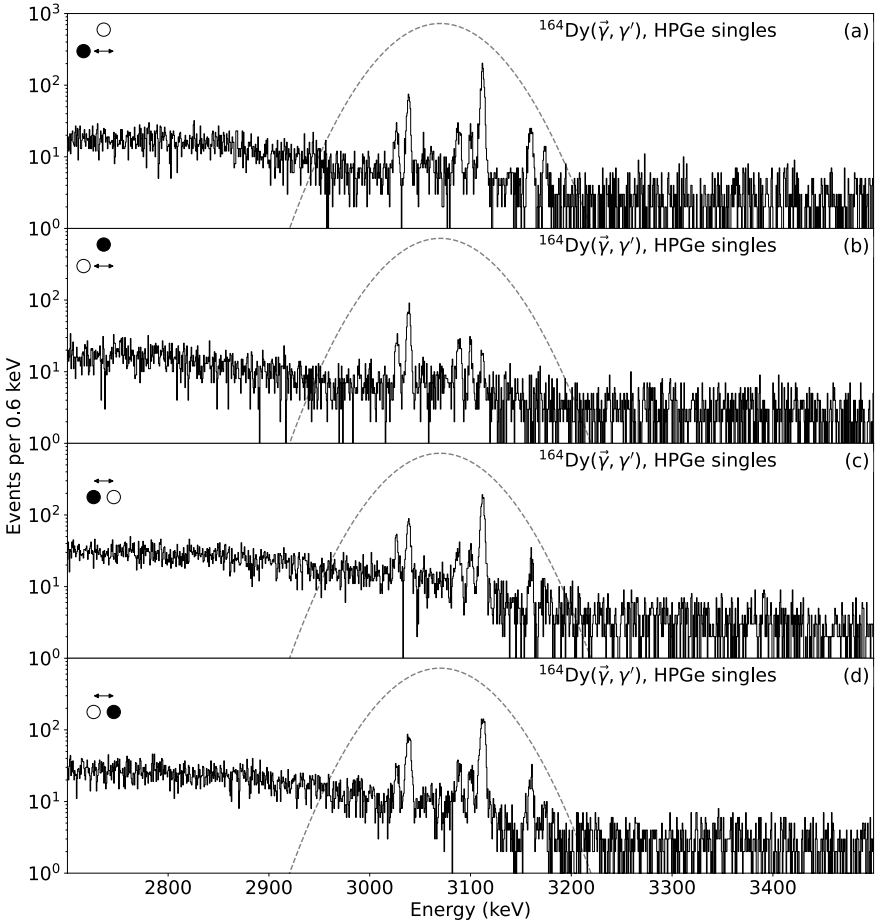

Figure D.12.: Spectra from the ^{164}Dy($\vec{\gamma}, \gamma'$) reaction for a beam energy of 3.075 MeV between 2700 and 3500 keV.

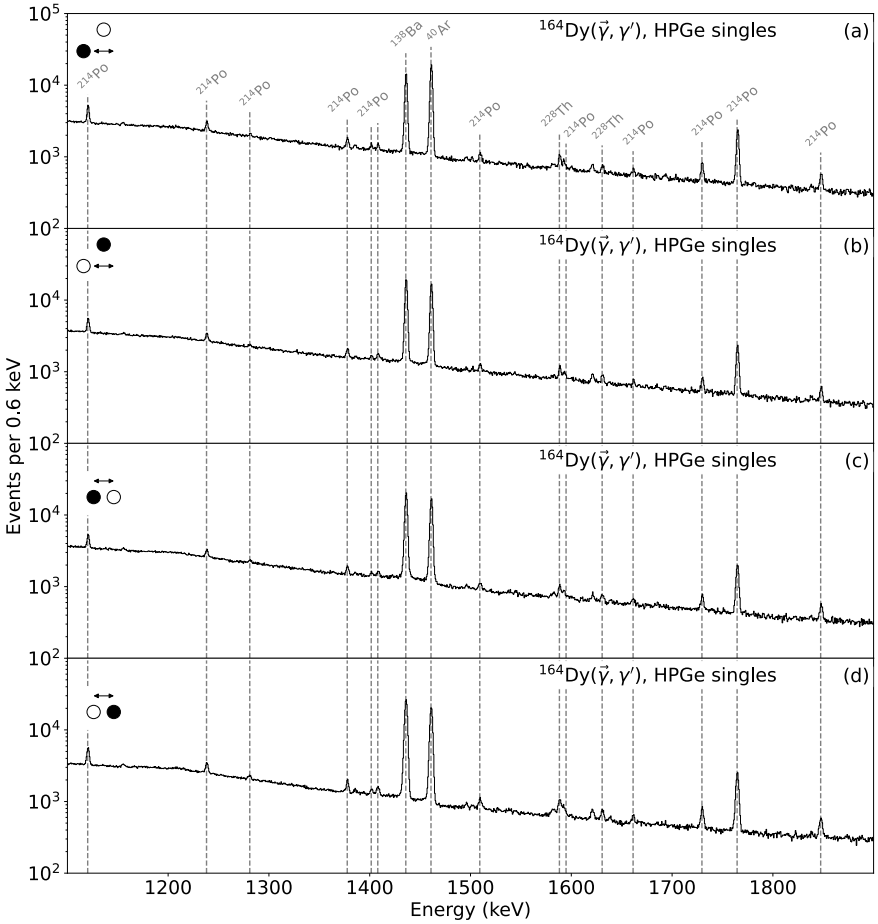

Figure D.13.: Spectra from the ^{164}Dy($\vec{\gamma}, \gamma'$) reaction for a beam energy of 3.180 MeV between 1100 and 1900 keV.

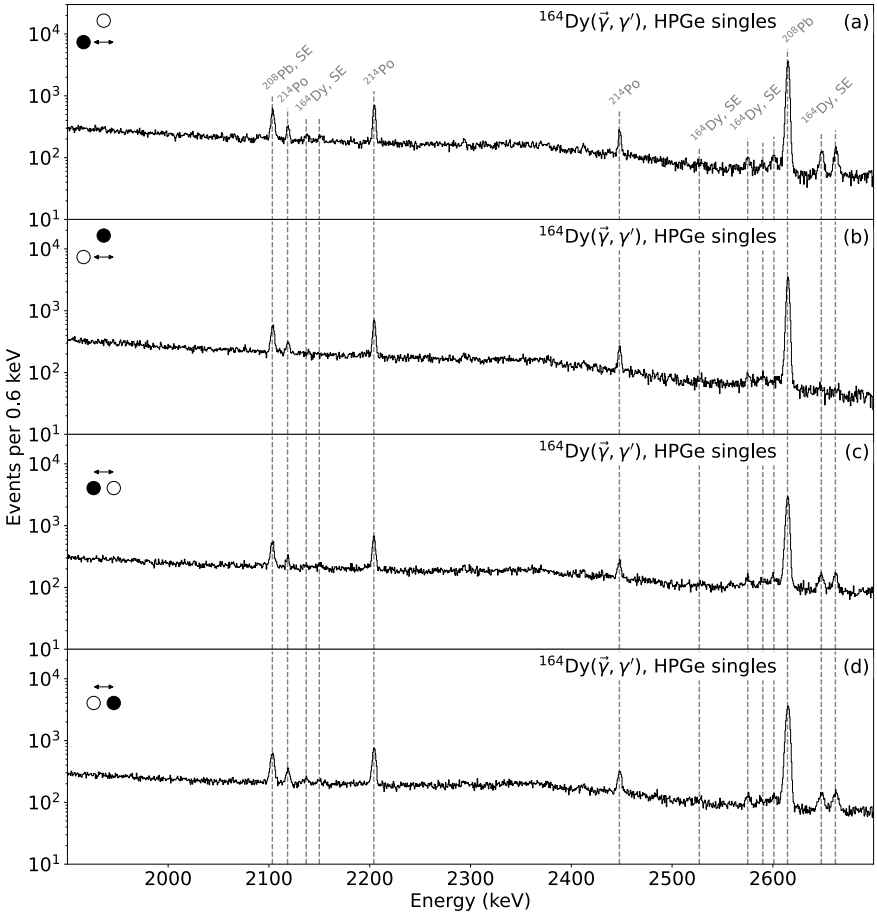

Figure D.14.: Spectra from the ^{164}Dy($\vec{\gamma}, \gamma'$) reaction for a beam energy of 3.180 MeV between 1900 and 2700 keV.

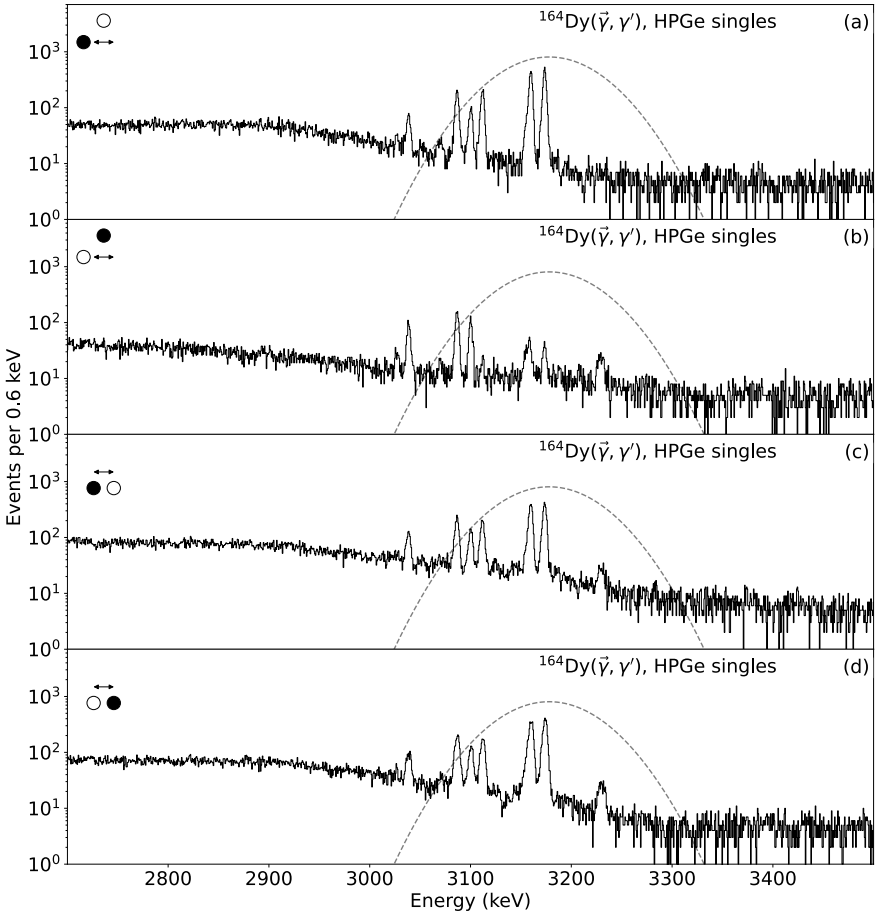

Figure D.15.: Spectra from the ^{164}Dy($\vec{\gamma}, \gamma'$) reaction for a beam energy of 3.180 MeV between 2700 and 3500 keV.

Bibliography

[1] M. G. Mayer, Phys. Rev. **75**, 1969 (1949).

[2] O. Haxel, J. H. D. Jensen, and H. E. Suess, Phys. Rev. **75**, 1766 (1949).

[3] J. Rainwater, Phys. Rev. **79**, 432 (1950).

[4] A. Bohr and B. R. Mottelson, *Nuclear structure*, Vol. 2 (W. A. Benjamin Inc., Reading, Massachusetts, 1975).

[5] T. Otsuka, A. Gade, O. Sorlin, T. Suzuki, and Y. Utsuno, Rev. Mod. Phys. **92**, 015002 (2020).

[6] E. K. Warburton, J. A. Becker, and B. A. Brown, Phys. Rev. C **41**, 1147 (1990).

[7] Y. Blumenfeld, T. Nilsson, and P. van Duppen, Phys. Scr. **T152**, 014023 (2013).

[8] P. Federman and S. Pittel, Phys. Lett. B **69**, 385 (1977).

[9] A. de Shalit and M. Goldhaber, Phys. Rev. **92**, 1211 (1953).

[10] P. Federman and S. Pittel, Phys. Rev. C **20**, 820 (1979).

[11] M. N. Harakeh and A. Van der Woude, *Giant resonances: fundamental high-frequency modes of nuclear excitation* (Oxford Studies in Nuclear Physics, 2002).

[12] W. Bothe and W. Gentner, Z. Phys. **106**, 236 (1937).

[13] F. Iachello and A. Arima, *The Interacting Boson Model* (Cambridge University Press, 1987).

[14] F. Iachello, Phys. Rev. Lett. **53**, 1427 (1984).

[15] N. Pietralla, P. von Brentano, and A. F. Lisetskiy, Prog. Part. Nucl. Phys. **60**, 225 (2008).

[16] D. Bohle et al., Phys. Lett. B **137**, 27 (1984).

[17] K. Heyde, P. von Neumann-Cosel, and A. Richter, Rev. Mod. Phys. **82**, 2365 (2010).

[18] R. F. Casten, D. D. Warner, D. S. Brenner, and R. L. Gill, Phys. Rev. Lett. **47**, 1433 (1981).

[19] J. Beller, "Systematische Untersuchung exotischer Zerfallskanäle der Scherenmode in Gadoliniumisotopen", PhD thesis (TU Darmstadt, 2014).

[20] T. C. Li et al., Phys. Rev. C **71**, 044318 (2005).

[21] N. Pietralla et al., Phys. Rev. Lett. **83**, 1303 (1999).

[22] N. Pietralla et al., Phys. Rev. Lett. **84**, 3775 (2000).

[23] D. Bohle et al., Phys. Rev. Lett. **55**, 1661 (1985).

[24] T. Beck et al., Phys. Rev. Lett. **118**, 212502 (2017).

[25] E. Noether, Gött. Nachr. **1918**, 235 (1918).

[26] E. Caurier, G. Martínez-Pinedo, F. Nowacki, A. Poves, and A. P. Zuker, Rev. Mod. Phys. **77**, 427 (2005).

[27] L. Coraggio, A. Covello, A. Gargano, N. Itaco, and T. Kuo, Prog. Part. Nucl. Phys. **62**, 135 (2009).

[28] A. Bohr and B. R. Mottelson, *Nuclear structure*, Vol. 1 (W. A. Benjamin Inc., Reading, Massachusetts, 1969).

[29] C. H. Townes, H. M. Foley, and W. Low, Phys. Rev. **76**, 1415 (1949).

[30] H. B. G. Casimir, *On the interaction between atomic nuclei and electrons* (Springer Netherlands, 1936).

[31] A. Bohr, Phys. Rev. **81**, 331 (1951).

[32] F. Asaro, F. Stephens, and I. Perlman, Phys. Rev. **92**, 1495 (1953).

[33] F. S. Stephens, F. Asaro, and I. Perlman, Phys. Rev. **96**, 1568 (1954).

[34] F. S. Stephens, F. Asaro, and I. Perlman, Phys. Rev. **100**, 1543 (1955).

[35] P. A. Butler and W. Nazarewicz, Rev. Mod. Phys. **68**, 349 (1996).

[36] B. M. Strutinsky, At. Energ. **1**, 611 (1956).

[37] K. Lee and D. R. Inglis, Phys. Rev. **108**, 774 (1957).

[38] J. Cocks et al., Nucl. Phys. A **645**, 61 (1999).

[39] M. Dahlinger et al., Nucl. Phys. A **484**, 337 (1988).

[40] P. Butler and W. Nazarewicz, Nucl. Phys. A **533**, 249 (1991).

[41] L. P. Gaffney et al., Nature **497**, 199 (2013).

[42] A. de Shalit and I. Talmi, *Nuclear shell theory* (Dover Publications, Inc., 1993).

[43] A. Frank, J. Jolie, and P. van Isacker, *Symmetries in atomic nuclei - from isospin to supersymmetry*, 2nd ed., Springer Tracts in Modern Physics 230 (Springer International Publishing, 2019).

[44] R. F. Casten, *Nuclear structure from a simple perspective* (Oxford Studies in Nuclear Physics, 1990).

[45] A. Zilges, "Untersuchung niedrigliegender Dipolanregungen in den Kernen der Seltenen Erden", PhD thesis (Universität zu Köln, 1992).

[46] G. Alaga, K. Alder, A. Bohr, and B. R. Mottelson, Dan. Mat. Fys. Medd. **29** (1955).

[47] E. Hammarén, P. Heikkinen, K. Schmid, and A. Faessler, Nucl. Phys. A **541**, 226 (1992).

[48] E. Epelbaum, H.-W. Hammer, and U.-G. Meißner, Rev. Mod. Phys. **81**, 1773 (2009).

[49] R. Machleidt and D. Entem, Phys. Rep. **503**, 1 (2011).

[50] L. Huth, V. Durant, J. Simonis, and A. Schwenk, Phys. Rev. C **98**, 044301 (2018).

[51] T. Otsuka, Y. Tsunoda, T. Abe, N. Shimizu, and P. Van Duppen, Phys. Rev. Lett. **123**, 222502 (2019).

[52] T. Otsuka, M. Honma, T. Mizusaki, N. Shimizu, and Y. Utsuno, Prog. Part. Nucl. Phys. **47**, 319 (2001).

[53] N. Shimizu et al., Prog. Theo. Exp. Phys. **2012**, 01A205 (2012).

[54] S. Sels et al., Phys. Rev. C **99**, 044306 (2019).

[55] J. P. Elliott, Proceedings of the Royal Society of London A: Mathematical, Physical and Engineering Sciences **245**, 128 (1958).

[56] D. Janssen, R. V. Jolos, and F. Dönau, Nucl. Phys. A **224**, 93 (1974).

[57] H. Feshbach and F. Iachello, Phys. Lett. B **45**, 7 (1973).

[58] F. Iachello and A. Arima, Phys. Lett. B **53**, 309 (1974).

[59] P. van Isacker, K. Heyde, J. Jolie, and A. Sevrin, Ann. Phys. **171**, 253 (1986).

[60] R. F. Casten and D. D. Warner, Rev. Mod. Phys. **60**, 389 (1988).

[61] R. F. Casten et al., *Algebraic approaches to nuclear structure* (Harwood Academic Publishers, 1993).

[62] G. Gneuss and W. Greiner, Nucl. Phys. A **171**, 449 (1971).

[63] A. Arima and F. Iachello, Phys. Rev. Lett. **35**, 1069 (1975).

[64] I. Talmi, *Simple models of complex nuclei*, Contemporary concepts in physics (Taylor & Francis, 1993).

[65] B. G. Wybourne, *Classical groups for physicists* (John Wiley & Sons, Inc., 1993).

[66] A. Arima, T. Ohtsuka, F. Iachello, and I. Talmi, Phys. Lett. B **66**, 205 (1977).

[67] T. Otsuka, A. Arima, and F. Iachello, Nucl. Phys. A **309**, 1 (1978).

[68] H. Harter, A. Gelberg, and P. von Brentano, Phys. Lett. B **157**, 1 (1985).

[69] P. van Isacker, K. Heyde, M. Waroquier, and G. Wenes, Phys. Lett. B **104**, 5 (1981).

[70] K. Heyde, P. van Isacker, M. Waroquier, and J. Moreau, Phys. Rev. C **29**, 1420 (1984).

[71] R. F. Casten, P. von Brentano, K. Heyde, P. van Isacker, and J. Jolie, Nucl. Phys. A **439**, 289 (1985).

[72] R. F. Casten and P. von Brentano, Phys. Lett. B **152**, 22 (1985).

[73] A. Arima and F. Iachello, Ann. Phys. **99**, 253 (1976).

[74] A. Arima and F. Iachello, Ann. Phys. **111**, 201 (1978).

[75] A. Arima and F. Iachello, Ann. Phys. **123**, 468 (1979).

[76] J. A. Cizewski et al., Phys. Rev. Lett. **40**, 167 (1978).

[77] R. F. Casten, P. von Brentano, and A. M. I. Haque, Phys. Rev. C **31**, 1991 (1985).

[78] A. Arima and F. Iachello, "The Interacting Boson Model", in *Advances in Nuclear Physics: Volume 13*, edited by J. W. Negele and E. Vogt (Plenum Press, New York, Boston, MA, 1984), p. 139.

[79] C. W. Reich, Nucl. Data Sheets **113**, 2537 (2012).

[80] A. Aprahamian, D. S. Brenner, R. F. Casten, R. L. Gill, and A. Piotrowski, Phys. Rev. Lett. **59**, 535 (1987).

[81] K. Heyde and J. L. Wood, Rev. Mod. Phys. **83**, 1467 (2011).

[82] A. Leviatan, N. Gavrielov, J. E. García-Ramos, and P. van Isacker, Phys. Rev. C **98**, 031302 (2018).

[83] Y Alhassid and A Leviatan, J. Phys. A: Math. Gen. **25**, L1265 (1992).

[84] A. Leviatan, Phys. Rev. Lett. **77**, 818 (1996).

[85] A. Leviatan, Prog. Part. Nucl. Phys. **66**, 93 (2011).

[86] F. Iachello and I. Talmi, Rev. Mod. Phys. **59**, 339 (1987).

[87] D. J. Dean and M. Hjorth-Jensen, Rev. Mod. Phys. **75**, 607 (2003).

[88] F. Iachello, G. Puddu, O. Scholten, A. Arima, and T. Otsuka, Phys. Lett. B **89**, 1 (1979).

[89] M. Baldo and G. F. Burgio, Prog. Part. Nucl. Phys. **91**, 203 (2016).

[90] A. Faessler, G. Kyrchev, and R. Nojarov, Nucl. Phys. A **487**, 37 (1988).

[91] F. G. Scholtz, G. Kyrchev, and A. Faessler, Nucl. Phys. A **491**, 91 (1989).

[92] J. Kleemann, *Decay Characteristics of the Scissors Mode of the* $0\nu\beta\beta$*-Decay Mother* ^{150}Nd, M.Sc. thesis, TU Darmstadt, 2018.

[93] D. D. Warner and R. F. Casten, Phys. Rev. Lett. **48**, 1385 (1982).

[94] D. D. Warner and R. F. Casten, Phys. Rev. C **28**, 1798 (1983).

[95] P. O. Lipas, P. Toivonen, and D. D. Warner, Phys. Lett. B **155**, 295 (1985).

[96] H. Harter, P. von Brentano, A. Gelberg, and R. F. Casten, Phys. Rev. C **32**, 631 (1985).

[97] J. Jolie, P. van Isacker, K. Heyde, and A. Frank, Phys. Rev. Lett. **55**, 1457 (1985).

[98] A. Novoselsky and I. Talmi, Phys. Lett. B **160**, 13 (1985).

[99] T. Otsuka, A. Arima, F. Iachello, and I. Talmi, Phys. Lett. B **76**, 139 (1978).

[100] K. A. Sage and B. R. Barrett, Phys. Rev. C **22**, 1765 (1980).

[101] H.-C. Wu and X.-Q. Zhou, Nucl. Phys. A **417**, 67 (1984).

[102] N. Yoshinaga, Y. Akiyama, and A. Arima, Phys. Rev. C **38**, 419 (1988).

[103] C. Fransen et al., Phys. Rev. C **67**, 024307 (2003).

[104] R. Casperson, V. Werner, and S. Heinze, Phys. Lett. B **721**, 51 (2013).

[105] J. Engel and F. Iachello, Nucl. Phys. A **472**, 61 (1987).

[106] D. Kusnezov and F. Iachello, Phys. Lett. B **209**, 420 (1988).

[107] S. Pascu et al., Phys. Rev. C **91**, 034321 (2015).

[108] M. Spieker, S. Pascu, A. Zilges, and F. Iachello, Phys. Rev. Lett. **114**, 192504 (2015).

[109] D. Rowe and F. Iachello, Phys. Lett. B **130**, 231 (1983).

[110] A. Leviatan and P. van Isacker, Phys. Rev. Lett. **89**, 222501 (2002).

[111] A. Leviatan and I. Sinai, Phys. Rev. C **60**, 061301 (1999).

[112] R. F. Casten, R. B. Cakirli, K. Blaum, and A. Couture, Phys. Rev. Lett. **113**, 112501 (2014).

[113] A. Couture, R. F. Casten, and R. B. Cakirli, Phys. Rev. C **91**, 014312 (2015).

[114] J. Stachel, P. van Isacker, and K. Heyde, Phys. Rev. C **25**, 650 (1982).

[115] J. Elliot and A. White, Phys. Lett. B **97**, 169 (1980).

[116] F. Iachello and P. van Isacker, *The Interacting Boson-Fermion Model* (Cambridge University Press, 1991).

[117] A. Bohr, Dan. Mat. Fys. Medd. **27** (1952).

[118] A. Bohr and B. R. Mottelson, Dan. Mat. Fys. Medd. **27** (1953).

[119] L. Fortunato, Eur. Phys. J. A **26**, 1 (2005).

[120] G. Scharff-Goldhaber and J. Weneser, Phys. Rev. **98**, 212 (1955).

[121] L. Wilets and M. Jean, Phys. Rev. **102**, 788 (1956).

[122] A. E. L. Dieperink, O. Scholten, and F. Iachello, Phys. Rev. Lett. **44**, 1747 (1980).

[123] J. N. Ginocchio and M. W. Kirson, Phys. Rev. Lett. **44**, 1744 (1980).

[124] P. van Isacker and J.-Q. Chen, Phys. Rev. C **24**, 684 (1981).

[125] A. Dieperink, Prog. Part. Nucl. Phys. **9**, 121 (1983).

[126] F. Iachello, Nucl. Phys. A **358**, 89 (1981).

[127] D. Guéry-Odelin and S. Stringari, Phys. Rev. Lett. **83**, 4452 (1999).

[128] O. M. Maragò et al., Phys. Rev. Lett. **84**, 2056 (2000).

[129] A. Minguzzi and M. P. Tosi, Phys. Rev. A **63**, 023609 (2001).

[130] E. Lipparini and S. Stringari, Phys. Rev. Lett. **63**, 570 (1989).

[131] V. O. Nesterenko, W. Kleinig, F. F. de Souza Cruz, and N. Lo Iudice, Phys. Rev. Lett. **83**, 57 (1999).

[132] P.-G. Reinhard, V. O. Nesterenko, E. Suraud, S. El Gammal, and W. Kleinig, Phys. Rev. A **66**, 013206 (2002).

[133] L. Serra, A. Puente, and E. Lipparini, Phys. Rev. B **60**, R13966 (1999).

[134] I. Ferrier-Barbut et al., Phys. Rev. Lett. **120**, 160402 (2018).

[135] W. Greiner, Phys. Rev. Lett. **14**, 599 (1965).

[136] W. Greiner, Nucl. Phys. **80**, 417 (1966).

[137] A. Faessler, Nucl. Phys. **85**, 653 (1966).

[138] T. Suzuki and D. Rowe, Nucl. Phys. A **289**, 461 (1977).

[139] N. Lo Iudice and F. Palumbo, Phys. Rev. Lett. **41**, 1532 (1978).

[140] N. Lo Iudice and F. Palumbo, Nucl. Phys. A **326**, 193 (1979).

[141] E. Lipparini and S. Stringari, Phys. Lett. B **130**, 139 (1983).

[142] G. De Franceschi, F. Palumbo, and N. Lo Ludice, Lettere al Nuovo Cimento **37**, 61 (1983).

[143] G. De Franceschi, F. Palumbo, and N. Lo Iudice, Phys. Rev. C **29**, 1496 (1984).

[144] D. Bohle, G. Küchler, A. Richter, and W. Steffen, Phys. Lett. B **148**, 260 (1984).

[145] U. E. P. Berg et al., Phys. Lett. B **149**, 59 (1984).

[146] A. Richter, Nucl. Phys. A **507**, 99 (1990).

[147] U. Kneissl, H. H. Pitz, and A. Zilges, Prog. Part. Nucl. Phys. **37**, 349 (1996).

[148] N. Pietralla et al., Phys. Rev. C **58**, 184 (1998).

[149] J. Enders, H. Kaiser, P. von Neumann-Cosel, C. Rangacharyulu, and A. Richter, Phys. Rev. C **59**, R1851 (1999).

[150] J. Enders, P. von Neumann-Cosel, C. Rangacharyulu, and A. Richter, Phys. Rev. C **71**, 014306 (2005).

[151] H. H. Pitz et al., Nucl. Phys. A **509**, 587 (1990).

[152] W. Ziegler, C. Rangacharyulu, A. Richter, and C. Spieler, Phys. Rev. Lett. **65**, 2515 (1990).

[153] I. Bauske et al., Phys. Rev. Lett. **71**, 975 (1993).

[154] J. Margraf et al., Phys. Rev. C **52**, 2429 (1995).

[155] J. Enders, N. Huxel, P. von Neumann-Cosel, and A. Richter, Phys. Rev. Lett. **79**, 2010 (1997).

[156] P. von Brentano et al., Phys. Rev. Lett. **76**, 2029 (1996).

[157] H. Maser et al., Phys. Rev. C **54**, R2129 (1996).

[158] R. W. Hasse and W. D. Myers, *Geometrical relationships of macroscopic nuclear physics*, Springer Series in Nuclear and Particle Physics (Springer-Verlag, 1988).

[159] D. R. Bes and R. A. Broglia, Phys. Lett. B **137**, 141 (1984).

[160] C. Rangacharyulu, A. Richter, H. J. Wörtche, W. Ziegler, and R. F. Casten, Phys. Rev. C **43**, R949 (1991).

[161] N. Pietralla et al., Phys. Rev. C **52**, R2317 (1995).

[162] E. Garrido, E. Moya de Guerra, P. Sarriguren, and J. M. Udrías, Phys. Rev. C **44**, R1250 (1991).

[163] J. Margraf et al., Phys. Rev. C **47**, 1474 (1993).

[164] N. Lo Iudice and A. Richter, Phys. Lett. B **304**, 193 (1993).

[165] D. D. Warner and P. van Isacker, Phys. Lett. B **395**, 145 (1997).

[166] P. van Isacker, M. A. Nagarajan, and D. D. Warner, Phys. Rev. C **45**, R13 (1992).

[167] Y. Sun, C.-L. Wu, K. Bhatt, and M. Guidry, Nucl. Phys. A **703**, 130 (2002).

[168] K. Hatada, K. Hayakawa, and F. Palumbo, Phys. Rev. C **84**, 011302 (2011).

[169] K. Hatada, K. Hayakawa, and F. Palumbo, Phys. Rev. C **88**, 014305 (2013).

[170] F. Palumbo, Nucl. Phys. A **983**, 64 (2019).

[171] S. Sachdev, *Quantum Phase Transitions* (Camebridge University Press, 1998).

[172] R. F. Casten, Nat. Phys. **2**, 811 (2006).

[173] R. F. Casten, Prog. Part. Nucl. Phys. **62**, 183 (2009).

[174] P. Cejnar and J. Jolie, Prog. Part. Nucl. Phys. **62**, 210 (2009).

[175] P. Cejnar, J. Jolie, and R. F. Casten, Rev. Mod. Phys. **82**, 2155 (2010).

[176] R. F. Casten, D. S. Brenner, and P. E. Haustein, Phys. Rev. Lett. **58**, 658 (1987).

[177] N. Nica, Nucl. Data Sheets **154**, 1 (2018).

[178] T. D. Johnson, D. Symochko, M. Fadil, and J. K. Tuli, Nucl. Data Sheets **112**, 1949 (2011).

[179] J. K. Tuli, Nucl. Data Sheets **56**, 607 (1989).

[180] Y. Khazov, A. Rodionov, and G. Shulyak, Nucl. Data Sheets **136**, 163 (2016).

[181] N. Nica, Nucl. Data Sheets **117**, 1 (2014).

[182] S. K. Basu and A. A. Sonzogni, Nucl. Data Sheets **114**, 435 (2013).

[183] M. J. Martin, Nucl. Data Sheets **114**, 1497 (2013).

[184] C. W. Reich, Nucl. Data Sheets **110**, 2257 (2009).

[185] N. Nica, Nucl. Data Sheets **141**, 1 (2017).

[186] C. W. Reich, Nucl. Data Sheets **105**, 557 (2005).

[187] C. W. Reich, Nucl. Data Sheets **108**, 1807 (2007).

[188] B. Singh and J. Chen, Nucl. Data Sheets **147**, 1 (2018).

[189] V. Werner, P. von Brentano, R. F. Casten, and J. Jolie, Phys. Lett. B **527**, 55 (2002).

[190] P. Koseoglou et al., Phys. Rev. C **101**, 014303 (2020).

[191] K. Kumar, Phys. Rev. Lett. **28**, 249 (1972).

[192] D. Cline, Ann. Rev. Nucl. Part. Sci. **36**, 683 (1986).

[193] V. Werner et al., Phys. Rev. C **78**, 051303 (2008).

[194] P. Cejnar and J. Jolie, Phys. Lett. B **420**, 241 (1998).

[195] P. Cejnar and J. Jolie, Phys. Rev. E **58**, 387 (1998).

[196] J. N. Ginocchio and M. Kirson, Nucl. Phys. A **350**, 31 (1980).

[197] F. Iachello, N. V. Zamfir, and R. F. Casten, Phys. Rev. Lett. **81**, 1191 (1998).

[198] F. Iachello and N. V. Zamfir, Phys. Rev. Lett. **92**, 212501 (2004).

[199] E. A. McCutchan, N. V. Zamfir, and R. F. Casten, Phys. Rev. C **71**, 034309 (2005).

[200] E. A. McCutchan, D. Bonatsos, and N. V. Zamfir, Phys. Rev. C **74**, 034306 (2006).

[201] J. Jolie, R. F. Casten, P. von Brentano, and V. Werner, Phys. Rev. Lett. **87**, 162501 (2001).

[202] J. Jolie et al., Phys. Rev. Lett. **89**, 182502 (2002).

[203] D. Warner, Nature **420**, 614 (2002).

[204] P. von Brentano et al., Phys. Rev. Lett. **93**, 152502 (2004).

[205] J. Bonnet, A. Krugmann, J. Beller, N. Pietralla, and R. V. Jolos, Phys. Rev. C **79**, 034307 (2009).

[206] J. Wiederhold et al., Phys. Rev. C **94**, 044302 (2016).

[207] R. Nojarov and A. Faessler, Z. Phys. A **336**, 151 (1990).

[208] S. Iwasaki and K. Hara, Phys. Lett. B **144**, 9 (1984).

[209] T. Beuschel, J. P. Draayer, D. Rompf, and J. G. Hirsch, Phys. Rev. C **57**, 1233 (1998).

[210] T. Beuschel, J. G. Hirsch, and J. P. Draayer, Phys. Rev. C **61**, 054307 (2000).

[211] K. Heyde, C. De Coster, S. Rombouts, and S. J. Freeman, Nucl. Phys. A **596**, 30 (1996).

[212] I. Hamamoto and C. Magnusson, Phys. Lett. B **260**, 6 (1991).

[213] B. L. Berman and S. C. Fultz, Rev. Mod. Phys. **47**, 713 (1975).

[214] A. Richter, Nucl. Phys. A **522**, 139 (1991).

[215] G. Rusev et al., Phys. Rev. Lett. **95**, 062501 (2005).

[216] J. Beller et al., Phys. Rev. Lett. **111**, 172501 (2013).

[217] P. van Isacker et al., Phys. Lett. B **144**, 1 (1984).

[218] K. Heyde and C. De Coster, Phys. Rev. C **44**, R2262 (1991).

[219] K. Heyde, C. De Coster, A. Richter, and H.-J. Wörtche, Nucl. Phys. A **549**, 103 (1992).

[220] T. Otsuka and K.-H. Kim, Phys. Rev. C **50**, R1768 (1994).

[221] G. Siems et al., Phys. Lett. B **320**, 1 (1994).

[222] N. Pietralla, P. von Brentano, R. F. Casten, T. Otsuka, and N. V. Zamfir, Phys. Rev. Lett. **73**, 2962 (1994).

[223] J. Wiederhold, "γ-spectroscopic determination of mean lifetimes and magnetic moments of excited nuclear states", PhD thesis (TU Darmstadt, 2020).

[224] T. Otsuka and J. N. Ginocchio, Phys. Rev. Lett. **54**, 777 (1985).

[225] T. Otsuka and J. N. Ginocchio, Phys. Rev. Lett. **55**, 276 (1985).

[226] O. Scholten et al., Phys. Rev. C **34**, 1962 (1986).

[227] W. D. Hamilton, A. Irbäck, and J. P. Elliott, Phys. Rev. Lett. **53**, 2469 (1984).

[228] J. N. Ginocchio and P. van Isacker, Phys. Rev. C **33**, 365 (1986).

[229] M. Dufour and A. P. Zuker, Phys. Rev. C **54**, 1641 (1996).

[230] K. E. Ide et al., Phys. Rev. C **103**, 054302 (2021).

[231] J. R. Vanhoy et al., Phys. Rev. C **52**, 2387 (1995).

[232] S. F. Hicks, C. M. Davoren, W. M. Faulkner, and J. R. Vanhoy, Phys. Rev. C **57**, 2264 (1998).

[233] G. Rainovski et al., Phys. Rev. Lett. **96**, 122501 (2006).

[234] R. Kern et al., Phys. Rev. C **102**, 041304 (2020).

[235] R. B. Cakirli, R. F. Casten, J. Jolie, and N. Warr, Phys. Rev. C **70**, 047302 (2004).

[236] C. R. Fitzpatrick et al., Phys. Rev. C **78**, 034309 (2008).

[237] U. Kneissl, N. Pietralla, and A. Zilges, J. Phys. G: Nucl. Part. Phys. **32**, R217 (2006).

[238] F. R. Metzger, Prog. Nucl. Phys. **7**, 53 (1959).

[239] H. A. Bethe, Rev. Mod. Phys. **9**, 69 (1937).

[240] J. M. Blatt and V. M. Weisskopf, *Theoretical nuclear physics*, 1st ed. (Springer Verlag, 1979).

[241] K. Krane, R. Steffen, and R. Wheeler, At. Data Nucl. Data Tables **11**, 351 (1973).

[242] B. Schlitt et al., Nucl. Instrum. Methods Phys. Res. A **337**, 416 (1994).

[243] C. Hutter et al., Nucl. Instrum. Methods Phys. Res. A **489**, 247 (2002).

[244] V. N. Litvinenko et al., Phys. Rev. Lett. **78**, 4569 (1997).

[245] H. R. Weller et al., Prog. Part. Nucl. Phys. **62**, 257 (2009).

[246] C. Sun, J. Li, G. Rusev, A. P. Tonchev, and Y. K. Wu, Phys. Rev. ST Accel. Beams **12**, 062801 (2009).

[247] B. Löher et al., Nucl. Instrum. Methods Phys. Res. A **723**, 136 (2013).

[248] C. Sun, "Characterizations and diagnostics of compton light source", PhD thesis (Duke University, https://hdl.handle.net/10161/1579, 2009).

[249] N. Pietralla et al., Phys. Rev. Lett. **88**, 012502 (2001).

[250] N. Pietralla, H. R. Weller, V. N. Litvinenko, M. W. Ahmed, and A. P. Tonchev, Nucl. Instrum. Methods Phys. Res. A **483**, 556 (2002).

[251] H. G. Essel and N. Kurz, IEEE Transactions on Nuclear Science **47**, 337 (2000).

[252] B. Löher, "Probing the decay characteristics of the pygmy dipole resonance in the semi-magic nucleus ^{140}Ce with $\gamma - \gamma$ coincidence measurements", PhD thesis (Johannes Gutenberg-Universität Mainz, 2014).

[253] U. Hartmann, D. Bohle, F. Humbert, and A. Richter, Nucl. Phys. A **499**, 93 (1989).

[254] J. H. Kelley, J. E. Purcell, and C. G. Sheu, Nucl. Phys. A **968**, 71 (2017).

[255] F. Ajzenberg-Selove, Nucl. Phys. A **523**, 1 (1991).

[256] C. Sun and Y. K. Wu, Phys. Rev. ST Accel. Beams **14**, 044701 (2011).

[257] C. Wesselborg et al., Phys. Lett. B **207**, 22 (1988).

[258] H. Friedrichs et al., Phys. Rev. C **45**, R892 (1992).

[259] E. L. Johnson et al., Phys. Rev. C **52**, 2382 (1995).

[260] D. Bohle, G. Kilgus, A. Richter, C. de Jager, and H. de Vries, Phys. Lett. B **195**, 326 (1987).

[261] V. Werner, "Proton-neutron symmetry at the limits of collectivity", PhD thesis (Universität zu Köln, 2004).

[262] *Electronic logbook of the γ^3 collaboration for the 2012-2014 campaigns*, `https://elog.ikp.physik.tu-darmstadt.de/gamma3_2012-2014`.

[263] BIPM et al., *JCGM 100: evaluation of measurement data – guide to the expression of uncertainty in measurement*, 1st ed. (Joint Committee for Guides in Metrology, Sèvres, 2008).

[264] BIPM et al., *JCGM 101: evaluation of measurement data – supplement 1 to the "guide to the expression of uncertainty in measurement" – propagation of distributions using a monte carlo method*, 1st ed. (Joint Committee for Guides in Metrology, Sèvres, 2008).

[265] H. Junde, H. Su, and Y. Dong, Nucl. Data Sheets **112**, 1513 (2011).

[266] M. Tanabashi et al., Phys. Rev. D **98**, 030001 (2018).

[267] J. Chen, Nucl. Data Sheets **146**, 1 (2017).

[268] J. Chen, Nucl. Data Sheets **140**, 1 (2017).

[269] Y. A. Akovali, Nucl. Data Sheets **76**, 127 (1995).

[270] M. J. Martin, Nucl. Data Sheets **108**, 1583 (2007).

[271] G. R. Gilmore, *Practical gamma-ray spectrometry*, 2nd ed. (John Wiley & Sons, Ltd., 2008).

[272] M. Shamsuzzoha Basunia, Nucl. Data Sheets **127**, 69 (2015).

[273] E. Browne and J. K. Tuli, Nucl. Data Sheets **114**, 1849 (2013).

[274] E. Browne and J. K. Tuli, Nucl. Data Sheets **108**, 2173 (2007).

[275] H. W. Koch and J. W. Motz, Rev. Mod. Phys. **31**, 920 (1959).

[276] L. I. Schiff, Phys. Rev. **83**, 252 (1951).

[277] M. Morháč, J. Kliman, V. Matoušek, M. Veselský, and I. Turzo, Nucl. Instrum. Methods Phys. Res. A **401**, 385 (1997).

[278] J. H. Hubbell and S. M. Seltzer, *Tables of x-ray mass attenuation coefficients and mass energy-absorption coefficients* (National Institute of Standards and Technology, Gaithersburg, MD, 2004).

[279] F. Ajzenberg-Selove, Nucl. Phys. A **506**, 1 (1990).

[280] M. Shamsuzzoha Basunia, Nucl. Data Sheets **112**, 1875 (2011).

[281] M. Tamkas et al., Nucl. Phys. A **987**, 79 (2019).

[282] U. Gayer et al., Phys. Rev. C **100**, 034305 (2019).

[283] O. Papst et al., Phys. Rev. C **102**, 034323 (2020).

[284] D. Savran and J. Isaak, Nucl. Instrum. Methods Phys. Res. A **899**, 28 (2018).

[285] G. Rusev et al., Phys. Rev. C **79**, 047601 (2009).

[286] A. Schiller et al., Phys. Rev. C **63**, 021306 (2001).
[287] M. Guttormsen et al., Phys. Rev. C **68**, 064306 (2003).
[288] H. T. Nyhus et al., Phys. Rev. C **85**, 014323 (2012).
[289] T. Renstrøm et al., Phys. Rev. C **98**, 054310 (2018).
[290] C. W. Reich, Nucl. Data Sheets **104**, 1 (2005).
[291] N. Nica, Nucl. Data Sheets **132**, 1 (2016).
[292] H. Friedrichs et al., Nucl. Phys. A **567**, 266 (1994).
[293] D. C. Sousa, L. L. Riedinger, E. G. Funk, and J. W. Mihelich, Nucl. Phys. A **238**, 365 (1975).
[294] A. Nord et al., Phys. Rev. C **54**, 2287 (1996).
[295] H. H. Pitz et al., Nucl. Phys. A **492**, 411 (1989).
[296] J. Berzins et al., Nucl. Phys. A **584**, 413 (1995).
[297] A. Nord et al., Phys. Rev. C **67**, 034307 (2003).
[298] A. Aprahamian et al., Nucl. Phys. A **764**, 42 (2006).
[299] D. Frekers et al., Phys. Lett. B **218**, 439 (1989).
[300] C. W. Reich and B. Singh, Nucl. Data Sheets **111**, 1211 (2010).
[301] T. Beck et al., Phys. Rev. Lett. **125**, 092501 (2020).
[302] T. Beck et al., AIP Conf. Proc. **1681**, 040007 (2015).
[303] T. Beck et al., EPJ Web Conf. **178**, edited by Y. Sun, 02022 (2018).
[304] S. G. Rohoziński and W. Greiner, Z. Phys. A **322**, 271 (1985).
[305] Y. Sun, C.-L. Wu, K. Bhatt, M. Guidry, and D. H. Feng, Phys. Rev. Lett. **80**, 672 (1998).
[306] A. Zilges et al., Phys. Rev. C **42**, 1945 (1990).
[307] D. Savran et al., Phys. Rev. C **71**, 034304 (2005).
[308] W. Ziegler et al., Nucl. Phys. A **564**, 366 (1993).
[309] N. J. Stone, At. Data Nucl. Data Tables **111**, 1 (2016).
[310] E. Münck, Z. Phys. A **208**, 184 (1968).
[311] N. Pietralla et al., Nucl. Phys. A **618**, 141 (1997).

[312] S. Freeman et al., Phys. Lett. B **222**, 347 (1989).

[313] R. Nojarov and A. Faessler, Nucl. Phys. A **484**, 1 (1988).

[314] V. G. Soloviev, A. V. Sushkov, N. Y. Shirikova, and N. Lo Iudice, Nucl. Phys. A **600**, 155 (1996).

[315] V. G. Soloviev, *Theory of atomic nuclei: quasiparticles and phonons* (Institute of Physics Publishing, 1992).

[316] N. Lo Iudice, V. Yu. Ponomarev, C. Stoyanov, A. V. Sushkov, and V. V. Voronov, J. Phys. G: Nucl. Part. Phys. **39**, 043101 (2012).

[317] I. Towner, Phys. Rep. **155**, 263 (1987).

[318] P. G. Hansen, P. Hornshøj, and K. H. Johansen, Nucl. Phys. A **126**, 464 (1969).

[319] R. F. Casten, D. D. Warner, and A. Aprahamian, Phys. Rev. C **28**, 894 (1983).

[320] R. F. Casten, J. Jolie, R. B. Cakirli, and A. Couture, Phys. Rev. C **94**, 061303 (2016).

[321] P. O. Lipas, Nucl. Phys. **39**, 468 (1962).

[322] L. L. Riedinger, N. R. Johnson, and J. H. Hamilton, Phys. Rev. **179**, 1214 (1969).

[323] V. M. Mikhailov, Izv. Akad. Nauk SSSR, Ser. Fiz. **28**, 308 (1964).

[324] V. M. Mikhailov, Izv. Akad. Nauk SSSR, Ser. Fiz. **30**, 1334 (1966).

[325] T. J. Humanic, J. X. Saladin, J. G. Alessi, and A. Hussein, Phys. Rev. C **27**, 550 (1983).

[326] H. J. Wollersheim, *Kernstruktur schnell rotierender Atomkerne*, Habilitation, (Goethe-Universität Franfurt, 1992).

[327] D. F. Winchell et al., Phys. Rev. C **51**, 2952 (1995).

[328] D. R. Bès, P. Federman, E. Maqueda, and A. Zuker, Nucl. Phys. **65**, 1 (1965).

[329] K. Heyde and C. De Coster, Phys. Lett. B **305**, 322 (1993).

[330] A. Ikeda and T. Shimano, Nucl. Phys. A **557**, 573 (1993).

[331] N. Lo Iudice, E. Lipparini, S. Stringari, F. Palumbo, and A. Richter, Phys. Lett. B **161**, 18 (1985).

[332] F. Palumbo and A. Richter, Phys. Lett. B **158**, 101 (1985).

[333] A. Davydov and V. Rostovsky, Soviet Physics JETP **36**, 1275 (1959).

[334] A. Davydov and G. Filippov, Soviet Physics JETP **35**, 303 (1958).
[335] A. Davydov and G. Filippov, Nucl. Phys. **8**, 237 (1958).
[336] A. Davydov and A. Chaban, Nucl. Phys. **20**, 499 (1960).
[337] M. Lettmann et al., Phys. Rev. C **96**, 011301 (2017).
[338] A. M. Forney et al., Phys. Rev. Lett. **120**, 212501 (2018).
[339] A. D. Ayangeakaa et al., Phys. Rev. Lett. **123**, 102501 (2019).
[340] J. L. Egido and A. Jungclaus, Phys. Rev. Lett. **126**, 192501 (2021).
[341] R. F. Casten and P. von Brentano, Phys. Lett. B **152**, 22 (1985).
[342] N. V. Zamfir and R. F. Casten, Phys. Lett. B **260**, 265 (1991).
[343] C. Fransen et al., Phys. Rev. C **59**, 2264 (1999).
[344] A. Gade et al., Phys. Rev. C **66**, 034311 (2002).
[345] A. Gade, H. Klein, N. Pietralla, and P. von Brentano, Phys. Rev. C **65**, 054311 (2002).
[346] N. Pietralla et al., Phys. Rev. C **57**, 150 (1998).
[347] F. Iachello, Phys. Rev. Lett. **87**, 052502 (2001).
[348] D. Tonev et al., Phys. Rev. C **69**, 034334 (2004).
[349] N. Pietralla and O. M. Gorbachenko, Phys. Rev. C **70**, 011304 (2004).
[350] R. Krücken et al., Phys. Rev. Lett. **88**, 232501 (2002).
[351] K. Dusling and N. Pietralla, Phys. Rev. C **72**, 011303 (2005).
[352] R. F. Casten and N. V. Zamfir, Phys. Rev. Lett. **87**, 052503 (2001).
[353] M. A. Caprio et al., Phys. Rev. C **66**, 054310 (2002).
[354] O. Möller et al., Phys. Rev. C **74**, 024313 (2006).
[355] E. A. McCutchan and R. F. Casten, Phys. Rev. C **74**, 057302 (2006).
[356] M. K. Harder and K. T. Tang, Phys. Lett. B **369**, 1 (1996).
[357] W.-T. Chou, N. V. Zamfir, and R. F. Casten, Phys. Rev. C **56**, 829 (1997).
[358] E. A. McCutchan, N. V. Zamfir, and R. F. Casten, Phys. Rev. C **69**, 064306 (2004).
[359] K. Nomura, N. Shimizu, and T. Otsuka, Phys. Rev. Lett. **101**, 142501 (2008).

[360] K. Nomura, T. Otsuka, N. Shimizu, and L. Guo, Phys. Rev. C **83**, 041302 (2011).

[361] J. Kotila, K. Nomura, L. Guo, N. Shimizu, and T. Otsuka, Phys. Rev. C **85**, 054309 (2012).

[362] K. Nomura and Y. Zhang, Phys. Rev. C **99**, 024324 (2019).

[363] P. E. Garrett, J. Phys. G: Nucl. Part. Phys. **27**, R1 (2001).

[364] A. Aprahamian et al., Phys. Rev. C **98**, 034303 (2018).

[365] A. Leviatan, J. E. García-Ramos, and P. van Isacker, Phys. Rev. C **87**, 021302 (2013).

[366] O. Scholten et al., Nucl. Phys. A **438**, 41 (1985).

[367] A. van Egmond, K. Allaart, and G. Bonsignori, Nucl. Phys. A **436**, 458 (1985).

[368] M. Sambataro and A. E. L. Dieperink, Phys. Lett. B **107**, 249 (1981).

[369] A. Wolf, D. D. Warner, and N. Benczer-Koller, Phys. Lett. B **158**, 7 (1985).

[370] A. Wolf, R. F. Casten, and D. D. Warner, Phys. Lett. B **190**, 19 (1987).

[371] N. J. Stone, At. Data Nucl. Data Tables **90**, 75 (2005).

[372] M. Sambataro, O. Scholten, A. Dieperink, and G. Piccitto, Nucl. Phys. A **423**, 333 (1984).

[373] S. Kuyucak and A. E. Stuchbery, Phys. Lett. B **348**, 315 (1995).

[374] I. Hamamoto and S. Åberg, Phys. Lett. B **145**, 163 (1984).

[375] J. Kleemann, *Zerfallsverhalten der Scherenmode in der* $0\nu\beta\beta$*-Tochter* ^{150}Sm, B.Sc. thesis, TU Darmstadt, 2016.

[376] K. Sieja, G. Martínez-Pinedo, L. Coquard, and N. Pietralla, Phys. Rev. C **80**, 054311 (2009).

[377] D. Bianco, F. Andreozzi, N. Lo Iudice, A. Porrino, and F. Knapp, Phys. Rev. C **85**, 034332 (2012).

[378] N. Shimizu, T. Otsuka, T. Mizusaki, and M. Honma, Phys. Rev. Lett. **86**, 1171 (2001).

[379] N. Y. Shirikova, A. V. Sushkov, R. V. Jolos, N. Pietralla, and T. Beck, Phys. Rev. C **99**, 044319 (2019).

[380] F. Palumbo, Phys. Rev. C **93**, 034331 (2016).

[381] C. L. McClelland and C. Goodman, Phys. Rev. **91**, 760 (1953).

[382] K. Alder, A. Bohr, T. Huus, B. Mottelson, and A. Winther, Rev. Mod. Phys. **28**, 432 (1956).

[383] K. Alder, *Coulomb excitation: a collection of reprints*, Perspectives in Physics. A Series of Reprint Collections (Academic Press, 1966).

[384] S. F. Mughabghab, *Atlas of neutron resonances: resonance parameters and thermal cross sections* $Z = 1 - 100$ (Elsevier Science, 2006).

[385] R. G. Helmer, Nucl. Data Sheets **107**, 507 (2006).

[386] C. W. Reich, Nucl. Data Sheets **112**, 2497 (2011).

[387] G. F. Knoll, *Radiation detection and measurement*, 4th ed. (John Wiley & Sons, Inc., 2010).

[388] E. G. Kessler et al., Nucl. Instrum. Methods Phys. Res. A **457**, 187 (2001).

[389] H. G. Börner and J. Jolie, J. Phys. G: Nucl. Part. Phys. **19**, 217 (1993).

[390] S. Heinze, "Eine Methode zur Lösung beliebiger bosonischer und fermionischer Vielteilchensysteme", PhD thesis (Universität zu Köln, 2008).

[391] *Electronic logbook of the* γ^3 *collaboration for the 2018 campaign*, `https://elog.ikp.physik.tu-darmstadt.de/gamma3/`.

Acknowledgements

Removed from online version.

Academic CV

Removed from online version.